Hugo Miguel Bento Rebelo

Licenciado em Ciências de Engenharia Civil

Numerical Simulation of Blast Effects on Fibre Grout RC Panels

Dissertação para obtenção do Grau de Mestre
em Engenharia Civil - Perfil Estruturas

Orientador: Professor Doutor Corneliu Cismaşiu,
Professor Associado, FCT/UNL

Co-orientador: Major (Engenheiro Militar) Gabriel Gomes,
Investigador, Academia Militar

Júri:

Presidente: Professor Doutor Carlos Manuel Chastre Rodrigues
Arguente: Professor Doutor Válter José da Guia Lúcio
Vogal: Professor Doutor Corneliu Cismaşiu

FACULDADE DE
CIÊNCIAS E TECNOLOGIA
UNIVERSIDADE NOVA DE LISBOA

Novembro de 2015

Numerical Simulation of Blast Effects on Fibre Grout RC Panels

To my grandfather, Prof. Dr. Carlos Lopes Bento

Acknowledgements

The present dissertation would not have been accomplished without the support and assistance from many people who have either helped me or encouraged me. For all those people, my most profound thanks.

I would like to express my deepest and heartfelt recognition to my adviser, Professor Corneliu Cismaşiu. I would like to thank him for his priceless scientific teachings, for his invaluable guidance and commitment, which allowed me to complete this dissertation.

I am truly grateful to my co-adviser, Major (Engenheiro Militar) Gabriel Gomes, for his invaluable guidance through the blast loads topic, which have made this experience so meaningful.

I also thank the remaining teaching staff that accompanied my academic career, which contributed to my growth as an engineer and human being.

I thank Concremat for having supplied the reinforced concrete panels.

I leave words of appreciation to my colleagues, Bruno, David, Gonçalo, Nuno and Pedro, with whom I had the pleasure of sharing moments along the way.

A special thanks to Rita for the unconditional support and help in general problem solving and revision.

Lastly, I thank my family for all their love, support and inspiration.

Abstract

The main purpose of the present dissertation is the simulation of the response of fibre grout strengthened RC panels when subjected to blast effects using the Applied Element Method, in order to validate and verify its applicability.

Therefore, four experimental models, three of which were strengthened with a cement-based grout, each reinforced by one type of steel reinforcement, were tested against blast effects. After the calibration of the experimental set-up, it was possible to obtain and compare the response to the blast effects of the model without strengthening (reference model), and a fibre grout strengthened RC panel (strengthened model).

Afterwards, a numerical model of the reference model was created in the commercial software *Extreme Loading for Structures*, which is based on the Applied Element Method, and calibrated to the obtained experimental results, namely to the residual displacement obtained by the experimental monitoring system. With the calibration verified, it is possible to assume that the numerical model correctly predicts the response of fibre grout RC panels when subjected to blast effects.

In order to verify this assumption, the strengthened model was modelled and subjected to the blast effects of the corresponding experimental set-up.

The comparison between the residual and maximum displacements and the bottom surface's cracking obtained in the experimental and the numerical tests yields a difference of 4 % for the maximum displacements of the reference model, and a difference of 4 and 10 % for the residual and maximum displacements of the strengthened model, respectively. Additionally, the cracking on the bottom surface of the models was similar in both methods.

Therefore, one can conclude that the Applied Element Method can correctly predict and simulate the response of fibre grout strengthened RC panels when subjected to blast effects.

Keywords:

Non-linear dynamic analysis, Applied Element Method, Blast effects, Reinforced grout.

Resumo

O principal objetivo da presente dissertação é a simulação da resposta de placas de betão armado reforçadas com argamassas armadas com fibras contínuas de aço quando sujeitas ao efeito de explosivos recorrendo ao Método dos Elementos Aplicados, de modo a validar e verificar a sua aplicabilidade.

Para tal, foram ensaiados quatro modelos experimentais, três dos quais reforçados, cada um com um tipo de armadura embebida numa calda cimentícia, submetendo-os a explosões de determinada magnitude. Após a calibração do sistema de ensaio, foi possível obter e comparar a resposta do modelo de referência, sem reforço, e do modelo reforçado com calda armada com fibras contínuas de aço ao efeito de explosivos. Seguidamente, criou-se um modelo numérico do modelo de referência no programa de cálculo *Extreme Loading for Structures*, baseado no Método dos Elementos Aplicados, e calibrou-se de acordo com os resultados experimentais, nomeadamente, de acordo com o deslocamento residual obtido através do sistema de monitorização. Após a verificação da calibração, assume-se que o modelo numérico prevê corretamente o comportamento de placas de betão armado com argamassas armadas quando sujeitas ao efeito de explosivos.

De modo a verificar esta suposição, o modelo reforçado foi igualmente modelado no programa de cálculo *Extreme Loading for Structures* e sujeito aos efeitos das explosivos do correspondente ensaio experimental.

Comparando os deslocamentos residuais e máximos e a fissuração presente na superfície inferior obtidos experimentalmente e numericamente, obtém-se uma diferença de 4 % para o deslocamento máximo do modelo de referência, e uma diferença de 4 e 10 % para os deslocamentos residual e máximo do modelo reforçado, respetivamente. Adicionalmente, a fissuração na face inferior de ambos os modelos foi semelhante nos dois métodos. Logo, conclui-se que o Método dos Elementos Aplicados pode prever e simular corretamente a resposta de placas de betão armado reforçadas com argamassas armadas com fibras contínuas de aço quando sujeitas ao efeito de explosivos.

Palavras chave:

Análise dinâmica não-linear, Método dos Elementos Aplicados, Efeito de explosivos, Calda reforçada.

Resumo alargado

Introdução

Ao longo da história, verificou-se uma necessidade constante para projetar estruturas que resistam às ações da gravidade, vento, variações de temperatura e sismos. No entanto, nas últimas décadas, guerras, ataques terroristas e explosões acidentais levaram à necessidade de considerar ações de explosivos no projeto de estruturas importantes, pois a ocorrência de uma explosão no interior ou próximo da estrutura pode resultar em efeitos catastróficos, como o dano e colapso estrutural e a perda de vidas humanas [10].

Devido a estes efeitos, surge a necessidade de projetar estruturas ou soluções de reforço que resistam às ações resultantes de uma explosão. Contudo, a investigação experimental, num ambiente seguro, das ações resultantes de uma explosão tem custos muito elevados. Deste modo, considera-se que os métodos computacionais são uma alternativa viável no estudo da resposta das estruturas quando são sujeitas a ações de explosivos.

Todavia, cenários de explosão resultam em condições altamente não-lineares, o que constitui um problema em Engenharia Estrutural. Logo, é necessário recorrer a métodos computacionais complexos de modo a prever corretamente a sua resposta estrutural.

O Método dos Elementos Aplicados é um método numérico não-linear que permite a simulação do comportamento da estrutura, qualquer que seja o carregamento imposto. Logo, é possível simular o comportamento da estrutura desde o momento em que o carregamento é nulo até ao momento em que esta colapsa.

A presente dissertação recorre ao Método dos Elementos Aplicados para simular a resposta de placas de betão armado reforçadas com argamassas armadas quando sujeitas ao efeito de explosivos, por forma a validar e verificar a sua aplicabilidade, e é parte integrante do projeto *Segurança e Integridade Estrutural de Edifícios Estratégicos face a explosões acidentais ou provocadas - SI4E*, realizado em parceria com a FCT/UNL e a Academia Militar.

As placas de betão armado reforçadas com argamassas armadas foram sujeitas aos efeitos de explosivos no campo militar de Santa Margarida para avaliar a sua resposta quando sujeitas a estes efeitos e estabelecer uma base de comparação para a modelação numérica.

Ações de explosivos

As ações de explosivos podem danificar severamente as estruturas, podendo, por vezes, provocar o colapso das mesmas. Logo, o estudo dos principais efeitos resultantes de uma explosão é essencial. No entanto, na literatura é possível encontrar diversas formulações para esses efeitos, pelo que será realizada uma revisão e comparação das características definidas por estas.

Tipos de explosão

Segundo a *Unified Facilities Criteria* (UFC) [13], os tipos de explosão podem ser separados em dois grandes grupos, explosões confinadas e não confinadas, que por sua vez se encontram divididas em diversos tipos. Apenas se representam na Tabela 1 os tipos de explosão não confinadas, pois apenas estas são de interesse para a presente dissertação. Os efeitos deste tipo de explosões dependem da localização da explosão em relação ao solo e à estrutura em estudo.

Tabela 1: Tipos de explosão não confinadas [13]

Tipo
Explosões aéreas perfeitas
Explosões próximas da superfície
Explosões à superfície

De modo a ser considerada uma explosão aérea perfeita, a onda de choque resultante da mesma não deve sofrer amplificações desde a sua origem até à estrutura. Tal não ocorre no caso das explosões próximas da e à superfície, onde a onda de choque sofre uma amplificação devido às reflexões com a superfície antes de chegar à estrutura. Especificamente, no caso das explosões à superfície, a explosão ocorre tão próximo do solo que a onda de choque sofre uma amplificação na sua origem. Tendo em conta que as explosões presentes no caso de estudo da presente dissertação são explosões aéreas perfeitas, apenas estas serão analisadas com mais detalhe no presente resumo.

Distância reduzida

A utilização de uma distância reduzida (Z) permite a comparação dos parâmetros que caracterizam as ondas de choque, quando estas resultam de explosões diferentes, recorrendo-se geralmente à distância reduzida definida por Hopkinson-Cranz, como:

$$Z = \frac{R}{W^{1/3}} \tag{1}$$

onde R é a distância ao centro da detonação (expressa em m) e W é a massa da carga (expressa em kg).

Fenómenos resultantes de uma explosão

De acordo com [34], *"uma explosão é uma perturbação de pressão causada por um libertação repentina de energia"*. Esta é o resultado de reações químicas que, no caso de detonações, resultam numa reação de oxidação que viaja a uma

velocidade superior à do som através do material que ainda não reagiu, resultando numa onda de choque.

Num ponto a certa distância da origem da detonação é possível definir o tempo de chegada da onda de choque como t_A. Nesse momento, ocorre um pico quase instantâneo de pressão, da pressão atmosférica P_a para uma pressão de pico incidente P_{so}, seguido por um declínio de pressão até à pressão atmosférica durante t_o. Esta fase positiva é seguida por uma fase negativa, caracterizada por um fluxo de ar inverso, que tem um valor de pressão mínimo de P_{so}^- e uma duração de t_o^-, geralmente mais longa que a fase positiva. No entanto, na maioria dos estudos incidentes sobre o tema, a fase negativa é ignorada pois é usualmente mais fraca e gradual que a fase positiva, o que leva a uma resposta estrutural menos significativa. Na Figura 1(a) é possível observar o comportamento descrito.

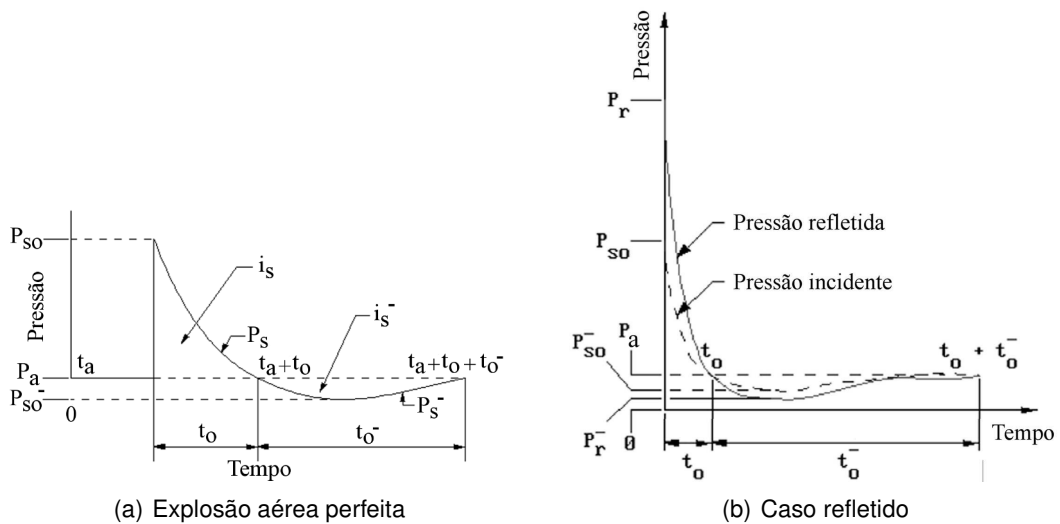(a) Explosão aérea perfeita   (b) Caso refletido

Figura 1: Variação da pressão com o tempo (Adaptado de [13])

De forma a definir por completo os fenómenos resultantes de uma explosão, é necessário obter o impulso específico, representado na Figura 1(a) como i_s e i_s^- para a fase positiva e negativa, respetivamente, através da integração da área do gráfico representado nessa mesma figura.

Kinney e Graham definem uma estimativa numérica, baseadas em explosões de 1 kg de TNT, para os valores da pressão de pico incidente, impulso específico e duração da fase positiva [23]:

$$\frac{P_{so}}{P_a} = \frac{808\left[1+\left(\frac{Z}{4.5}\right)^2\right]}{\sqrt{1+\left(\frac{Z}{0.048}\right)^2}\sqrt{1+\left(\frac{Z}{0.32}\right)^2}\sqrt{1+\left(\frac{Z}{1.35}\right)^2}} \tag{2}$$

$$i_s = \frac{0.067\sqrt{1 + \left(\frac{Z}{0.23}\right)^4}}{Z^2 \sqrt[3]{1 + \left(\frac{Z}{1.55}\right)^3}} \tag{3}$$

$$\frac{t_o}{W^{1/3}} = \frac{980\left[1 + \left(\frac{Z}{0.54}\right)^{10}\right]}{\left[1 + \left(\frac{Z}{0.02}\right)^3\right]\left[1 + \left(\frac{Z}{0.74}\right)^6\right]\sqrt{1 + \left(\frac{Z}{6.9}\right)^2}} \tag{4}$$

onde P_{so}/P_a é a relação entre a pressão de pico incidente e a pressão atmosférica, i_s o impulso específico expresso em [bar.ms] e $t_o/W^{1/3}$ a duração da fase positiva escalada para uma explosão resultante de 1 kg de TNT expressa em [ms/kg$^{1/3}$]. As expressões anteriores encontram-se representadas na Figura 2, juntamente com as estimativas definidas pela UFC, de modo a obter uma melhor comparação entre as formulações.
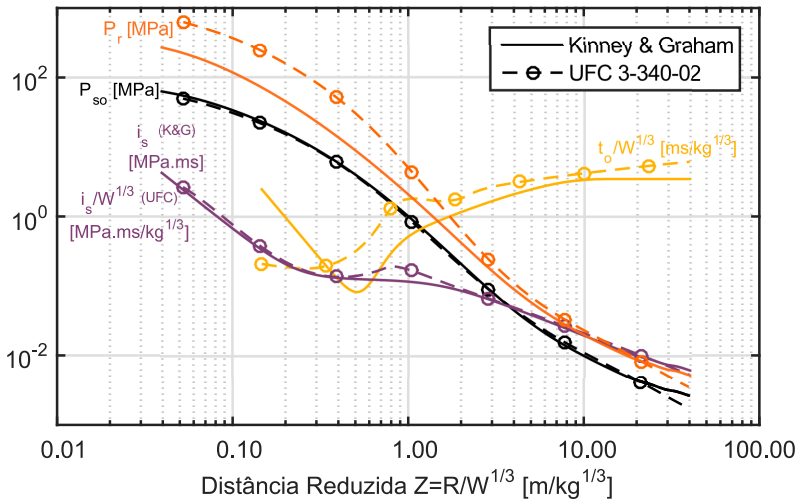
Figura 2: Grandezas características de uma explosão [13, 23]

No momento em que a onda de choque atinge a estrutura, é possível verificar a reflexão e amplificação da mesma. Caso a onda de choque embata perpendicularmente à superfície da estrutura, poderá classificar-se a reflexão como sendo uma reflexão normal. Como consequência, a onda de choque sofre um aumento de pressão para a pressão de pico refletida P_r, como observado na Figura 1(b), sendo que a duração das fase positiva e negativa se mantém inalteradas. Na Figura 2 encontra-se representada a estimativa da pressão de pico refletida definida pela UFC.

Adicionalmente, segundo Rankine-Hugoniot [35], é possível estimar a pressão de pico refletida a partir da pressão de pico incidente a partir da seguinte expressão:

$$P_r = 2P_{so}\left(\frac{7P_a + 4P_{so}}{7P_a + P_{so}}\right) \tag{5}$$

Por último, pode-se aproximar o impulso específico refletido se for conhecido o

impulso específico incidente, assumindo que a seguinte relação é valida [5]:

$$\frac{i_r}{i_s} \approx \frac{P_r}{P_{so}}$$

(6)

Propriedades dinâmicas dos materiais

Quando solicitados por cargas dinâmicas, os materiais têm mais resistência do que quando se encontram solicitados por cargas estáticas da mesma amplitude. Isto deve-se aos efeitos de inércia que dependem essencialmente da velocidade de deformação, geralmente expressa em s^{-1}. Para converter as propriedades dos materiais de cargas estáticas para dinâmicas, deve-se recorrer ao fator de amplificação dinâmica (*Dynamic Increase Factor* - DIF), que é diretamente proporcional à velocidade de deformação.

(a) Betão sujeito a compressão [30]

(b) Betão sujeito a tração [27, 30]

(c) Módulo de Elasticidade do betão [27, 30]

(d) Aço [27, 30]
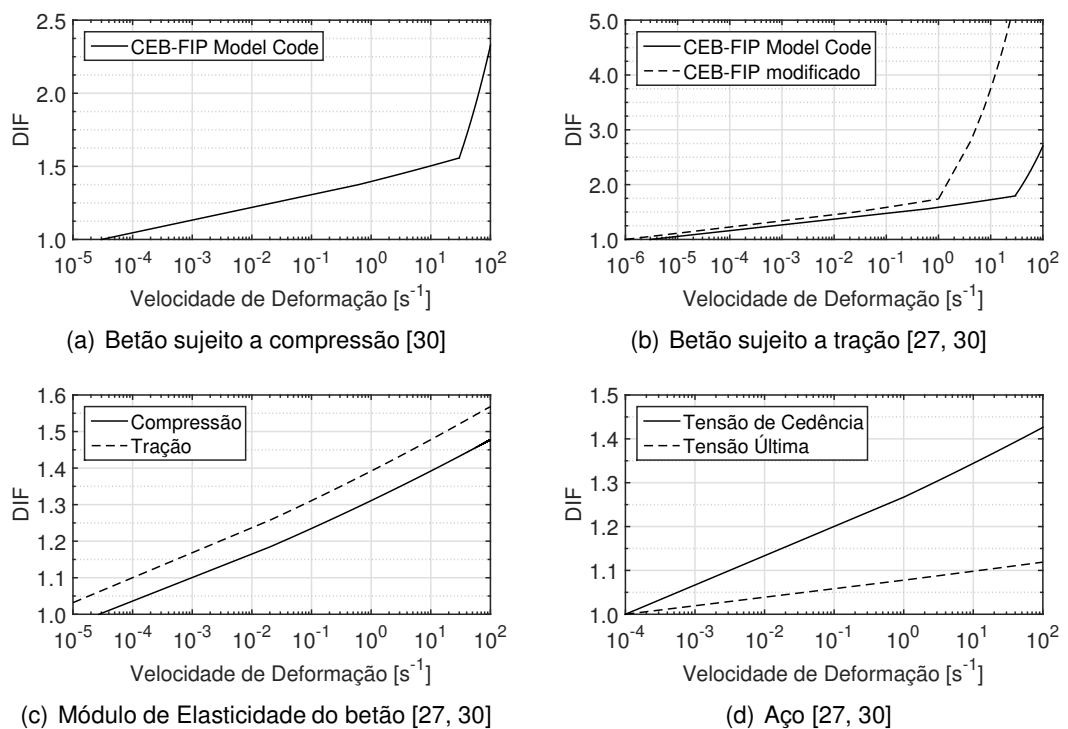
Figura 3: Fatores de amplificação dinâmica

Método dos Elementos Aplicados

O Método dos Elementos Aplicados (AEM) foi desenvolvido como parte integrante da pesquisa do Dr. Hatem Tagel-Din, resultando no programa de cálculo *Extreme Loading for Strutures* (ELS). Este permite a realização de análises dinâmica não-lineares com base no Método dos Elementos Aplicados [29, 31, 32, 33, 38, 46, 47, 48, 49].

Formulação do AEM

No AEM a estrutura é modelada através da divisão da mesma em elementos de menores dimensões, como representado na Figura 4(a). A ligação entre os diversos elementos é obtida através da colocação de molas, distribuídas ao longo da interface do elemento, que permitem o cálculo de deformações e tensões normais e tangenciais. Na Figura 4(b) é possível observar que as molas de ligação entre dois elementos permitem a definição das tensões e deformações de um determinado volume em análises tridimensionais ou de uma certa área em análises bidimensionais.

(a) Geração de elementos

(b) Volume de influência de cada par de molas
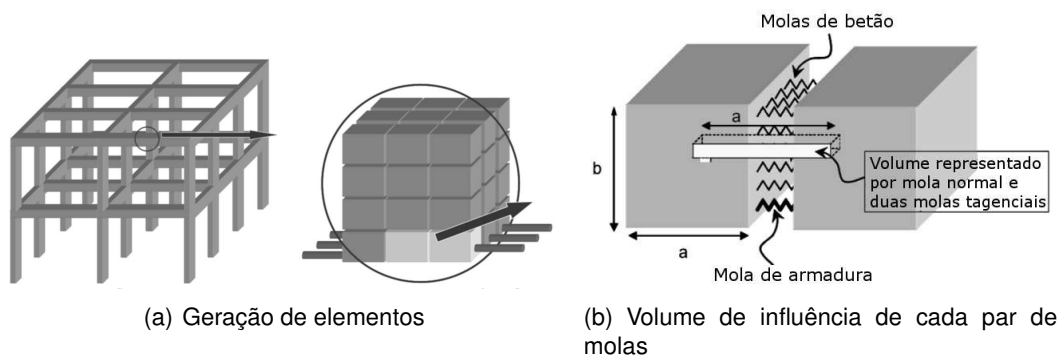
Figura 4: Modelação de estruturas com AEM (Adaptado de [2])

Os deslocamentos e rotações dos elementos são caracterizados através de 6 graus de liberdade (GDL), 3 para translações e 3 para rotações, no caso tridimensional ou através de 3 GDL no caso bidimensional. Adicionalmente, caso ocorram deslocamentos ou rotações relativas entre os elementos geram-se as tensões, nas molas localizadas na sua interface, ilustradas na Figura 5.

O Método dos Elementos Aplicados considera modelos constitutivos não-lineares para a simulação do comportamento dos diversos materiais que constituem as estruturas. Para o comportamento do betão à compressão é adotado o modelo elasto-plástico e de fratura de Maekawa [36]. Caso o betão seja sujeito a esforços de tração ou corte é assumido um comportamento linear até à rotura. Por último, para as armaduras é considerado o modelo constitutivo desenvolvido por Ristic [40]. Na Figura 6 é possível observar os modelos constitutivos referidos.

O Método dos Elementos Aplicados assume que o betão se encontra fendilhado quando a tensão principal atinge a resistência à tração do mesmo. Nos casos em que a fenda ocorre na direção da face do elemento, esta prolonga-se nessa mesma direção. No entanto, nos casos em que esta se inicia com uma inclinação em relação à face do elemento, o problema torna-se numericamente complicado. De modo a resolver este problema é possível considerar duas soluções. A primeira envolve a divisão dos elementos, enquanto que a segunda opta por redistribuir as tensões que se geram durante a fendilhação, conforme ilustrado na Figura 7. Considera-se que a primeira solução, apesar de precisa na simulação da transferência de tensões de corte, é demasiado complicada. Por isso, no ELS é adotada a segunda solução, que apesar de ser mais simples, permite o aumento da precisão com a diminuição da dimensão dos elementos.
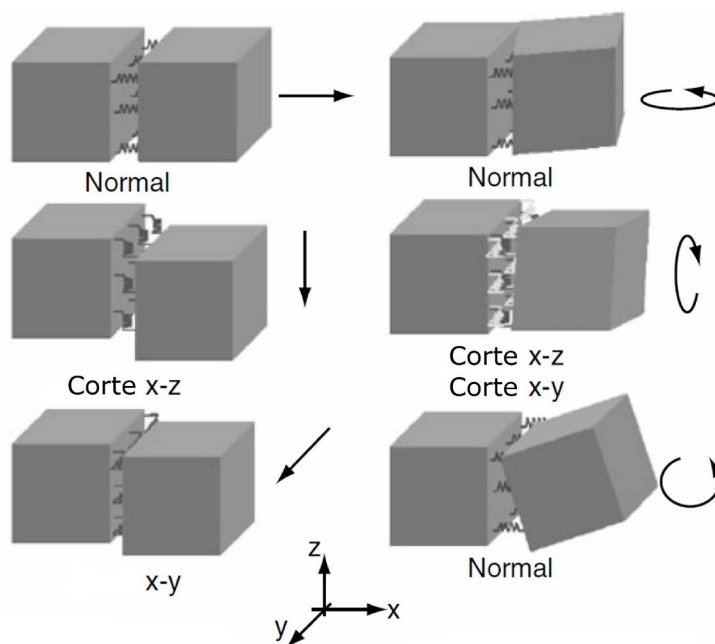
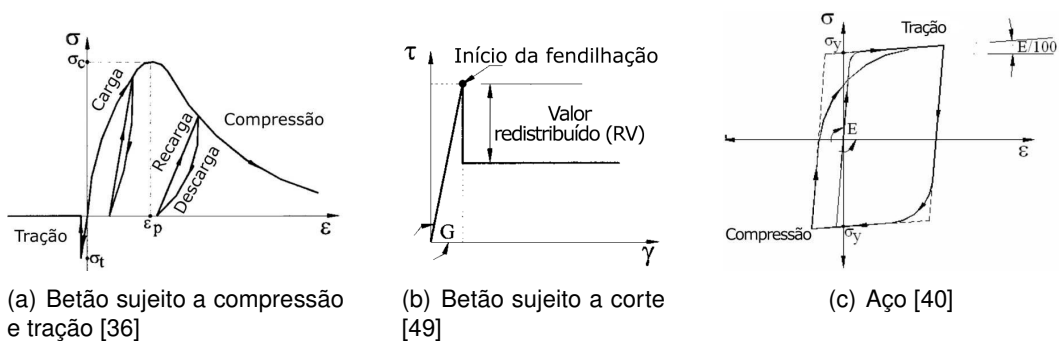Figura 5: Rotações e translações dos elementos (Adaptado de [4])

(a) Betão sujeito a compressão e tração [36]

(b) Betão sujeito a corte [49]

(c) Aço [40]

Figura 6: Modelos constitutivos
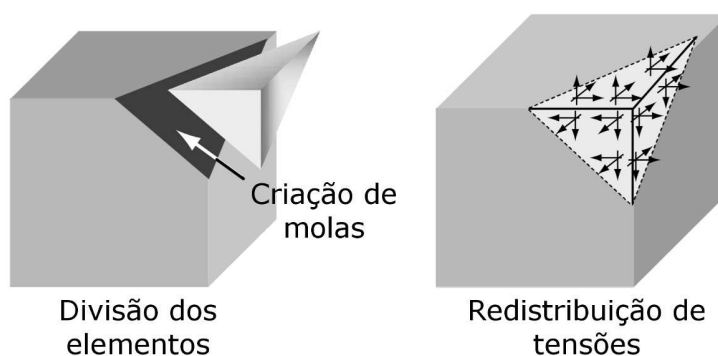

Divisão dos elementos

Redistribuição de tensões

Figura 7: Técnicas de simulação da fratura dos elementos (Adaptado de [4])

A formulação do AEM implementada no programa de cálculo ELS considera automaticamente a separação, o efeito de colisão e o "recontacto" entre os elementos. Para a simulação destes efeitos, a forma dos elementos é assumida como sendo circular (esférica no caso tridimensional), conforme se observa na Figura 8 e a colisão ou "recontacto" entre os elementos é detetada com base apenas na distância entre os centros dos elementos.
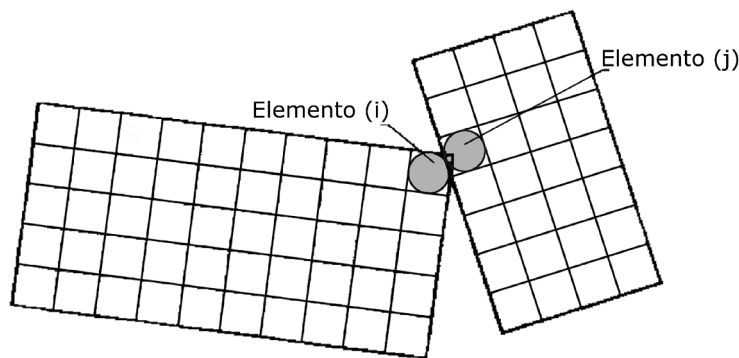
Figura 8: Colisão entre os elementos (i) and (j) (Adaptado de [46])

O Método dos Elementos Aplicados baseia-se no Método dos Deslocamentos, no qual uma matriz de rigidez geral é formulada e resolvida não-linearmente para os deslocamentos estruturais. A solução das equações de equilíbrio é obtida implicitamente através do método de integração dinâmica de Newmark Beta [37, 4].

Caso de Estudo

Na presente dissertação foram usados os testes experimentais apresentados por Gonçalves [18] como base de comparação de modo a verificar a aplicabilidade do AEM na simulação da resposta de placas de betão armado reforçadas com argamassas armadas quando sujeitas ao efeito de explosivos.

Definição dos modelos experimentais

De modo a estudar as melhorias no comportamento das estruturas, devido à aplicação de argamassas armadas, quando submetidas ao efeito de explosivos, foram criados quatro modelos experimentais a partir de painéis de fachada pré-fabricados de betão armado. Três destes modelos foram reforçados com soluções à base de calda de cimento armada, sendo que o quarto modelo experimental, sem reforço, serviu como referência. Todos os reforços efetuados têm 20 mm de espessura, diferindo apenas no tipo de armadura utilizada:

- Reforço A: Malha distendida galvanizada;

- Reforço B: 1 % de fibras de aço unidirecionais colocadas na direção do vão da placa;

- Reforço C: 0.5 % de fibras de aço em duas direções ortogonais.

A geometria final de cada modelo experimental, obtida através do corte dos painéis de fachada, foi de 2.6x2.17x0.12 m, como representado na Figura 9. A pormenorização de cada modelo era caracterizada por 2 malhas electrosoldadas NC50 e dois varões ϕ12 em 3 dos 4 lados dos modelos, formando um "U". Por último, é necessária a definição dos materiais que compõe os modelos experimentais:

- Betão: NP EN 206-1; C30/37; Cl 1.0; D$_{max}$ 1.4; F5;
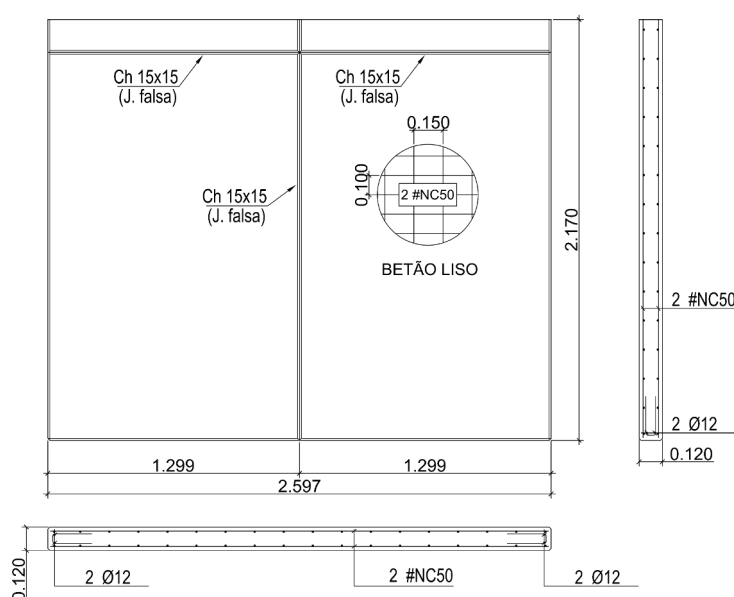
- Malha electrosoldada: A 500 ER;

- Varões: A 500 NR-SD.

Figura 9: Pormenorização do modelo experimental [18]

Ensaios experimentais dos modelos

Os ensaios experimentais foram realizados no campo militar de Santa Margarida com o auxílio do Exército Português no transporte, armazenamento e manuseamento dos materiais explosivos, de acordo com as suas regras de segurança. As cargas explosivas, TNT sob a forma de cargas para utilização militar, foram suspensas acima do centro dos modelos experimentais com o auxílio de um mecanismo em consola, conforme ilustrado na Figura 10. A distância entre o centro da carga e a face superior do modelo experimental foi medida durante o posicionamento da mesma através da medição do comprimento de uma corda. Após o posicionamento da carga, esta foi fixa ao solo de modo a evitar alterações da sua posição por ação do vento. Logo, é possível controlar ambos os parâmetros que definem a onda de choque gerada pela carga explosiva:

- Massa da carga explosiva, W_{TNT};
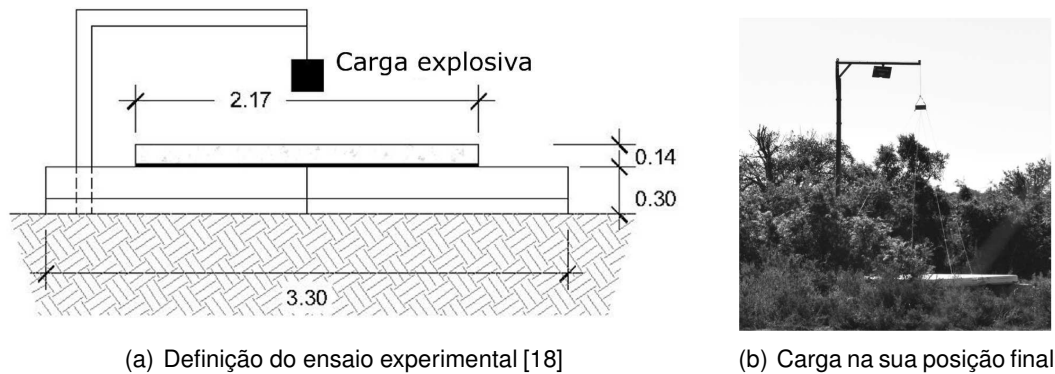
(a) Definição do ensaio experimental [18]　　　(b) Carga na sua posição final

Figura 10: Ensaio experimental

• Distância entre o centro da carga e a superfície do modelo experimental, R.

O objetivo dos ensaios experimentais foi o estudo da resistência de placas reforçadas com argamassas armadas, quando sujeitas ao efeito de explosivos. Portanto, de modo a obter uma melhor comparação, um dos modelos experimentais foi testado sem reforço. Simultaneamente, os modelos devem ser sujeitos aos mesmos efeitos. No entanto, estes efeitos devem provocar danos suficientes, de modo a torná-los visíveis, mas ao mesmo tempo, não causar o colapso do modelo experimental. A calibração do ensaio experimental foi realizada nos dois primeiros ensaios, sendo os dois seguintes para o ensaio dos modelos de referência e reforçado (B). Na Tabela 2 é possível observar as configurações usadas nos diversos ensaios. Repare-se que a distância apresentada nesta tabela corresponde à distância entre a face inferior da carga explosiva e a superfície superior do modelo experimental, pelo que deverá ser acrescida da distância entre a face inferior e o centro da carga explosiva na modelação numérica.

Tabela 2: Definição dos ensaios experimentais

Teste No.	Modelo	Massa TNT [kg]	Distância [m]	Objetivo
1	C	2	3	Calibração
2	C	8	2	Calibração
3	B	8	3	Ensaio
4	Referência	8	3	Ensaio

De modo a comparar os resultados dos diversos testes, torna-se necessária a utilização de um sistema de monitorização. Os deslocamentos residuais foram medidos com uma régua de alumínio de 2 m e uma fita métrica, conforme representado na Figura 11(a). O sistema de monitorização dos deslocamentos máximos foi composto por placas de poliestireno e hastes de metal, como representado na Figura 11(b). Durante o ensaio No. 3, o sistema de monitorização do deslocamento máximo sofreu danos devido à onda de choque. Contudo, considera-se que os resultados da zona central, composta por 4 hastes de arame, são fidedignos.
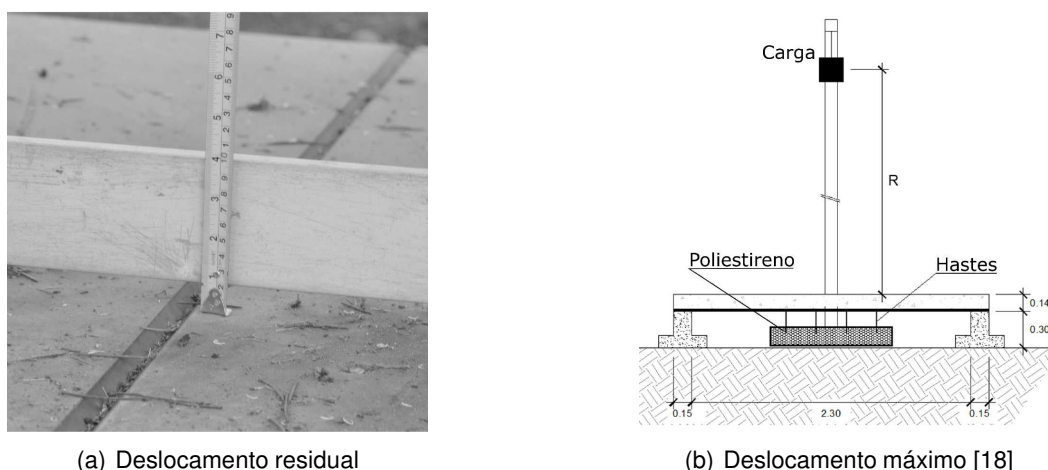
(a) Deslocamento residual

(b) Deslocamento máximo [18]

Figura 11: Sistema de monitorização

Resultados experimentais

Submetendo os modelos experimentais aos efeitos explosivos das configurações apresentadas na Tabela 2, obtém-se as deformações máxima e residual representadas na Tabela 3. Adicionalmente, observou-se que ambos os modelos possuíam fendilhação na face inferior, sendo esta caracterizada por uma fenda principal a meio vão com as larguras ao longo do seu comprimento representadas na Tabela 3.

Tabela 3: Deformações obtidas

Teste	Modelo	Def. max. média	Def. residual	Abertura fenda
[No.]	[-]	[mm]	[mm]	[mm]
3	B	33.5	10.0	1.3 - 2.5
4	Referência	65.0	20.0	2.0 - 3.0

Modelo numérico

O modelo numérico dos modelos experimentais foi criado com o auxílio do programa de cálculo *Extreme Loading for Strutures* v3.1 [15], que recorre ao Método dos Elementos Aplicados.

Calibração dos materiais

O ELS tem a capacidade de simular o comportamento não-linear dos materiais. Contudo, é necessário proceder à calibração dos modelos constitutivos adotados pelo programa. Para tal, foram realizados diversos ensaios experimentais ao materiais e, posteriormente, foram criados modelos no programa de cálculo de modo a calibrar os seus modelos constitutivos. Na Figura 12 é possível observar os modelos criados para o efeito. Note-se que o aço das armaduras e as fibras de aço presentes no reforço foram ambas modeladas com base no mesmo modelo, variando apenas o seu comprimento e diâmetro, pois assume-se que o

comportamento das fibras corresponde ao comportamento de uma armadura com o comportamento dos fios de aço a partir dos quais as fibras foram fabricadas.

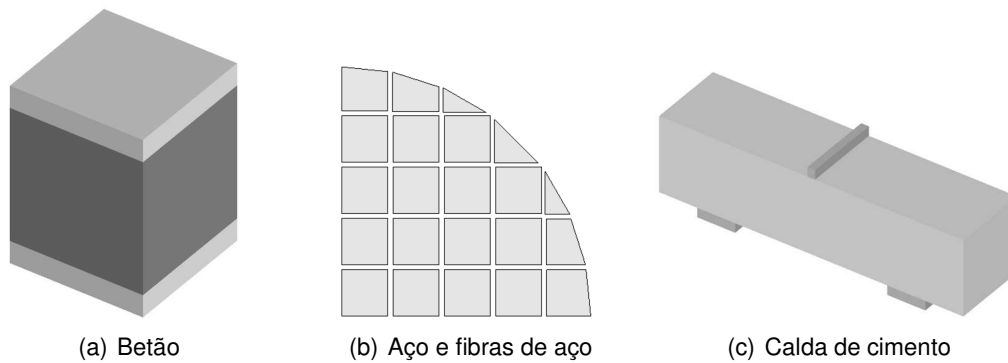(a) Betão　　　　　(b) Aço e fibras de aço　　　　　(c) Calda de cimento

Figura 12: Modelos ELS

Adicionalmente, na Figura 13, apresentam-se os resultados da calibração dos modelos constitutivos do betão, aço, calda de cimento e fibras.
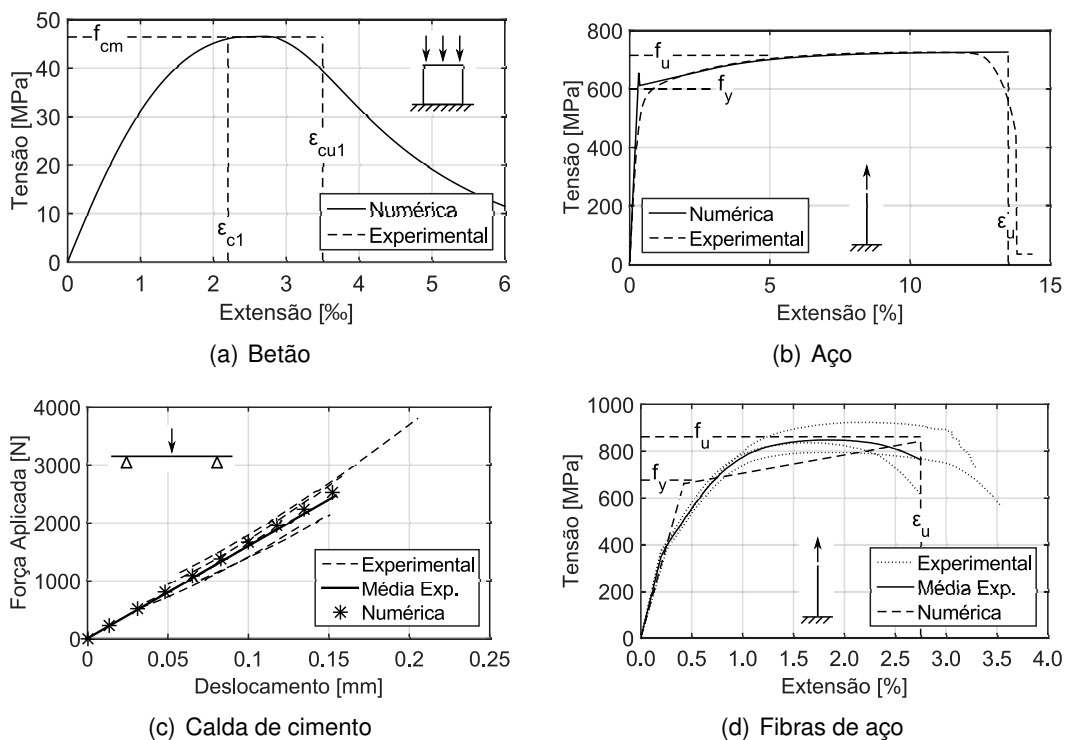

(a) Betão

(b) Aço

(c) Calda de cimento

(d) Fibras de aço

Figura 13: Calibração dos materiais

De seguida, procedeu-se à modelação do modelo experimental de referência, de acordo com o projeto ilustrado na Figura 9.

Análise de convergência e sensibilidade
Na presente dissertação, a calibração e validação do modelo numérico foram baseadas nos resultados obtidos no teste No. 4, em particular, para o

deslocamento residual obtido neste ensaio.

A análise de convergência da malha do modelo foi realizada através da aplicação de uma carga de 50 kN, estaticamente aplicada em 1000 passos e distribuída por todos os elementos. A escolha deste valor de carga permite o estudo da estabilidade da solução numérica em todas as fases do comportamento estrutural do modelo, pois garante a rotura do mesmo. Analisando a Figura 14(b), é possível verificar que uma malha composta por 86x45x4=15480 elementos com 5x5 pares de molas normais e de corte nas interfaces comuns entre os elementos conduz a resultados fidedignos e precisos com um esforço computacional e tempo de análise razoável.

(a) Geometria da laje

(b) Força aplicada-deslocamento
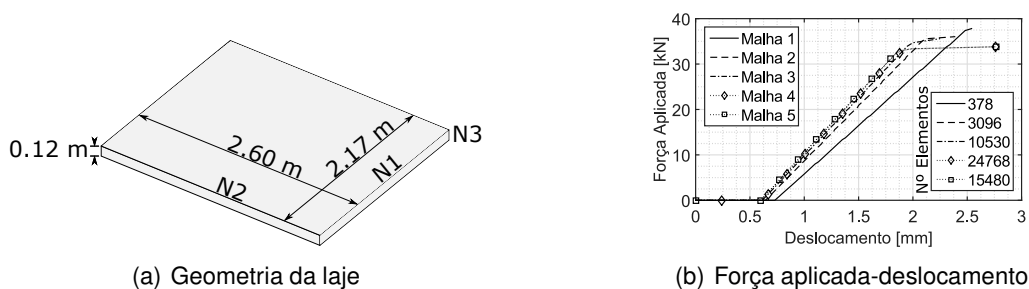
Figura 14: Análise de convergência da malha

Após a verificação da convergência da malha, o modelo numérico foi sujeito aos efeitos dos explosivos do respetivo ensaio experimental, sendo a análise efetuada num processador Intel Xeon CPU 5670 a 2.93 GHz e 16 GB de RAM. Devido ao pico quase instantâneo de pressão associado às detonações, é necessária a utilização de um intervalo de tempo bastante reduzido de modo a obter uma simulação correta da variação da pressão com o tempo. Logo, o intervalo de tempo usado, desde a detonação até se verificarem sobrepressões nulas na face superior da laje, foi 10^{-4} s. Após esta fase, que dura aproximadamente 0.05 s, recorreu-se a um intervalo de tempo de 10^{-3} s nos 1.95 s seguintes, permitindo o estudo do comportamento do modelo após os efeitos da explosão. O tempo de análise necessário para calcular os resultantes 2450 passos de análise foi de aproximadamente 8-10 horas.
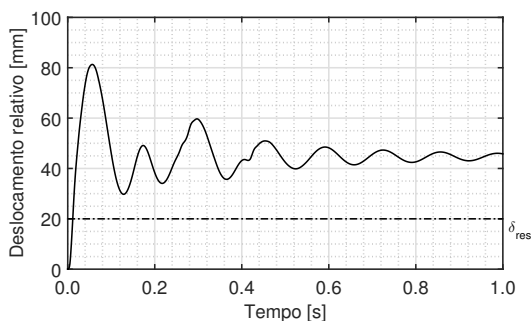


Figura 15: Relação deslocamento relativo-tempo inicial

Através da análise do resultado numérico ilustrado na Figura 15, verifica-se uma

diferença entre o deslocamento residual obtido experimentalmente, representado nesta figura como δ_{res}, e o deslocamento relativo obtido numericamente, que corresponde ao deslocamento medido pela régua no ensaio experimental. Por conseguinte, verifica-se a necessidade de calibrar o modelo numérico de acordo com o resultado experimental.

Tendo em conta que os apoios do modelo experimental foram vigas em T invertidas, considerou-se inicialmente que o material que os constituía era o *High Strength Concrete*, definido no ELS, e que estes se encontravam encastrados na sua base, ou seja, que a rigidez do solo era muito elevada. No entanto, através da análise da Figura 15, verifica-se a necessidade de considerar a dissipação de energia do solo no modelo numérico. Contudo, a modelação do solo levaria a um grande esforço computacional, pelo que se optou por modelar a influência do solo nos apoios, que serão modelados com um comportamento elástico. Assumindo um $N_{SPT} = 15$ para o solo, foi possível, através da relação proposta por Stroud [44], estimar o Módulo de Elasticidade do solo como sendo $E = 20.7$ MPa. De seguida, através da modelação de um apoio com o solo, ilustrado na Figura 16(a), foi possível definir o comportamento do apoio e do solo em série e, seguidamente, implementado no apoio elástico final. A relação força aplicada-deslocamento representada na Figura 16(b) resulta da aplicação de uma força estática de 2440 kN ao apoio para ambos os casos, de onde se pode verificar a correcta implementação do comportamento em série no apoio final.
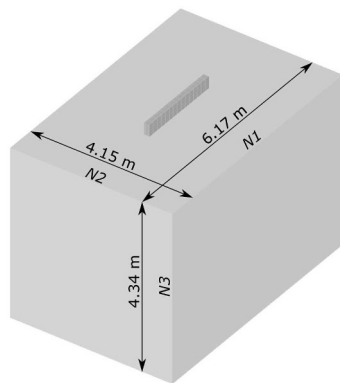

(a) Modelo apoio e solo
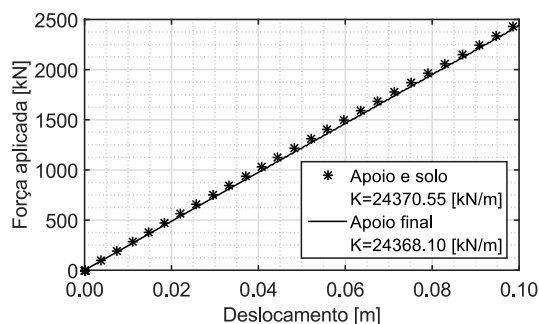
(b) Relação força aplicada-deslocamento

Figura 16: Determinação do comportamento do solo

Inicialmente, o amortecimento nos apoios foi considerado como nulo, levando a que a dissipação de energia seja nula, o que poderá não ser correto pois o solo dissipa energia e o apoio final simula o comportamento do solo e do apoio. Logo, foi realizada uma análise modal com o objetivo de obter o primeiro modo de vibração axial da estrutura, representado na Figura 17(a). De seguida é possível implementar o coeficiente de amortecimento $r = 2\zeta\omega_1 = 9070.92$ s⁻¹, admitindo um amortecimento crítico do apoio, conforme ilustrado na Figura 17(b). Adicionalmente, nessa mesma figura, encontra-se representado o comportamento elástico ($r = 0$ s⁻¹) do apoio.

Através da consideração de um material com fracas características mecânicas foi

possível obter uma correta simulação da interface entre o modelo e os apoios do modelo experimental. No entanto, o programa de cálculo *Extreme Loading for Structures* considera por definição um valor para a rigidez de contacto normal de $N_F = 0.01$, que levou à rotura das molas de interface entre o modelo experimental e os apoios, ilustradas como círculos na Figura 17(c). De modo a não se verificar esta rotura, considera-se que um valor de rigidez de contacto normal $N_F = 1$ é mais apropriado do que o assumido no programa de cálculo. Na Figura 17(d) observa-se tanto o resultado inicial, como os resultados obtidos através da consideração do comportamento do solo nos apoios e de um valor unitário para a rigidez de contacto normal N_F. Analisando a figura, conclui-se que ambas as considerações melhoram o resultado numérico.
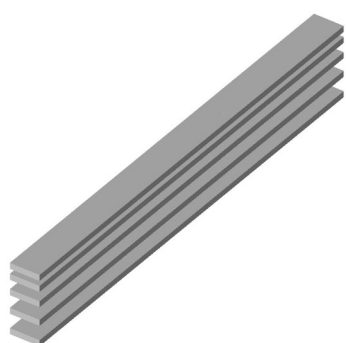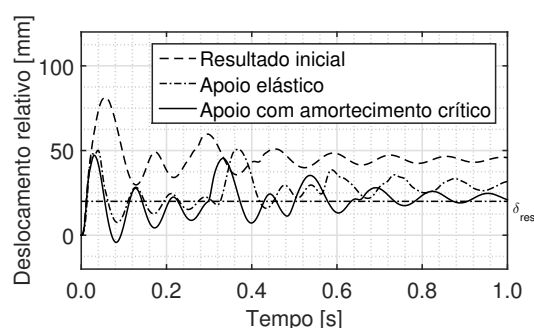
(a) Primeiro modo de vibração axial ($\omega_1 = 4535.36$ rad/s)
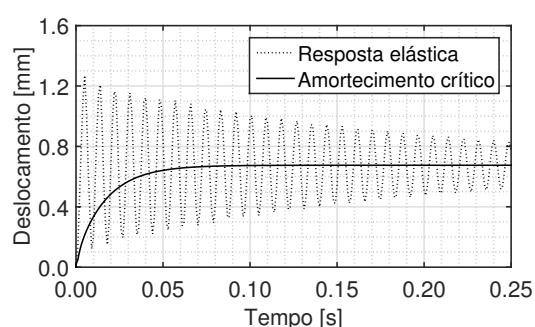
(b) Resposta elástica e amortecida do apoio final
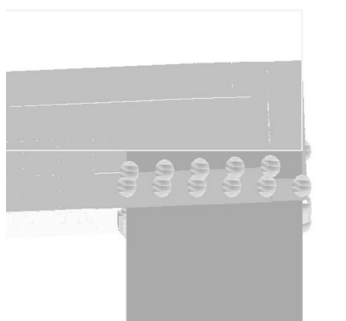
(c) Rotura das molas de contacto

(d) Influência do solo e da N_F na curva deslocamento relativo-tempo

Figura 17: Calibração do resultado numérico do modelo de referência

Por último, deve-se considerar os efeitos de inércia devidos às elevadas velocidades de deformação através da aplicação dos respetivos Fatores de Amplificação Dinâmica (DIF). O processo inicia-se com a análise do modelo numérico considerando DIF=1, permitindo assim o cálculo de DIFs atualizados para as velocidades de deformação obtidas nesta analise. De seguida, o processo deve ser repetido até não se verificarem diferenças significativas entre os DIFs. Deste processo resultaram os valores apresentados na Tabela 4 para ambos os modelos.

Tabela 4: DIFs obtidos

Material	Propriedade	Modelo referência	Modelo B
Betão	f_{cm}	1.40	1.35
	f_{ctm}	1.59	1.53
	E_{cm}	1.35	1.32
Aço	f_y	1.32	1.31
	f_u	1.09	1.09

Resultados numéricos e comparação

Apresentam-se na presente secção os resultados obtidos numericamente e a sua comparação com os resultados experimentais. Através da análise da Figura 18 é possível verificar que os resultados obtidos experimental e numericamente se encontram bastante próximos entre si, tanto para os deslocamentos como para o padrão de fendilhação presente na face inferior do modelo após o ensaio. Adicionalmente, verifica-se que o padrão de fendilhação do modelo B se aproxima mais do resultado experimental do que o padrão observado no modelo de referência. Esta menor aproximação do modelo de referência poderá dever-se à inexistência da junta falsa no modelo numérico, devido ao elevado número de elementos de pequena dimensão necessário para assegurar uma modelação correta da mesma, criando assim uma maior distribuição de tensões que poderá não ter existido no modelo experimental devido à presença da junta falsa, que gera uma concentração de tensões e posterior falha concentrada.

(a) Modelo de referência

(b) Modelo B

(c) Fendilhação do modelo de referência
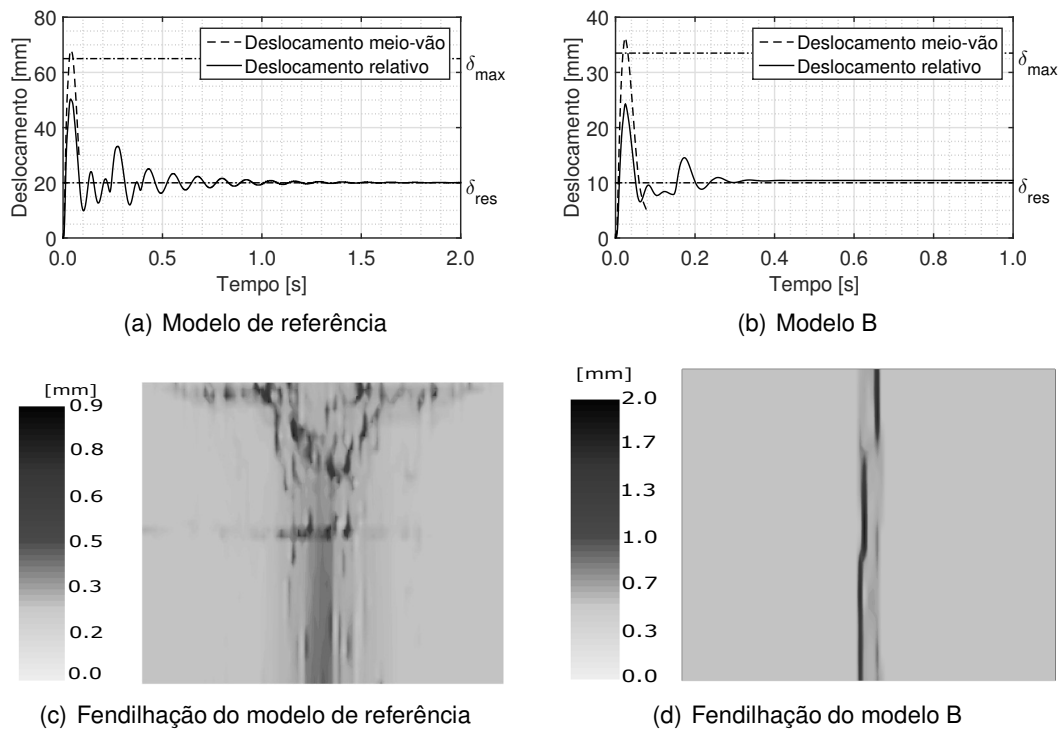

(d) Fendilhação do modelo B

Figura 18: Comparação entre os resultados obtidos

Nas Tabelas 5 e 6 observa-se que as diferenças entre os deslocamentos obtidos por ambos os métodos são razoáveis e verifica-se que, tal como esperado, as diferenças obtidas para o modelo de referência são menores do que as diferenças para o modelo B. Este facto poderá dever-se à inexistência de medições de pressões aplicadas no modelo experimental, que dependem grandemente das condições ambiente e à modelação do solo com propriedades incertas. No entanto, é possível concluir que o Método dos Elementos Aplicados consegue prever e simular com precisão a resposta de placas de betão armado com argamassas armadas quando sujeitas ao efeito de explosivos.

Tabela 5: Diferenças entre os resultados do modelo de referência

Deslocamento [mm]	Máximo	Residual
Modelo experimental	65.0	20.0
Modelo numérico	68.0	20.0
Diferença [%]	4	0

Tabela 6: Diferenças entre os resultados do modelo B

Deslocamento [mm]	Máximo	Residual
Modelo experimental	33.5	10.0
Modelo numérico	37.3	10.4
Diferença [%]	10	4

Conclusão

A colaboração com a Academia Militar Portuguesa, tornou possível a campanha experimental no campo militar de Santa Margarida, permitindo a definição da resposta ao efeito de explosivos de um painel de betão armado (modelo de referência) e de um painel de betão armado reforçado com argamassas armadas (modelo B). No entanto, a inexistência de definição para as condições de fronteira, especificamente para as características do solo no local de ensaio, e a falta de dados de pressão medidos nos ensaios experimentais, gerou dificuldades no processo de calibração do modelo numérico criado no programa de cálculo *Extreme Loading for Structures*.

Não obstante, a calibração do modelo referência sujeito aos efeitos de uma detonação foi realizada com sucesso. De seguida, recorrendo aos parâmetros calibrados, foi simulado o comportamento do modelo B quando sujeito ao cenário de explosão. Através da análise dos resultados numéricos e subsequente comparação com os resultados experimentais é possível concluir que o Método dos Elementos Aplicados consegue prever e simular com precisão a resposta de placas de betão armado com argamassas armadas quando sujeitas ao efeito de explosivos. Adicionalmente verifica-se que as diferenças observadas no modelo B poderão dever-se à falta de definição das condições de fronteira, que influenciam grandemente os resultados das análises dinâmicas. Para o caso de estudo, as

condições de fronteira relacionadas com o solo e com as propriedades dos materiais em contacto foram modeladas com incertezas devido à inexistência de definição para as mesmas.

Contents

List of Figures

List of Tables

List of Abbreviations, Acronyms and Symbols

Abbreviations

DOF	Degree of Freedom
EC2	Eurocode 2
K&G	Kinney and Graham
R-H	Rankine-Hugoniot

Acronyms

AEM	Applied Element Method
CFD	Computational Fluid Dynamics
DIF	Dynamic Increase Factor
EDEM	Extended Distinct Element Method
ELS	Extreme Loading for Structures
FCT	Faculdade de Ciências e Tecnologia
FEM	Finite Element Method
RC	Reinforced Concrete
UFC	Unified Facilities Criteria
UFRG	Unidirectional Fibre Reinforced Grout
UNL	Universidade Nova de Lisboa

Symbols

α	Angle of incidence of the shock wave
β	Crack inclination angle relative to the element's edge
γ	Ratio of specific heats
$\boldsymbol{\Delta f}$	Incremental applied load vector for static analysis
$\boldsymbol{\Delta f}(t)$	Incremental applied load vector for dynamic analysis
$\boldsymbol{\Delta u}$	Incremental displacement vector
$\boldsymbol{\Delta \ddot{u}}$	Incremental acceleration
$\boldsymbol{\Delta \dot{u}}$	Incremental velocity vector
$\boldsymbol{\Delta \ddot{u}_G}$	Incremental gravity acceleration vector
δ_{max}	Experimental maximum displacement
δ_{res}	Experimental residual displacement

$\dot{\varepsilon}$	Strain rate
ε_{c1}	Strain at maximum compression stress for concrete
ε_{cu1}	Ultimate compression strain for concrete
ε_u	Ultimate strain for steel
ζ	Damping ratio
σ_1, σ_2	Principal stress components
τ	Shear stress component
ω_1	Structure's fundamental frequency
Ω	Strain energy

a	Length of the representative area
A	Contact area
b	Element's height
$\boldsymbol{C}$	Matrix of damping
C_0	Speed of sound in air
C_D	Drag cofficient
C_E	Equivalent/uniform load factor
C_r	Reflected overpressure ratio; Sound velocity in overpressure region
d	Effective depth; Distance between springs
E	Young's modulus
E_1	Post Yield Young's Modulus for steel
$\boldsymbol{f}$	Applied load vector
f_{cm}	Mean compressive strength of concrete and grout
f_{ceq}	Concrete's modified compressive strength
$f_{c,cube}$	Mean cubic compressive strength of concrete
f_y	Tensile yield stress of steel
f_u	Ultimate strength of steel
$\boldsymbol{f_m}$	Element's force vector
G	Shear modulus
H_T	Height of the triple point
i_r	Reflected specific impulse
i_s	Specific impulse
$\boldsymbol{K}$	Non-linear stiffness matrix
$\boldsymbol{K_G}$	Global stiffness matrix
K_n	Spring's axial stiffness
K_r	Spring's rotational stiffness
K_s	Spring's shear stiffness
L_w	Wave length of the shock wave
$\boldsymbol{M}$	Matrix of mass
M_{rd}	Moment capacity
n	Ratio between the unloading and loading stiffness
N_F	Normal contact stiffness ratio
N_{SPT}	Blow count of the Standart Penetration Test
P_r	Peak reflected overpressure
P_a	Atmospheric pressure
P_{so}	Positive overpressure

P_{so}^{-}	Negative overpressure
q_s	Peak dynamic pressure
R	Distance from the burst's origin
r	Damping ratio
$\boldsymbol{r_G}$	Residual force vector due to geometrical changes
$\boldsymbol{r_m}$	Residual force vector due to material non-linearity
RV	Redistributed value
S	Clearing distance
S_F	Shear contact stiffness ratio
T	Kinetic energy; Element's thickness
t_A	Shock wave's arrival time
t_c	Clearing time
t_d	Rise time
t_o	Positive phase duration
t_o^{-}	Negative phase duration
t_{of}, t_{rf}	Duration of the equivalent triangular impulse
$\boldsymbol{u}$	Displacement vector
U	Shock front velocity
W	Weight of explosive
Z	Scaled distance

Chapter 1

Introduction

"The military sappers and miners of one generation become the quarry blasters of another."
*(*P. S. Bulson*)*

1.1 Background

Over the course of history, there has been a constant drive to design structures which withstand the effects of gravity, wind, temperature changes and earthquake's actions. However, over the last few decades, wars, terrorist attacks and accidental explosions established the need to consider blast loads in the design of important structures, since an explosion within or surrounding a building can result in disastrous effects, causing not only structural damage or failure but also the loss of human life [10].

Therefore, blast protection has the goal of containing damage to the immediate vicinity of the explosion and prevent progressive collapse, and ultimately, the preservation of both buildings and human lives. In this sense, numerical simulations could prove to be valuable tools, as they allow to test a wide range of building types, blast protections and reinforcements over a broad range of hypothetical events.

However, blast scenarios result in highly dynamic loading conditions, which nowadays represent a challenge in structural engineering. Under such load regimes, investigations on structural performances cannot be conducted without considering aspects which are typically neglected under static loading conditions, e.g. large displacements, material characteristics under high strain rates, and fluid dynamics [4].

In fact, throughout history, society has been faced with numerous challenges, e.g. wars and terrorism, from which designers took valuable lessons. On April 19, 1995, a truck containing about 2200 kg of ammonium nitrate fertilizer, nitromethane and diesel fuel mixture, the equivalent of over 2300 kg of TNT, exploded in front of the Alfred P. Murrah Federal Building in Oklahoma City, Oklahoma. The blast collapsed

a third of the building, gouged out a crater 9.14 m wide by 2.44 m deep and destroyed or damaged 324 buildings in a 16-block radius [42].

The collapse of the building, illustrated in Figure 1.1, resulted from the destruction of the first floor columns, which supported a 12 m long transfer girder (also represented in this figure). Consequently, the failure of the transfer girder led to the collapse of two adjacent columns, triggering the progressive collapse and the destruction of most of the front of the building. However, due to two massive shear walls, the building experienced only partial collapse, which decreased the injuries and loss of lives [42].
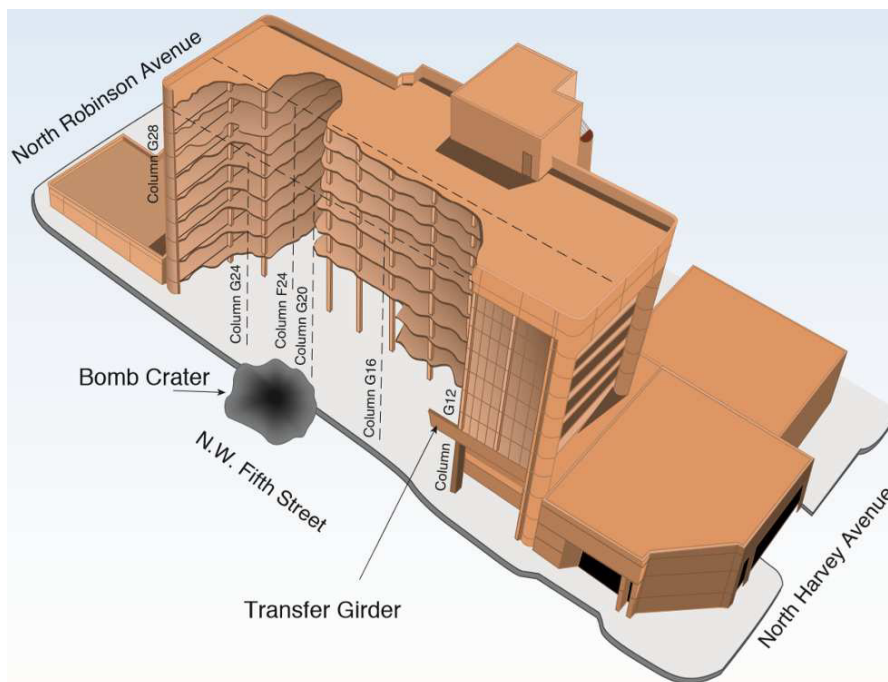
Figure 1.1: Alfred P. Murrah Federal Building's progressive collapse [42]

Around the world, pre-cast and pre-stressed concrete structures are usually used in urban residential constructions. However, pre-cast panels are typically supported at the ends unless they span over multiple floors and the panels are not bolted together. This might constitute a problem in resisting both the direct blast loads and uplift loads resultant from a blast [42].

In 1996, a large truck containing approximately the equivalent to 9000 kg of TNT attacked the Khobar Towers military housing in Saudi Arabia, a pre-cast concrete structure. Despite the large amount of explosive material, due to the larger distance of the charge to the building, 25 m, and to the bolted connections designed according to the British standards for blast-resistant structures, the damage resulting from the detonation, depicted in Figure 1.2, was less extensive than the damage of the Alfred P. Murrah Federal Building.

Figure 1.2: Khobar Towers damage after the bombing [42]

On the other hand, civil society also faces the danger of explosions resultant from accidental explosions. As an example, in August 2015, a warehouse for hazardous materials at the port of Tianjin, China, exploded twice as a consequence of a fire of unknown origin, leading to a massive loss of lives and severe injuries and to significant material losses. The warehouse contained hazardous and flammable chemicals, such as calcium carbide, sodium cyanide, potassium nitrate, ammonium nitrate and sodium nitrate. It is estimated that the first explosion had an equivalent weight of 3000 kg of TNT, while the second one had an equivalent weight of 21000 kg of TNT [8]. In Figure 1.3 it is possible to observe a building damaged by the explosions.
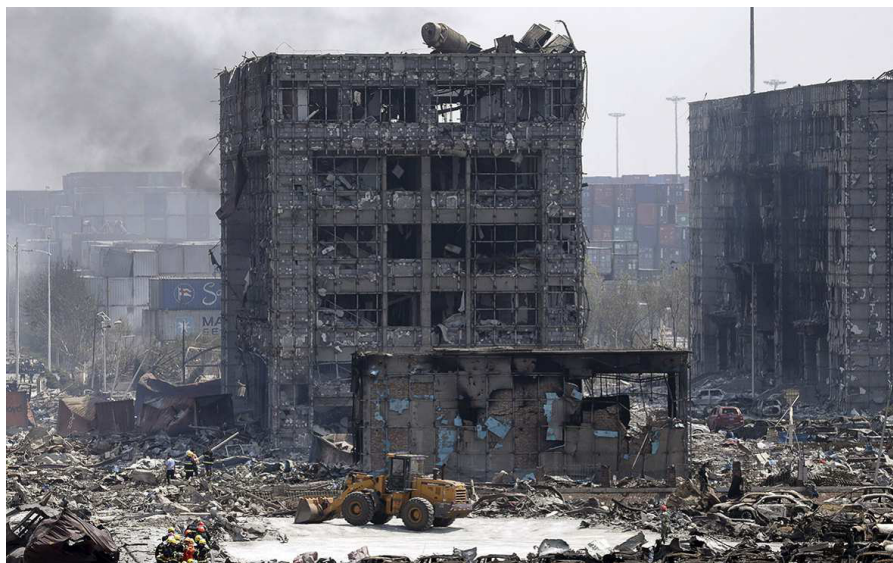
Figure 1.3: Building damaged by Tianjin explosions [41]

An explosion may inflict severe damage and represent a major disaster, as observed in the previous examples. Hence, in order to minimize such effects, knowledge of the mechanisms of explosion damage becomes essential. Only then it is possible to design and build explosion resistant facilities [23].

However, the cost of providing a safe environment for research in this specific area is very high. Therefore, in most countries, the experimental work has been assigned to the armed forces, government research facilities or to large industrial explosive manufacturers, leading to results that are not openly reported due to security restrictions [7].

The physics of the detonation process is of interest, from initiation to the formation of the shock front and blast wave. This has been well documented by Kinney and Graham [23], Baker [5], Henrych [19] and in the UFC [13]. According to [23], *"an explosion is a phenomenon resulting from a sudden release of energy"* and does not give any type of warning because the shock front travels faster than the speed of sound. The representative effects of a blast wave, based on nuclear explosions, with its origin to the right of the represented building, are illustrated in Figure 1.4 and the typical pressure-time curve is plotted in Figure 1.5.

At time A defined in these figures, the atmosphere is still undisturbed. At time B, immediately after the impact of the shock front, a force, which is proportional to the pressure rise and the impact area, is applied to the wall. Additionally, the subsequent blast wind also exerts a force. These blast effects then decrease quasi-exponentially with time until the pressure reaches the value of the atmospheric pressure. Afterwards, there is a slight negative phase, along with a reversed blast wind, defined as time C in these figures. Finally, there is a dissipation of the negative pressure until the value of the atmospheric pressure is reached, represented as time D [23].

Due to the severity of these effects, it becomes necessary to design structures or reinforcements to withstand them. However, the empirical research of the blast loads depends on a safe environment, which results in very high costs. Therefore, one might resort to computational methods to simulate the structures' behaviour when subjected to blast loads.

As previously stated, blast scenarios result in highly non-linear dynamic loading conditions. Thereby, in order to predict a correct structural response one must resort to complex numerical formulations. These formulations must be able to simulate the mechanical and geometric characteristics of the structure, as well as its interaction with the shock wave.

The Finite Element Method is the most used computational method in the simulation and analysis of the behaviour of structures due to its versatility in modelling complex geometries and its simple implementation in computer software. Although it generally produces accurate results, the simulation of the collapse of structures involves complex and time-consuming techniques, hindering the application of this method in the simulation of blast scenarios.

A. BEFORE BLAST WAVE STRIKES.

B. IMMEDIATELY AFTER PASSAGE OF THE SHOCK FRONT.

C. IN NEGATIVE OVERPRESSURE PHASE WITH REVERSED BLAST WIND.

D. AFTER BLAST WAVE SUBSIDES.
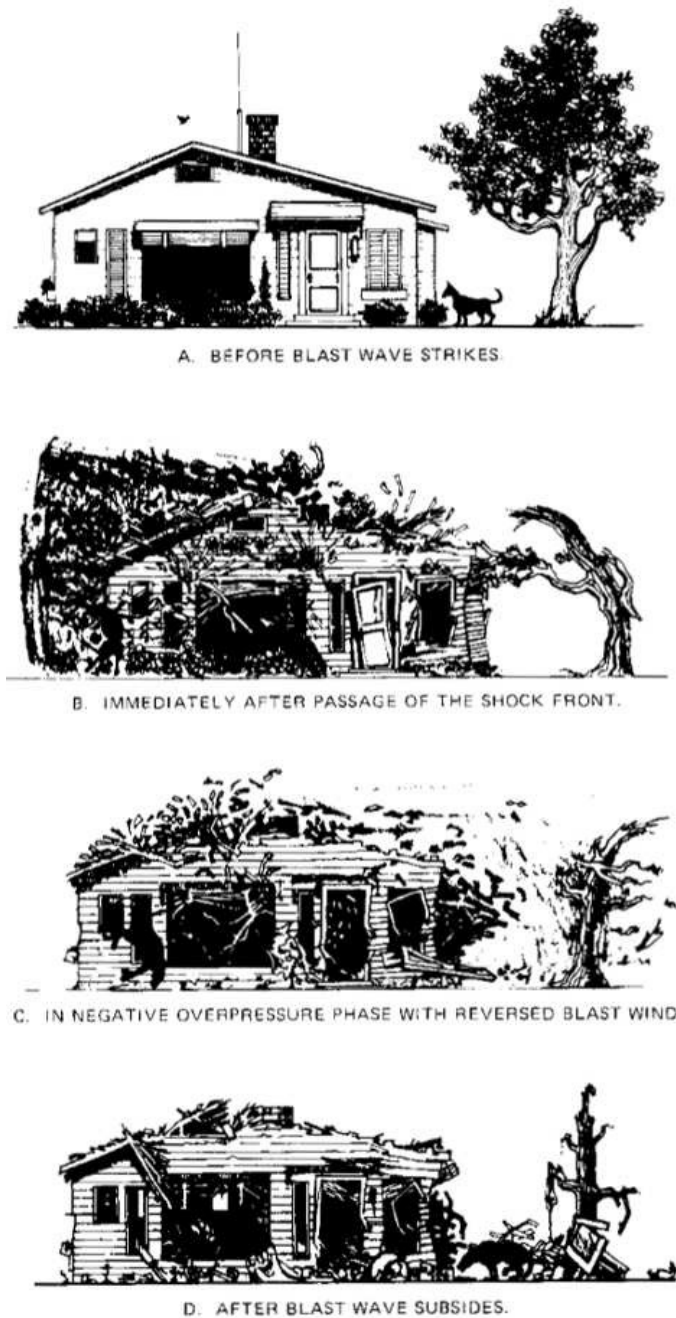
Figure 1.4: Representation of blast wave effects [23]

The Applied Element Method, reviewed further in Chapter 3, is a non-linear numerical method, which allows the simulation of structures' behaviour when subjected to any load. Hence, it is possible to simulate the structure's behaviour from the moment of the loads' application until the moment when the structure collapses, through the elastic phase, crack opening and propagation, reinforcement yield and collision of materials.
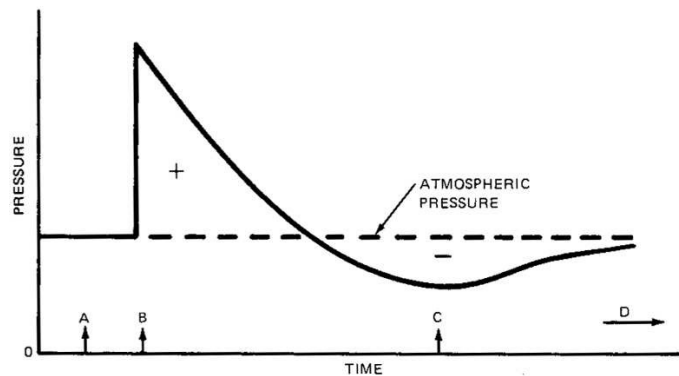
Figure 1.5: Blast wave pressures plotted versus time [23]

In Figure 1.6, it is possible to observe the simulation of the Alfred P. Murrah Federal Building bombing with the Applied Element Method, implemented in the commercial software *Extreme Loading for Structures* [15]. If one compares the progressive collapse represented in this figure with with the one illustrated in Figure 1.1, one can observe the similarity between the numerical model's results and the reality.

Figure 1.6: Simulation of A.P. Murrah Federal Building bombing [3]

1.2   Objectives and scope

The present dissertation aims to simulate the response of fibre grout reinforced RC panels when subjected to blast effects from unconfined explosions using the Applied Element Method, in order to validate and verify the applicability of this method in the simulation of explosions. It is meant as a part of the *Segurança e Integridade Estrutural de Edifícios Estratégicos face a explosões acidentais*

ou provocadas - SI4E project in partnership between the FCT/UNL and the Portuguese Military Academy.

The prefabricated fibre grout strengthened RC panels were subjected to a set of experimental tests in order to evaluate their response when subjected to blast effects and establish a comparison base for the numerical simulation.

The numerical modelling was performed with the commercial software *Extreme Loading for Structures*, which is based on the Applied Element Method. The reference model was calibrated using the obtained experimental results in order to ensure a correct numerical analysis.

Hereupon, through numerical simulations, the intended purpose is to infer the predictability of the Applied Element Method when used to simulate blast effects on structures. This inference is performed through the appraisal of the numerical results, namely the maximum and residual displacements and the cracking on the bottom surface of the model, in comparison to the experimental test results.

1.3 Dissertation outline

The content of the dissertation is organized into the following five chapters:

Chapter 1 General approach to the subject of the dissertation and analysis of the state-of-the-art.

Chapter 2 Review of the main effects of an explosion through a survey of different formulations and a comparison of the characteristics defined by them. Application of a blast scenario to the case study to provide a better comparison between the characteristics defined by the different formulations. Study of the changes in the properties of the materials when subjected to dynamic loads.

Chapter 3 Study of the theoretical concepts and formulation of the Applied Element Method and its implementation into the commercial software *Extreme Loading for Structures*.

Chapter 4 Description of the experimental tests, reported by Gonçalves [18]. Definition and calibration of a numerical model to allow the correct simulation of the experimental tests. Numerical analysis of the blast effects on slabs and subsequent assessment and comparison with the experimental tests.

Chapter 5 Summary of the research, conclusions and suggestions for future work.

1.4 State-of-the-art

In 2013, Tabatabaei *et al* [45], studied the addition of long carbon fibres to traditional reinforced concrete as a way to improve the blast spalling resistance

of concrete. In order to obtain a comparison of the blast resistance of conventional reinforced concrete (RC), which was tested as a control specimen, and long carbon fibre reinforced concrete (LCFRC), a series of blast tests, whose set-up is defined in Figure 1.7, were conducted.
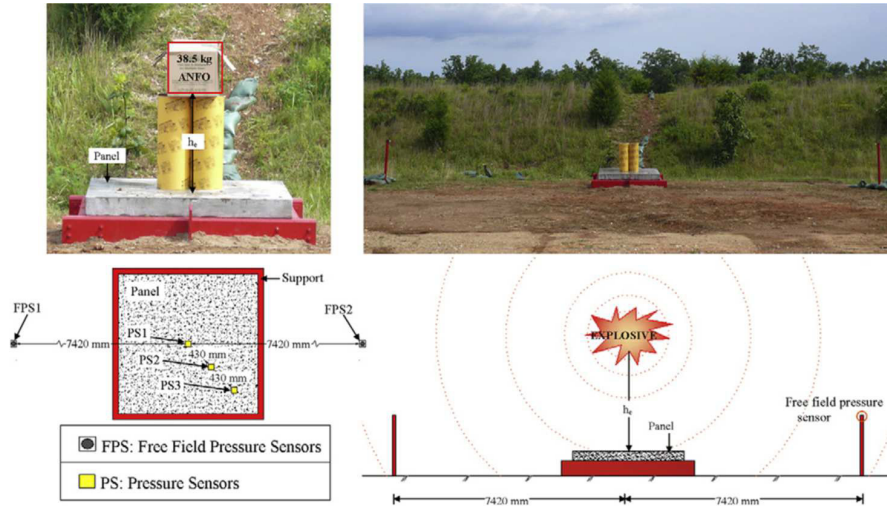
Figure 1.7: Blast test set-up and sensor locations [45]

Furthermore, finite element models were created in LS-DYNA to replicate both a control panel and a LCFRC panel to observe the applicability of the FEM in predicting the models' damage. To ensure a correct pressure simulation, both the free-field incident pressure and the reflected pressure for each panel were measured with pressure sensors, whose location is defined in Figure 1.7.

The blast spalling resistance was evaluated through visual and physical measurement of the damage. The physical measurement consisted in the evaluation of the weight before and after the blast test and the definition of the percentage of surface damage of the front and back faces of the specimens. Afterwards, the obtained experimental results were compared with the UFC and McVay's spall and breach prediction curves for reinforced concrete slabs subjected to detonations. These prediction curves revealed a good agreement for the control specimens. However, they overestimated the damage present after the blast for the LCFRC specimens.

Lastly, the surface damage obtained in the experimental tests and the LS-DYNA finite element models was compared, as illustrated in Figure 1.8.

Through the comparison of the surface damage and weight loss of the specimens, the authors concluded that the LCFRC outperforms the RC in the blast spalling resistance. Additionally, LS-DYNA, with the use of Material Model 159, successfully modelled the response of the LCFRC exposed to blast loadings. This reveals that finite element modelling is an alternative when full-scale blast testing is not feasible.

In the 2015 article of Štoller and Zezulová [51], high strength fibre reinforced

Top surface   Bottom surface

(a) RC panel

Top surface   Bottom surface

(b) LCFRC panel
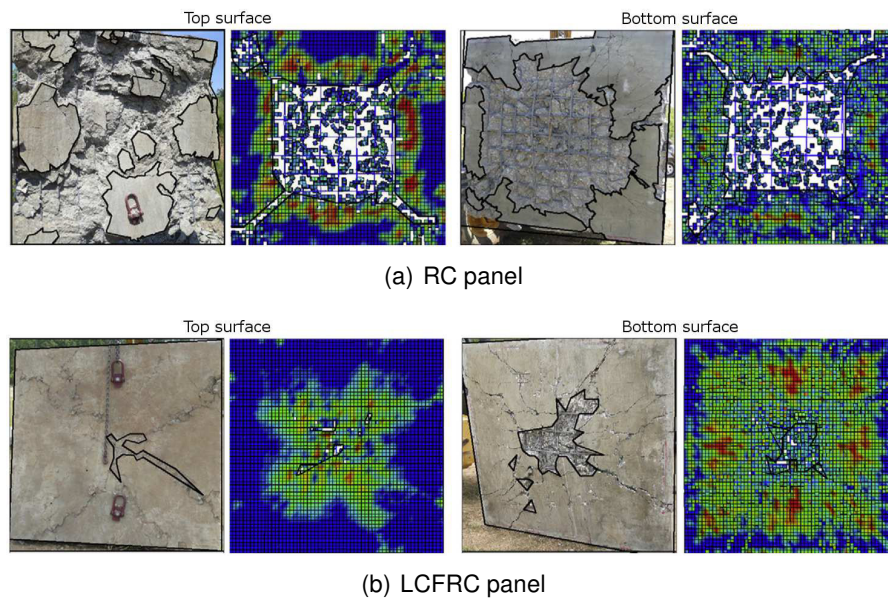
Figure 1.8: Comparison of the surface damage [45]

concrete (HSFRC) slabs were subjected to contact and distant blast loadings. The authors analysed several blast parameters defined in the literature, and verified that the different formulations are very similar, differing only in coefficients, which result in an uncertainty of a range of $\pm$ 20 %. Additionally, the reliability of each formulation increases with the distance to the blast.

Two numerical models, represented in Figure 1.9 after being subjected to blast loadings, were created in the ANSYS-AUTODYN software by the authors to simulate the two experimental tests. For the contact explosion, sandwich slabs with three layers of various width combinations were created, with the outer two layers consisting of HSFRC and an inner layer of polystyrene, and subjected to a blast of 250 g PlNp 10 contact charge. Additionally, for the distant blast loadings, thin and thick slabs were subjected to the blast effects of a TNT charge at different distances.

The results of the experimental and numerical tests are similar, and confirm the ability of the HSFRC to withstand contact and distant explosions. However, the time of analysis for the contact explosion case, with a 1.0 ms duration of simulation and 8.0 million of elements, was 10 days in a workstation HP Z800 (2$\times$6 core XEON and 96 GB of RAM), which might turn infeasible the numerical determination of the problem on a computer with worse characteristics.

The Applied Element Method was used in the Coffield and Adeli's 2014 article to test the effectiveness of different framing systems for three seismically designed steel frame structures subjected to blast loadings [10]. The three framing systems, represented in Figure 1.10, were: a moment resisting frame (MRF), a concentrically braced frame (CBF) and an eccentrically braced frame (EBF). The designs were performed in a previous research resorting to ETABS.
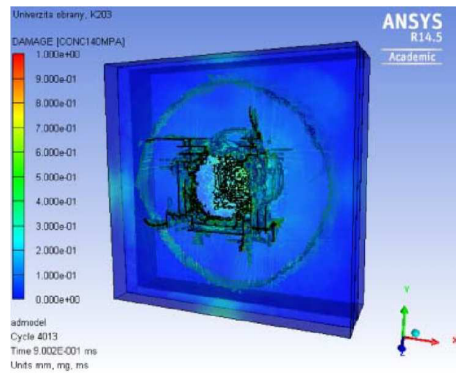
(a) Contact explosion
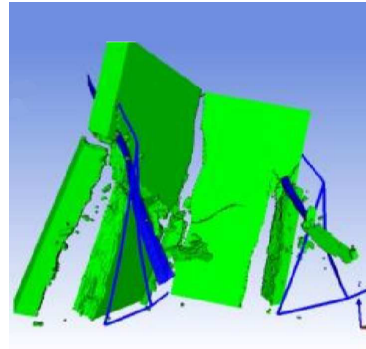
(b) Explosion of 20 kg TNT at a distance of 1.0 m

Figure 1.9: Numerical models created with ANSYS-AUTODYN [51]

(a) MRF

(b) CBF

(c) EBF
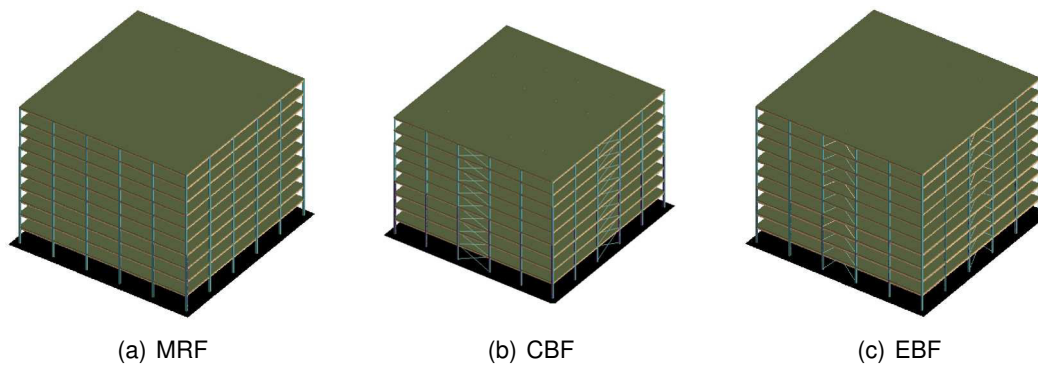
Figure 1.10: Building structures created using Applied Element Method [10]

The structures were modelled with the Applied Element Method and subjected to the loads of an unconfined, free-air burst detonated 4.572 m away from one of the centre columns and 4.6 m above the ground. Three dimensional cuboid elements were used by the authors to create the numerical structures, resulting in approximately in 40000 elements for each model. Approximately 3000 time steps were used for each model, which led to an analysis time of 12-15 hours in a core XEON and 2 GB of RAM.

The effectiveness of the framing systems was obtained through the number of plastic hinges and member failure and the roof's deflections and accelerations due to the blast loads. The main conclusion obtained in this research was that braced frames provide a higher level of resistance to the blast loading scenario.

However, according to the authors, blast analysis of a large 3D multi-storey structure is complicated and requires significant computing resources because a small time step, in the order of 0.0001 seconds, must be used. Hence, several simplifications were considered, such as the non-consideration of the negative and reflected pressures and the strain rate effects.

Asprone *et al* [4] simulated the blast effects on a porous glass fibre reinforced polymer (GFRP) barrier for implementation of this type of structures as a protection system for airport infrastructures. Figure 1.11 represents a prototype of the barrier, which consists of GFRP pipes mounted vertically over a modular reinforced concrete base 0.5 m high, and the Applied Element Method model obtained after a mesh sensitivity analysis.

(a) Prototype (b) Applied Element Method model
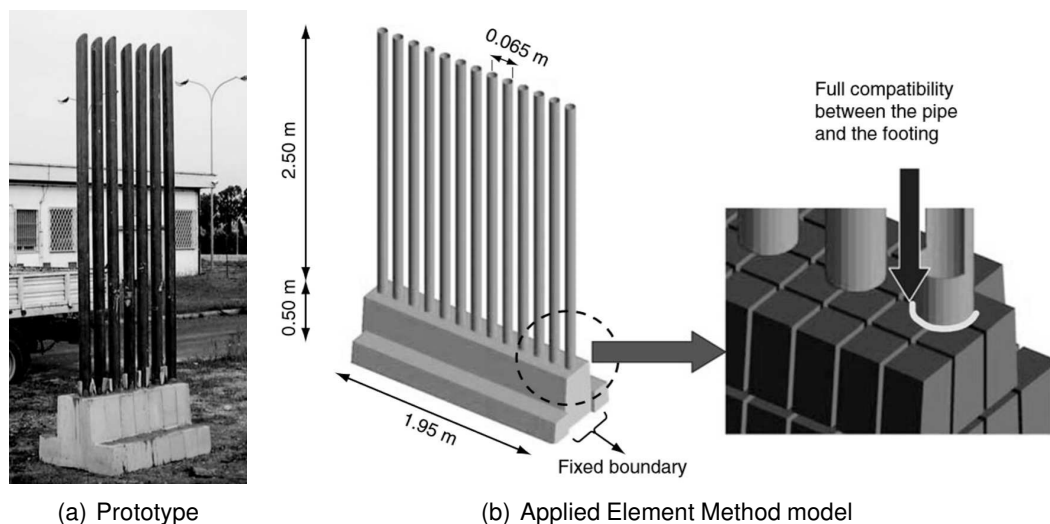
Figure 1.11: GFRP barrier system [4]

In order to ensure a correct simulation, the strain rate effects were taken into consideration for the GFRP. However, due to the dimensions of the concrete footing, these effects were neglected for this material. Afterwards, the authors presented a blast pressure calculation with the following assumptions: only the

drag pressure is applied to the GFRP pipes; the negative phase is negleted; the secondary reflections between the pipes are neglected; there are no fragments due to the blast; the drag pressure decay is similar to the free-air burst pressure decay; a factor of 25 % is added to the calculated pressure to account for any neglected secondary effects.

The assembly of pressure gauges to measure the reflected pressure during the experiments enabled the authors to compare the estimated experimental drag pressure with the drag numerically applied and verify a good agreement between both values which improves with the charge's distance.

Next, the numerical results were compared with the experimental results. Specifically, the wall's deformations and accelerations, the maximum strain contours and the pipes's cracking, separation and failure. From this comparison, the authors concluded that the Applied Element Method model of the barrier correctly predicted the porous GFRP barrier's response to blast loadings, and, thus, can be used in a parametric study to determine the minimum safe stand-off distance, as observed in Figure 1.12.
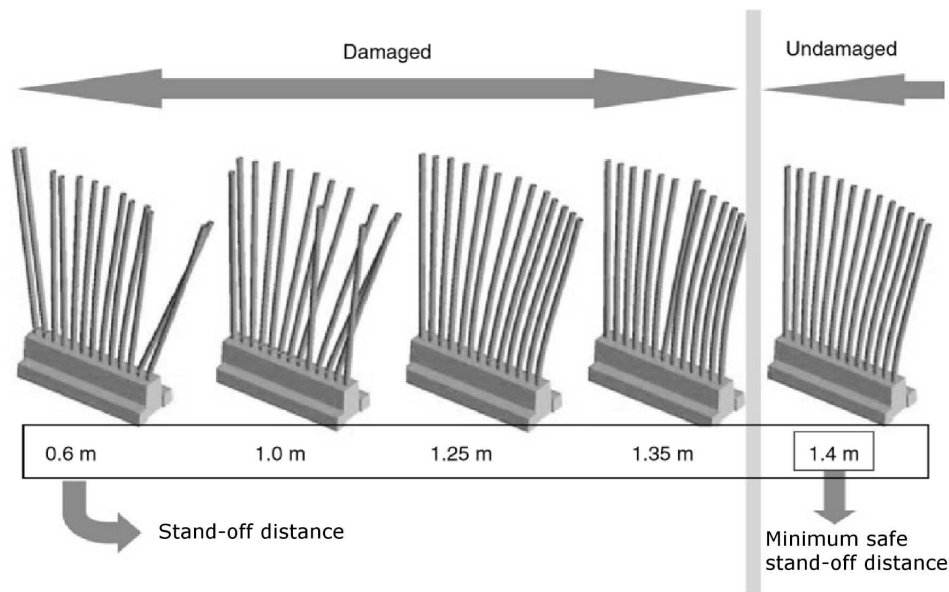
Figure 1.12: Minimum safe stand-off distance (Adapted from [4])

In 2015, Wijesundara and Clubley [52] investigated the effect of time-variant coupled lifted forces and lateral blast pressures on the vulnerability of reinforced concrete columns when subjected to internal explosions. The research resorted to the Applied Element Method together with a high-resolution computational fluid dynamics (CFD) simulations to model the column's response to complex vented and confined internal blast environments.

The numerical verification was performed in two steps: (i) verification of CFD simulations of internal building detonations conducted using the hydrocode 'Air3D',

which represents a robust uncoupled approach, and (ii) verification of the numerical modelling of column's response using the Applied Element Method.

In the first step, Air3D simulations of internal detonations were compared to high-resolution CFD simulations conducted using AUTODYN. The pressure contours, which resulted from AUTODYN simulations, are illustrated in Figure 1.13. Through the comparison of both the overpressure-time and the total impulse-time histories of the two formulations, the authors verified the accuracy and robustness of the Air3D CFD simulation.
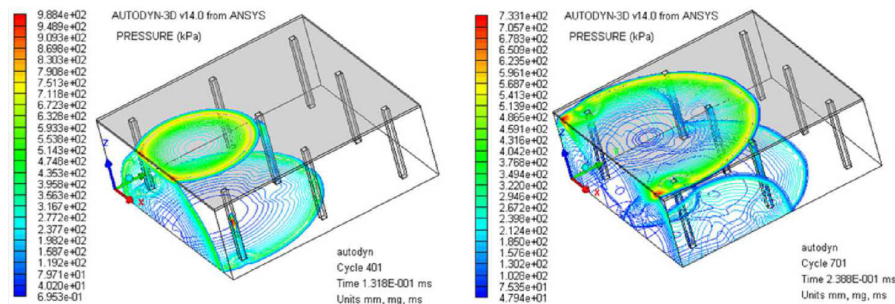
Figure 1.13: Vented blast conditions AUTODYN simulation [52]

In the second step, the accuracy of the numerical modelling of the column's response was verified by comparing the numerical results with experimental test data. Two numerical cases based on the connectivity of the column to the cross girders at the upper end were tested. In Case 1, the upper end's vertical translations during static loading were permitted, whilst both ends were fully fixed in the blast loading case. On the other hand, in Case 2, the columns were modelled together with adjacent cross girders and floor plates at the floor level to accurately simulate the partially fixed boundary. Figure 1.14 demonstrate the capability of the numerical analysis to accurately represent the column's failure mode after blast loads.

The authors verified that the widely used simplified boundary conditions, e.g. fixed-fixed, may lead to underestimations in design parameters depending upon the connectivity of the column and the stiffness of the cross girders. Hence, by modelling the adjacent cross girders and plate floor, a significant enhance in the numerical predictions' accuracy might be verified in some circumstances.

Additionally, the authors concluded that both uplift forces and extended lateral pressures, resulting from confined detonations, significantly deteriorate the overall strength and stiffness of RC columns, leading to a high probability of concrete columns to exhibit an unexpected and premature failure due to significant uplift forces, which results from inadequate anchorage of longitudinal reinforcement bars and from conventional design practice for RC columns that only considers axial compression forces. Therefore, the authors recommend the anchorage and continuity of longitudinal reinforcement bars throughout the column's height.
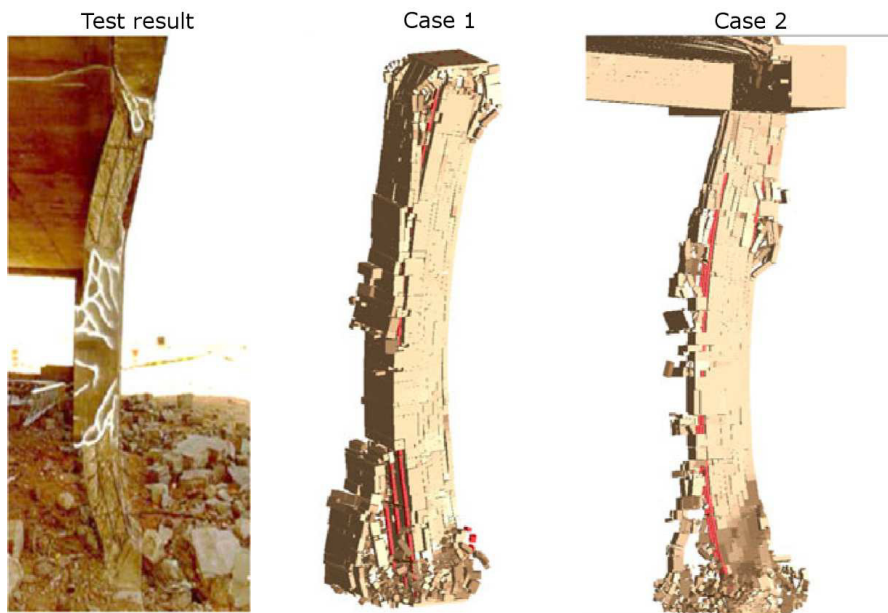
Figure 1.14: Overall failure mode of the column [52]

Chapter 2

Blast Loads

The present chapter reviews the main effects of an explosion, namely, its blast overpressures and the shock loads produced by the blast wave. A set of parameters are used in the literature to characterize the shock waves. However, as alternative formulations can be used to estimate their values, a survey of the existing formulations and a comparison between the values of the corresponding parameters is presented in the present chapter.

2.1 Blast phenomena

According to [34], *"a blast is a pressure disturbance caused by the sudden release of energy"*. The blast waves are often the result of chemical reactions that can be divided into two primary groups: deflagrations and detonations. The former are the result of an oxidation reaction that propagates throughout the unreacted material at a rate lower than the speed of sound, while, on the other hand, in the latter, the reaction front propagates supersonically, resulting in a shock wave.

2.1.1 Scaling method

In order to compare blast wave parameters resulting from different explosions, one must use a scaling method. The most commonly used method is the Hopkinson-Cranz, or cube root, scaling method [34]. This method defines the scaled distance as:

$$Z = \frac{R}{W^{1/3}} \tag{2.1}$$

where R is the distance from the burst's origin (expressed in m) and W is the explosive's mass (expressed in kg). The use of equation (2.1) allows the study and the comparison of blast waves resulting from different weight charges and distances.

2.1.2   Shock wave phenomena

As a result of the detonation, a pressure front propagates radially throughout the atmosphere as a shock wave. At any given point away from the burst's origin, the arriving time of the wave to the structure is defined by t_A. At that moment, the wave is mainly characterized by an almost instantaneous rise in pressure, from ambient pressure, P_a, to a peak incident pressure, P_{so}, followed by a decay back to the ambient pressure in a time interval t_o. This positive phase is followed by a negative phase, characterized by a reverse air flow, that has a minimum pressure value of P_{so}^- and a duration of t_o^-, usually much longer than the duration of the positive phase. However, in most blast studies, the negative phase of the shock wave is ignored because it is usually weaker and more gradual than the positive phase, resulting in a less significant structural response. The previously described behaviour can be observed in Figure 2.1.
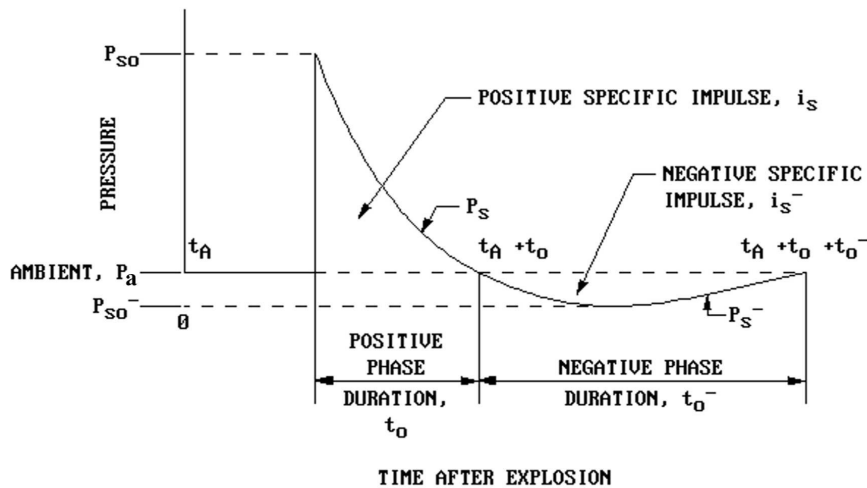
Figure 2.1: Pressure-Time variation (Adapted from [13])

On the other hand the pressure-time correlation may be expressed by the modified Friedlander's equation, presented in Baker [5]:

$$P(t) = P_{so} \left(1 - \frac{t}{t_o} \right) e^{\frac{-bt}{t_o}} \tag{2.2}$$

where b is a decay constant, as defined in Figure 2.2.

In order to define the shock wave's behaviour, three characteristics are necessary. Firstly, one must define the peak overpressure, P_{so}, and the positive phase's duration t_o. At last, one needs to obtain the specific impulse, which can be achieved through the integration of the area under the pressure-time curve represented in Figure 2.1, as i_s and i_s^- for the positive and negative phase, respectively. The resulting expressions, obtained using equation (2.2) for the pressure-time relation, are given by:
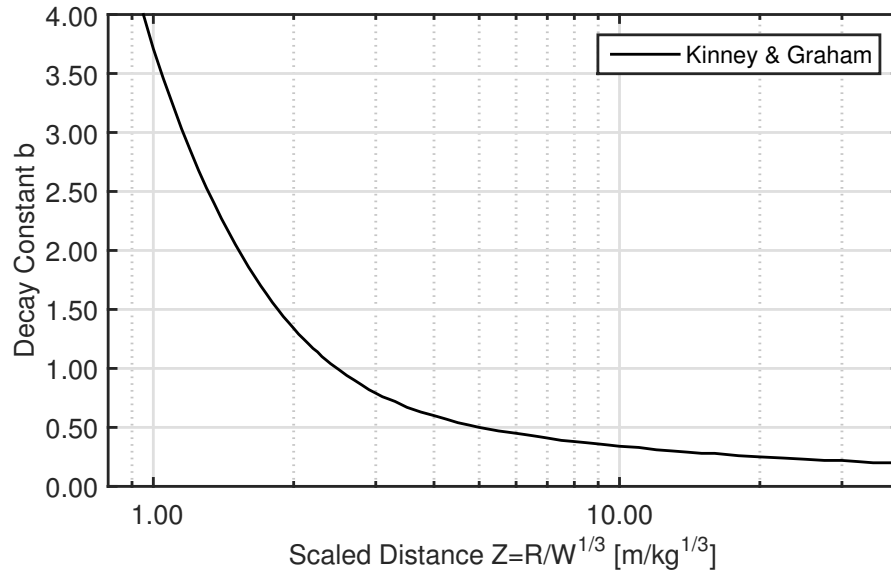
Figure 2.2: Decay constant [23]

$$i_s = \int_0^{t_o} P(t)\,\mathrm{d}t = \frac{P_{so}t_o}{b}\left[1 - \frac{\left(1 - e^{-b}\right)}{b}\right] \tag{2.3}$$

$$i_s^- = \int_{t_o}^{\infty} P(t)\,\mathrm{d}t = -\frac{P_{so}t_o}{b^2}\,e^{-b} \tag{2.4}$$

for the positive and negative phase, respectively.

Peak overpressure

Both experimental and theoretical means have been used in the literature to obtain the relevant characteristics of blast waves. With the development of the computer technology, numerical solutions have been obtained and afterwards validated by experimental tests. In 1965, an experimental approximation for the peak overpressure was suggested in the US Army Technical Manual [12], with Z expressed in imperial units (ft/lb$^{1/3}$), as:

$$P_{so} = \frac{4120}{Z^3} - \frac{105}{Z^2} + \frac{39.5}{Z} \tag{2.5}$$

However, the use of this expression is very limited, as it should only be applied when 160 psi $> P_{so} > 2$ psi and 20 ft/lb$^{1/3}$ $> R/W^{1/3} > 3$ ft/lb$^{1/3}$. Due to this limitation, the present norm [13] establishes an empirical relation, illustrated in Figure 2.3, defined for 100 ft/lb$^{1/3}$ $> R/W^{1/3} > 0.132$ ft/lb$^{1/3}$.

Additionally, Kinney and Graham [23] defined the overpressure as a function of Z, expressed in international units, as seen in equation (2.6).

$$\frac{P_{so}}{P_a} = \frac{808 \left[1 + \left(\frac{Z}{4.5}\right)^2\right]}{\sqrt{1 + \left(\frac{Z}{0.048}\right)^2} \sqrt{1 + \left(\frac{Z}{0.32}\right)^2} \sqrt{1 + \left(\frac{Z}{1.35}\right)^2}} \tag{2.6}$$

The previously defined peak overpressure formulations are graphically represented in Figure 2.3 as a function of Z, expressed in international units. Through the analysis of Figure 2.3, one can observe that all the formulations result in very similar overpressure ratios. Because the TM5-855-1 expression is only valid on a smaller domain, it will not be addressed again in this dissertation.
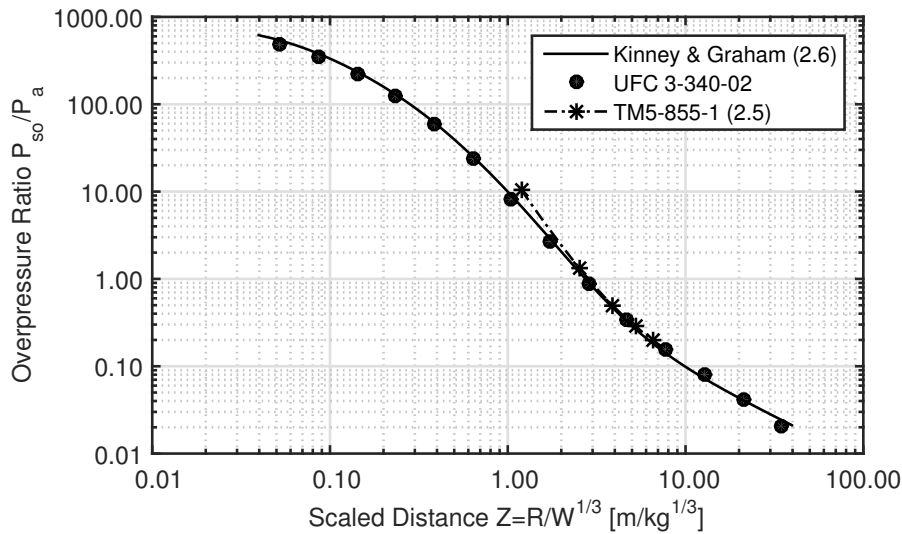
Figure 2.3: Peak overpressure [12, 13, 23]

Positive phase duration

Taking into account that the damage inflicted on the structure depends on how long the blast loads are applied for, the positive phase duration is one very important characteristic of the shock wave [23].

This parameter, t_o, is a function of P_{so} and the total energy yield of the explosion. At the end of the positive phase, a zero overpressure value is obtained, which is a characteristic of a sound wave that has no shock front and infinitesimal changes in pressure amplitude. The zero overpressure moves away from the origin of the explosion at the speed of sound in air. However, because the shock wave front velocity, in high explosions, is higher than the speed of sound, one can conclude that the distance between these two points increases with the distance to the centre of the explosion, leading to an increasing duration of the positive phase with this distance and reaching a limiting value when $P_{so} = 0$ [7]. Typical values of t_o for detonations might be obtained through the equation (2.7) presented by Kinney and Graham [23],

$$\frac{t_o}{W^{1/3}} = \frac{980 \left[1 + \left(\frac{Z}{0.54}\right)^{10}\right]}{\left[1 + \left(\frac{Z}{0.02}\right)^3\right] \left[1 + \left(\frac{Z}{0.74}\right)^6\right] \sqrt{1 + \left(\frac{Z}{6.9}\right)^2}} \tag{2.7}$$

as a function of Z expressed in international units and scaled for a one kilogram TNT explosion. Alternatively, its value could be estimated from the empirical relation presented in the UFC [13] and illustrated in Figure 2.4. Through the analysis of Figure 2.4, one can observe that the two formulations result in different positive phase durations, probably due to the difficulty of experimental measurement of the reviewed characteristic.
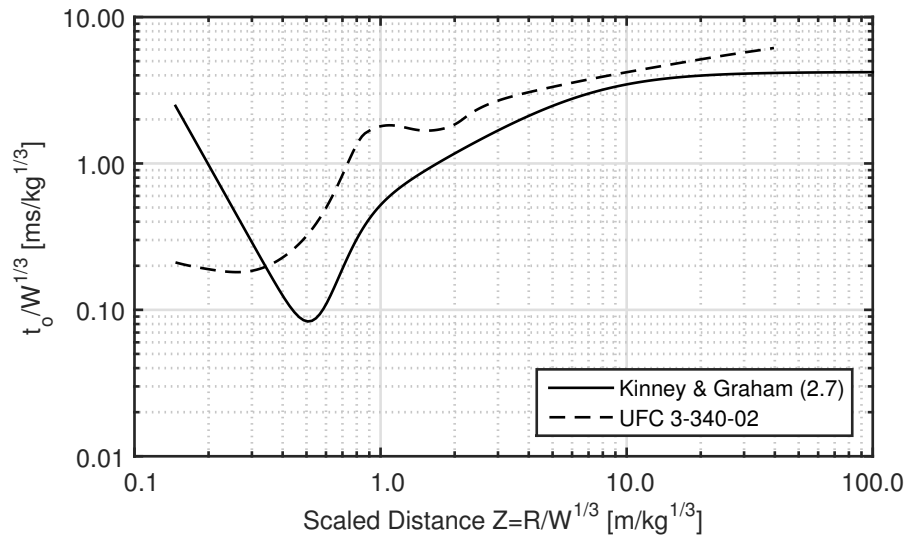
Figure 2.4: Positive phase duration [13, 23]

Shock wave impulse

The knowledge of the peak overpressure and the duration of the positive phase allows the calculation of the shock wave impulse, which can be graphically represented as the area under the pressure-time curve. Admitting that the significant part of an explosion is associated with the positive phase, one can consider the positive impulse per area unit as a characteristic for the entire shock wave system. An empirical equation presented in [23] is given in equation (2.8) as a function of Z, with the scaled distance expressed in meters per cubit root kilogram of TNT and represented in Figure 2.5.

$$i_s = \frac{0.0067 \sqrt{1 + \left(\frac{Z}{0.23}\right)^4}}{Z^2 \sqrt[3]{1 + \left(\frac{Z}{1.55}\right)^3}} \tag{2.8}$$

where i_s is expressed in MPa.ms. Alternatively, the Unified Facilities Criteria (UFC) [13] defines the shock wave impulse per cubic root of explosive mass. In Figure 2.5 the previous definition is illustrated for a one and a five kilogram TNT explosion.
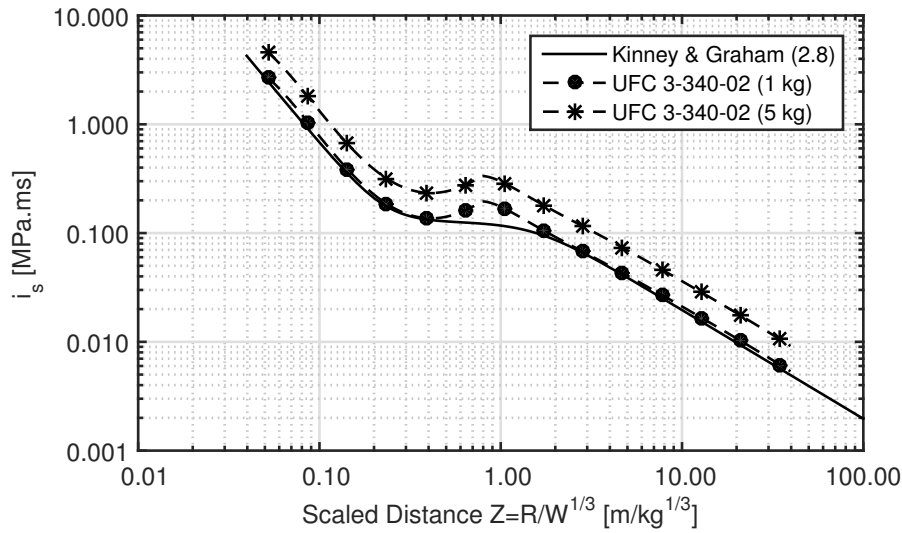
Figure 2.5: Shock wave impulse [13, 23]

The empirical definition of the UFC resulted in a shock wave impulse, which is scaled for a one kilogram TNT explosion. However, as the Kinney and Graham's definition is not scaled, larger differences between the two formulations are observed as the explosive mass increases.

2.1.3 Dynamic pressure

After the shock front passage, the resulting air flow generates a dynamic pressure. This effect is cumulative to the blast overpressure and is a function of the peak incident pressure resulting from the free-air burst[1] and the shape of eventual obstructions. For low overpressure range and atmospheric sea level conditions, one can use Newmark's equation [34], with P_{so} expressed in psi.

$$q_s = 0.022 \left(P_{so}\right)^2 \tag{2.9}$$

Alternatively, one can use the Rankine-Hugoniot relation [35], where P_a is the atmospheric pressure at sea level expressed in MPa.

$$q_s = \frac{5}{2} \frac{P_{so}^2}{\left(7P_a + P_{so}\right)} \tag{2.10}$$

Both of the above relations are depicted in Figure 2.6, together with the estimate for the dynamic pressure defined in the UFC [13].

From the observation of Figure 2.6, one can conclude that the relations defined by Rankine-Hugoniot and the UFC are very similar, i.e. they conduct to similar values of q_s. However, Newmark's relation leads to different values as the peak incident pressure increases, which might be due to the simplicity of the relation.

---

[1]Free-air burst is an explosion where no amplification of the shock wave occurs from its origin to the structure.
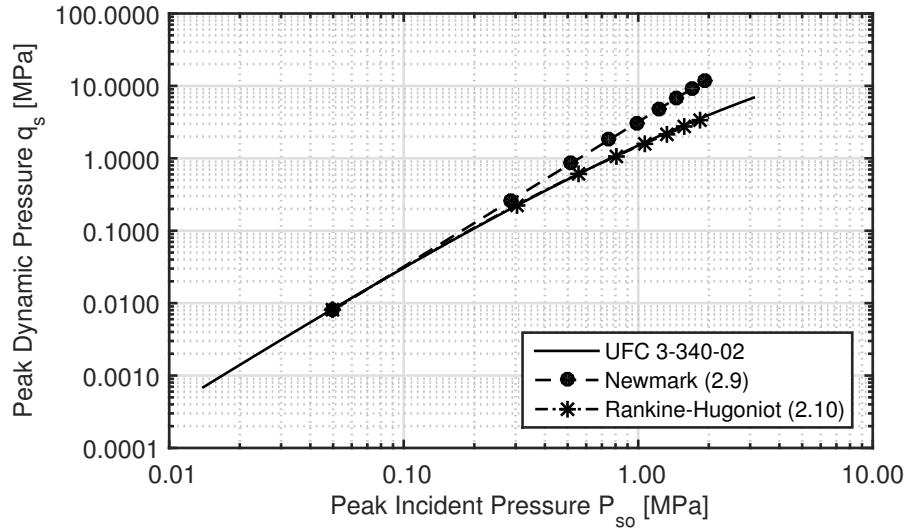
Figure 2.6: Peak dynamic pressure [13, 34, 35]

2.1.4 Shock front velocity

The shock front velocity U, allows us to compute several parameters, such as the arrival time of the sock front to the structure and the wave length. As presented before, the shock front velocity in detonations is higher than the speed of sound. According to [35], one can use the Rankine-Hugoniot relation to determine the shock wave velocity as follows:

$$U = C_0 \sqrt{1 + \frac{(\gamma + 1) P_{so}}{2\gamma P_a}} \tag{2.11}$$

where C_0 is the speed of sound in air (340.29 m/s). If one considers an ideal gas, with a ratio of specific heats[2] $\gamma = 1.4$, equation (2.11) reads:

$$U = 340.29 \sqrt{1 + \frac{6P_{so}}{7P_a}} \tag{2.12}$$

Alternatively the UFC [13] presents an abacus for the shock wave velocity as a function of the peak incident pressure. Comparing the two formulations, represented in Figure 2.7, one can observe that they yield similar results.

2.1.5 Wave length

The positive phase wave length L_w, corresponds to the length of the region in which positive overpressures are being experienced at a given time t. According to [24], its value can be obtained as,

$$L_w = U t_o \tag{2.13}$$

---

[2]Ratio of specific heats can be defined as the ratio of the specific heat at constant pressure to the specific heat at constant volume.
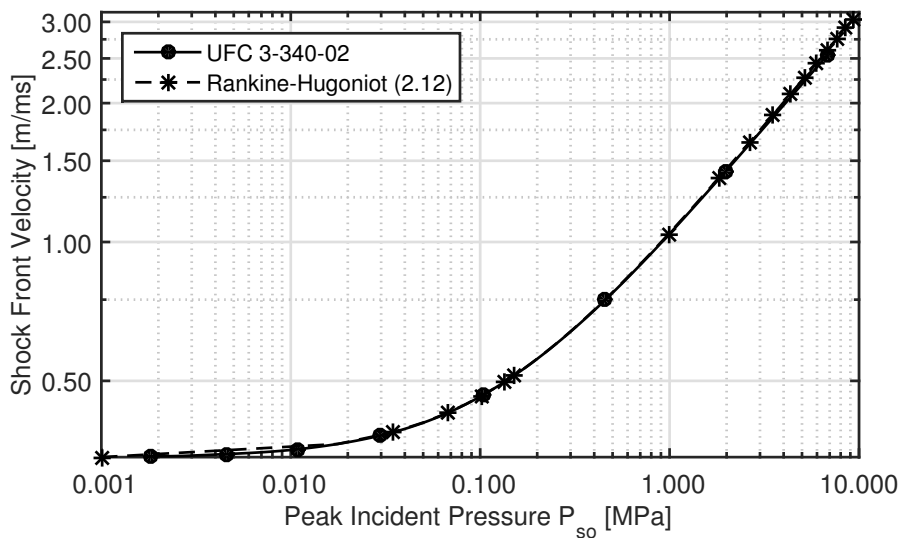
Figure 2.7: Shock front velocity [13]

where U is the shock front velocity and t_o is the duration of the positive phase expressed in m/ms and ms, respectively.

2.2   Blast loading categories

According to [13], blast loadings can be separated into two main groups, confined and unconfined explosions, as well as in several categories, as seen in Table 2.1.

Table 2.1: Blast load categories [13]

Charge Confinement	Categories
Unconfined	Free-air burst (No. 1)
	Air burst (No. 2)
	Ground burst (No. 3)
Confined	Fully vented (No. 4)
	Partially confined (No. 5)
	Fully confined (No. 6)

The blast's locations corresponding to the classification of the unconfined explosions presented in Table 2.1 are illustrated in Figure 2.8. On the other hand, a schematic illustration of the confined explosions is presented in Figure 2.9.

To be considered a free-air burst, the resulting shock wave must suffer no amplification from its origin to the structure. This is the case of location No. 1. On the other hand, for explosions occurring at locations No. 2 and No. 3, the shock wave suffers an amplification due to the proximity to the ground. More specifically, for location No. 3, the explosion occurs so close to the ground that the sock wave is amplified at the detonation point.
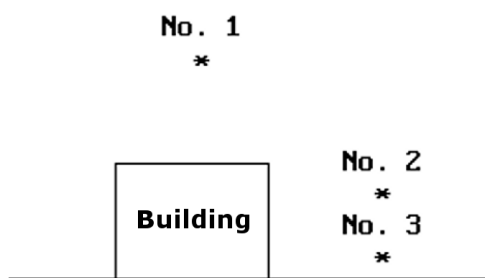
Figure 2.8: Blast load unconfined categories [13]

Fully vented   Partially vented   Fully confined
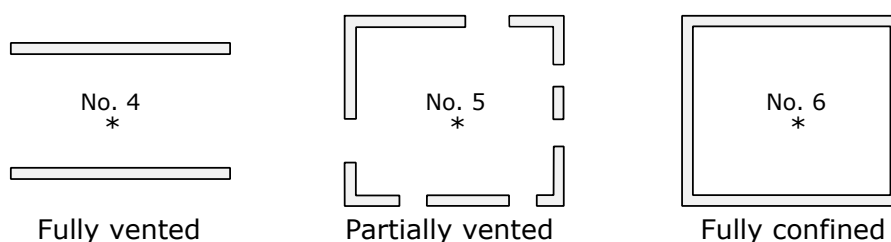
Figure 2.9: Blast load confined categories (Adapted from [53])

In what concerns confined explosions, one can see that an explosion on location No. 4 occurs within a barrier or cubicle type structure with one or more surfaces open to the atmosphere. In this case, the initial wave is amplified by the non-frangible[3] portions of the structure and the products of detonation are, immediately, fully vented to the atmosphere, forming a shock wave.

This total ventilation does not occur in location No. 5, which takes place in structures with limited size openings and/or frangible surfaces. In these situations, the initial wave is amplified and the products of detonation are ventilated to the atmosphere after a finite period of time. Lastly, No. 6 locations are associated with total or near total containment of the explosion. This conditions generate unventilated shock loads and a very long duration of gas pressures, depending upon the containment degree.

Since the main focus of this dissertation are unconfined explosions, they will be presented in more detail over the next sections.

2.2.1 Free-air burst

A free-air burst is an explosion in which the shock wave suffers no amplification or reflection from its origin to the structure, as seen in Figure 2.10, where a free-air burst resulting from W kg of TNT is represented.
Until the wave impacts a structure or the ground, it behaves as presented in Section 2.1.2. When the impact happens, the shock wave suffers a reflection and an amplification. In what follows, and according to the current practice in the

---

[3]The Oxford Dictionary defines *frangible* as: *"Able to be broken into fragments, brittle or fragile."*
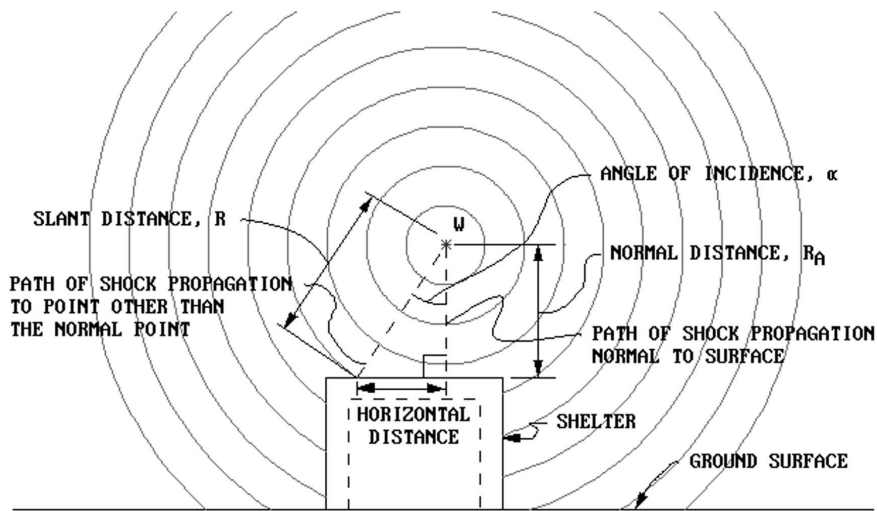
Figure 2.10: Free-air burst [13]

literature in order to define overpressures it is assumed that the structure and/or the ground surfaces are rigid, in other words, there is no energy dissipation resulting from surface deformation. However, in some cases, this assumption might lead to some discrepancy between experimental results and analytical estimations.

Normal Reflection

A normal reflection is verified whenever the shock wave strikes perpendicular to a surface. This happens when the line that describes the path of the travelling wave, with a length of R_A, is normal to the surface, as represented in Figure 2.10. At the moment of impact, the wave's direction changes abruptly and, as a consequence, the air particles at the surface acquire a relative velocity compared to those further from the surface. This has an effect on the new shock wave moving back through the air, which is an increase in its overpressure to P_r. In Figure 2.11 one can observe the increment in overpressure due to the reflection which will result in a superior impulse. Additionally, one can observe that the phase durations remains unchanged.

To estimate the normal peak reflected overpressure, first, one must define the magnitude of the dynamic pressure with the Rankine-Hugoniot relation [35] as:

$$q_s = \frac{P_{so}^2}{2\gamma P_a + (\gamma - 1)P_{so}} \tag{2.14}$$

where γ is the ratio of the specific heat at constant pressure to the specific heat at constant volume, ratio of specific heats, and P_a is the atmospheric pressure.

When the shock wave hits a solid surface and the path of travel is normal to it, the peak reflected overpressure can be represented through the expression presented in [35]:

$$P_r = 2P_{so} + (\gamma + 1)q_s \tag{2.15}$$
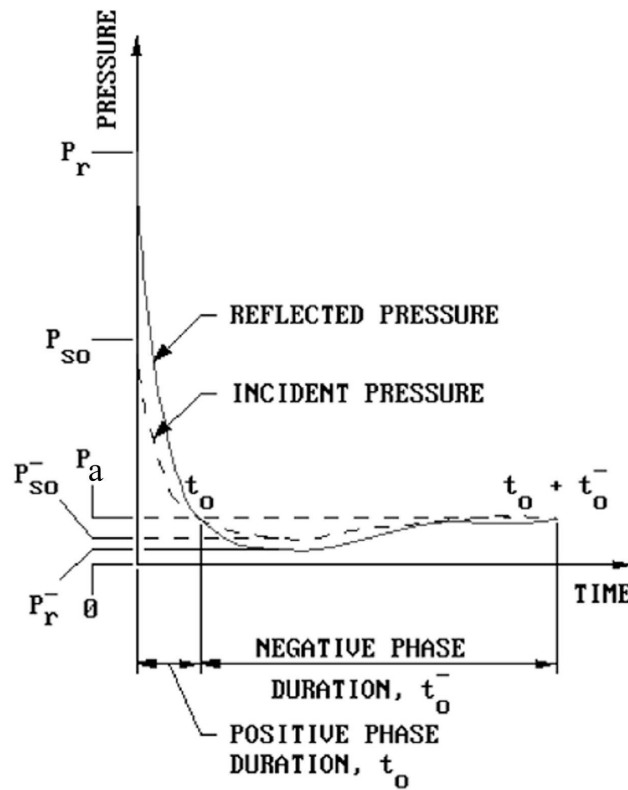
Figure 2.11: Pressure-Time variation for Free-air burst [13]

The assumption that air is an ideal gas with $\gamma = 1.4$ usually yields a very good approximation for current situations. With this in mind, Rankine-Hugoniot simplified the former expressions, considering $\gamma = 1.4$, to the expression depicted in equation (2.16). However, if the peak incident overpressure exceeds 2 MPa, the value of the ratio of the specific heats γ begins to decrease from the assumed value.

$$P_r = 2P_{so} \left(\frac{7P_a + 4P_{so}}{7P_a + P_{so}} \right) \qquad (2.16)$$

Alternatively [34], one can determine the peak reflected overpressure, expressed in psi, using Newmark's equation for peak incident overpressures lower than 40 psi (0.27 MPa) and for sea level atmospheric pressures:

$$P_r = (2 + 0.05 P_{so}) \, P_{so} \qquad (2.17)$$

Finally, the UFC [13] empirically defines the reflected overpressure ratio. These values are presented in Figure 2.12 together with the previous formulations, in order to allow a better comparison between them.

Analysing the graphs in Figure 2.12, one can readily observe the strong dependence of the reflected overpressure ratio on γ for a peak incident pressure
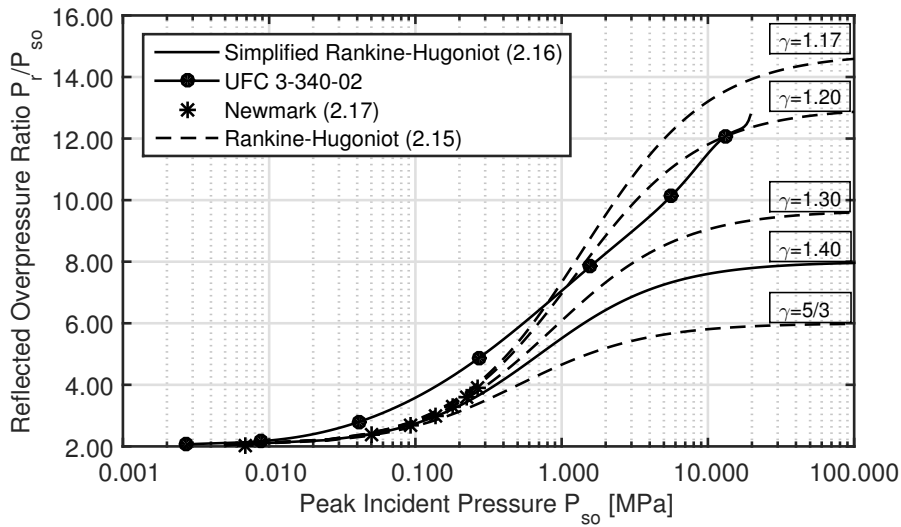
Figure 2.12: Reflected overpressure ratio [13, 34, 35]

higher than 0.3 MPa. For lower values of the peak incident pressure, all formulations lead to similar results. One should note that the UFC [13] relations seem to take into account the variation of γ for all values of peak incident pressure, which could be explained by the empirical origin of the formulation, based on experimental tests.

The UFC [13] also defines the scaled reflected impulse for normal reflections through an abacus, which can be visualized in Figure 2.13.
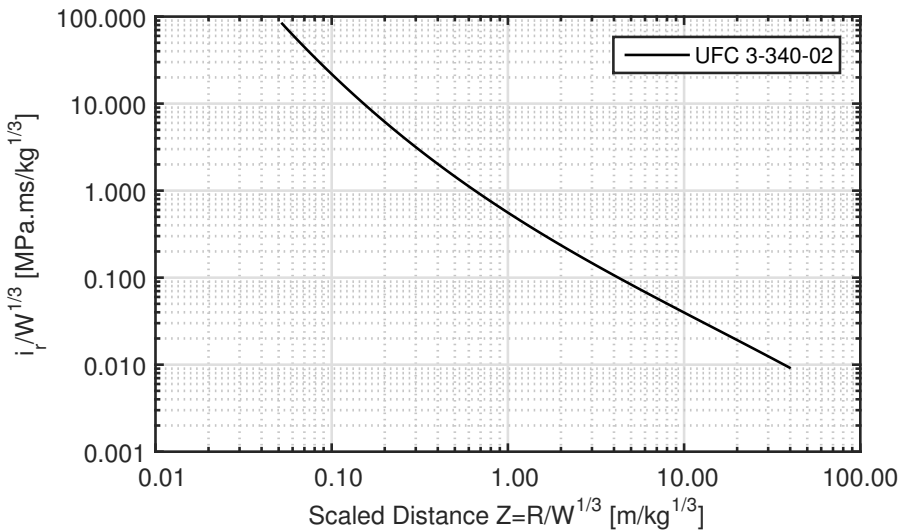
Figure 2.13: Reflected scaled impulse for normal reflections [13]

Note that equations (2.16) and (2.17) define only the reflected peak overpressure and therefore, the time history for the reflected pressure is not defined. One can roughly estimate the reflected specific impulse if the incident impulse is known or

predictable, by assuming similarity between the time histories of both the incident and the reflected overpressures [5]. This assumption gives:

$$\frac{i_r}{i_s} \approx \frac{P_r}{P_{so}} \tag{2.18}$$

Oblique reflection

An oblique reflection occurs when the shock front impacts a surface close to the normal path of travel. This phenomenon is very similar to the reflection of sound waves. However, for shock waves, the angle of reflection is not ordinarily equal to the angle of incidence. According to Baker [5], oblique reflections can be classified as either regular or Mach reflections, depending upon the incident angle and shock strength. The following review concerns only the regular reflections' behaviour because only these are of interest for free-air bursts. As observed on Figure 2.14, the incident shock travels through still air (Region 1) at velocity 1, impacting the surface with an angle α_i. In Region 2, which is situated behind this front, properties correspond to the ones found in the region behind the shock front of a free-air burst. On the contact with the surface, the flow behind the incident shock is turned and the shock is reflected from the surface at a reflection angle α_r. Hence, the conditions in Region 3 are the reflected shock properties.
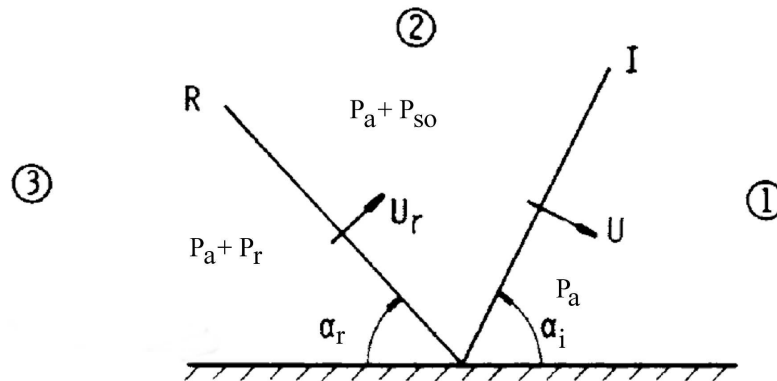
Figure 2.14: Regular oblique reflection of a shock from plane surface (Adapted from [22])

In 1946, Kennedy [22] defined the following properties for the previously defined reflection:

- For a given strength of incident shock, there is a critical angle of incidence $\alpha_{i\ crit}$, such that the type of reflection described above cannot occur for $\alpha_i > \alpha_{i\ crit}$;

- For each gaseous medium, there is an angle α' such that for $\alpha_i > \alpha'$, the strength of the reflected shock is greater than it is for a normal reflection. For air (approximated as an ideal gas with $\gamma = 1.40$), $\alpha' = 39.38°$;

- For a given strength of incident shock, there is a value for $\alpha_i > \alpha_{min}$ such that the strength of the reflected shock, P_r/P_a is minimum;

- The angle of reflection α_r is an increasing monotonic function of the angle of incidence α_i.

It is possible to obtain the reflected peak overpressure for an oblique reflection through the following expression:

$$P_r = C_r P_{so} \tag{2.19}$$

where C_r is the reflected overpressure ratio (dimensionless), which can be determined from the abacus present in Kinney and Graham [23], Figure 2.15, or alternatively using the abacus shown in the UFC 3-340-02 [13], Figure 2.16. In a similar way, it is possible to observe the abacus that defines the reflected scaled impulse as a function of the incidence angle, found in the UFC, in Figure 2.17.
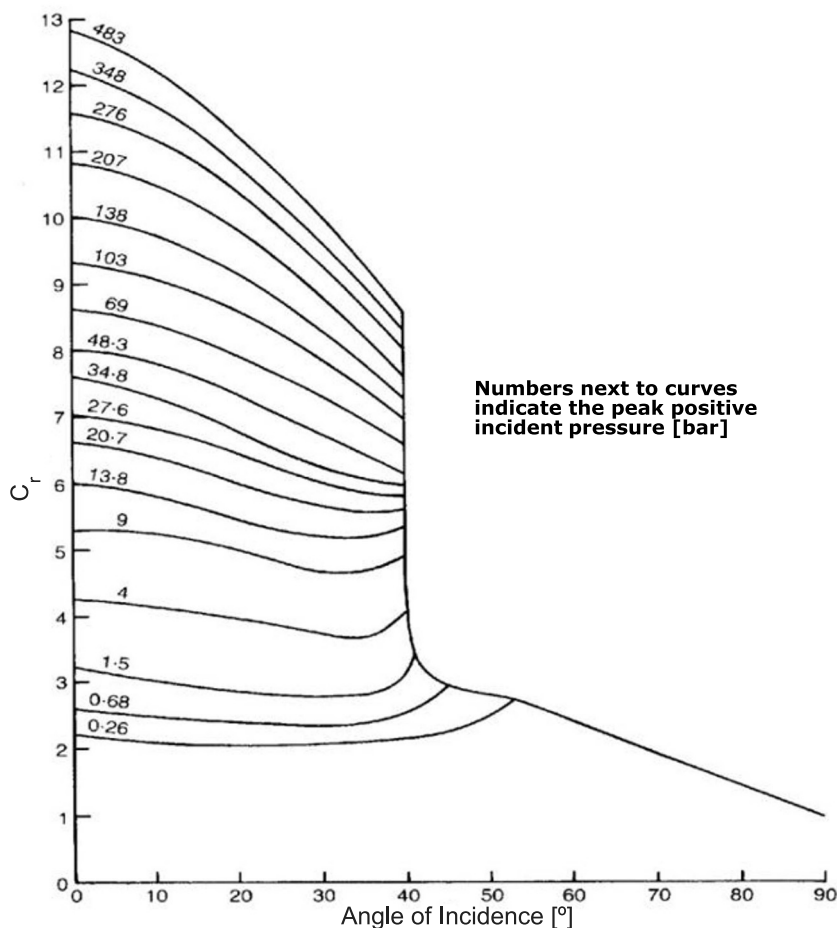
Figure 2.15: Reflected overpressure ratio (Kinney and Graham) [23]

Although the reflected overpressure ratio values in the UFC are defined for angles of incidence up to 90°, one must take into account that for oblique reflections only angles of incidence up to 40° are allowed for high peak incident pressures and up to 55° for lower peak incident pressures [7].
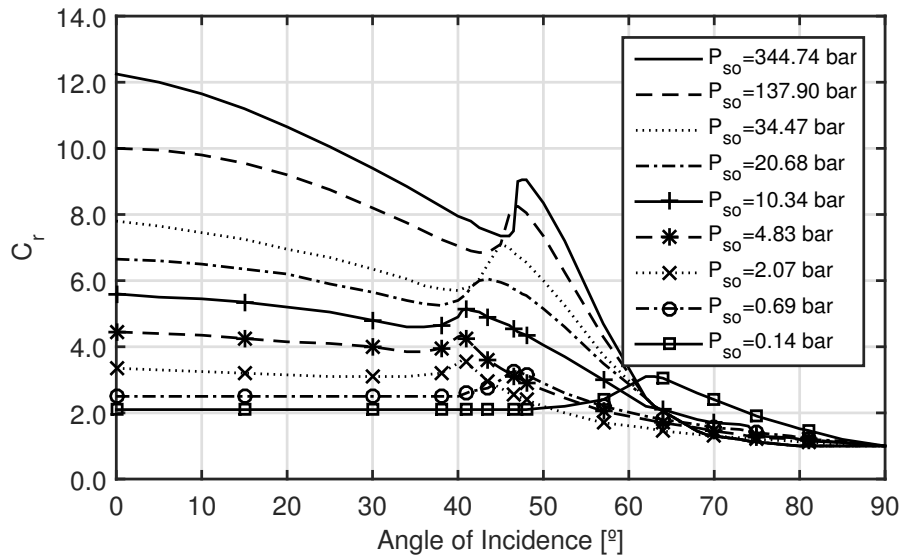
Figure 2.16: Reflected overpressure ratio (UFC 3-340-02) [13]
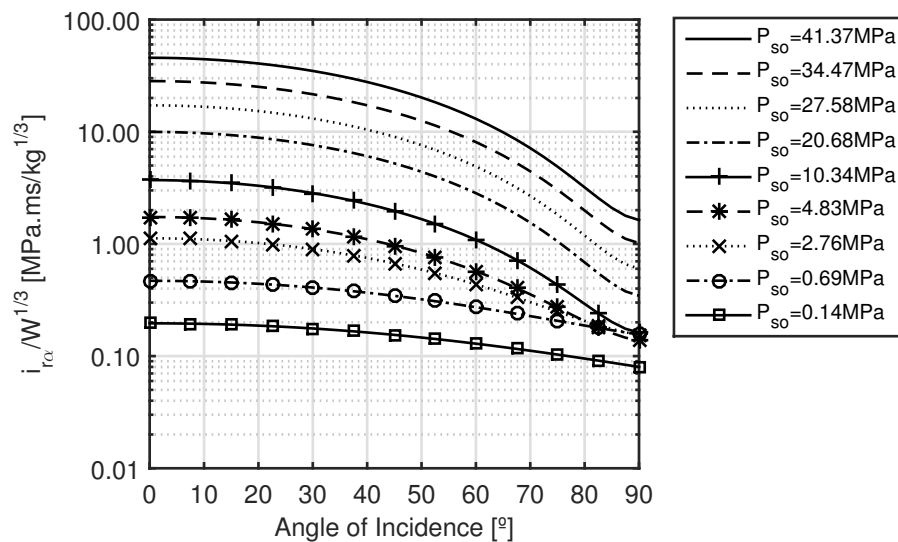
Figure 2.17: Reflected scaled impulse [13]

2.2.2 Air burst

The shock wave in an air burst suffers ground reflections before the impact with the structure, resulting in an amplification of its properties. The UFC defines the air burst as an explosion which occurs two to three times the height of a one or two-story building.

At the moment of impact with the ground, the incident shock wave is reflected. The resulting reflected wave travels at a higher velocity than the incident wave. This results in the overtaking of the incident wave by the reflected wave creating what is known as a Mach stem or a Mach front, since it was first analysed by Mach and

Sommer [7]. To simplify the problem, it is assumed that the Mach front is a plane wave with a uniform pressure and a magnitude similar to the incident pressure. This phenomenon can be observed in Figure 2.18 and occurs when the incident angle exceeds the critical angle of incidence $\alpha_{i\ crit} \approx 40°$.
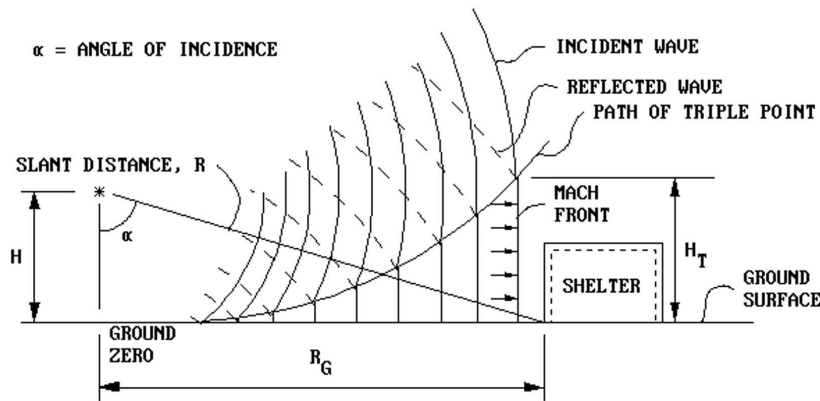
Figure 2.18: Air burst environment [13]

The point at which the incident and reflected waves intersect the Mack stem is referred to as triple point. In Figure 2.18 it is possible to observe the path of this point, whose altitude increases as the wave travels throughout the atmosphere. This altitude, H_t in Figure 2.18, is extremely important in structural design because it determines the structure's loading. If the triple point's height is larger than the structure's height, the structure is loaded by a uniform pressure distribution. However, if the triple point's height is lower than the structure's height, one must adjust the pressure accordingly.

Using the abacus presented in Figure 2.19, one can estimate the triple point's height as a function of the scaled charge height and the scaled horizontal distance.

Due to the complexity of calculation of the reflected peak overpressure present on an air burst's environment, illustrated in Figure 2.18, the description of the process is presented next:

- Determine the slant distance R;

- Compute the blast parameters for a free-air burst as reviewed in Section 2.1.2;

- Estimate P_r as a function of the incident angle and the peak incident pressure (Figure 2.16).

2.2.3   Ground burst

At last, a ground burst is an explosion that occurs close to, or on the ground, which results in a shock wave amplified at the detonation point by the ground reflections,
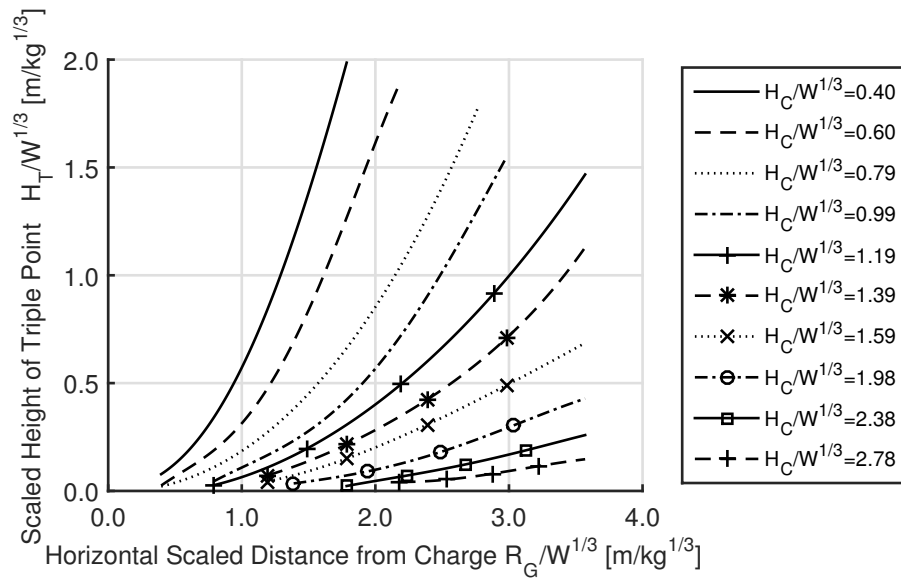
Figure 2.19: Scaled height of triple point [13]

as illustrated in Figure 2.20.
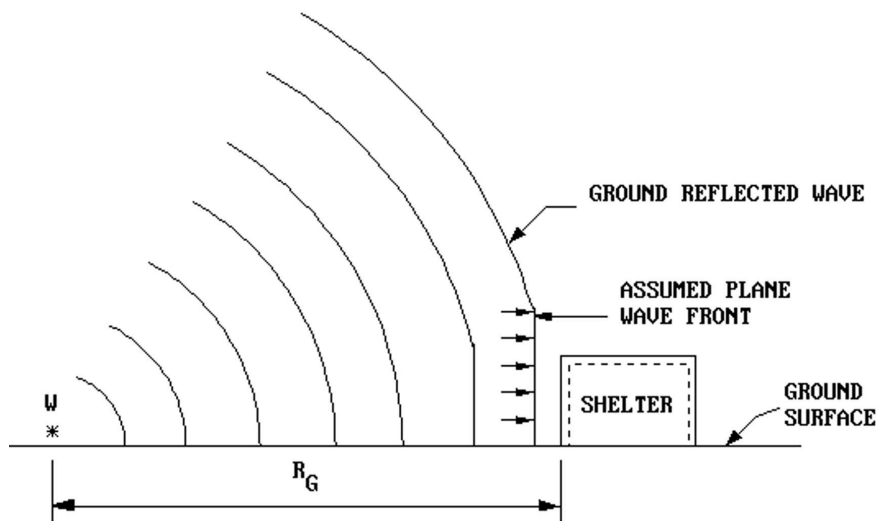
Figure 2.20: Ground burst environment [13]

Considering the soil as a perfectly smooth, rigid plane, once a ground burst takes place, the resulting shock front would be hemispherical. Therefore, the energy of the explosion would be concentrated in a smaller surface area (half of a free-air burst's surface area) and the relations presented in Section 2.1.2 become valid if $2W$ is used instead of W. However, if one considers the energy dissipated by cratering and ground shock, the factor of 2 must be reduced. Accordingly, Bulson [7] suggests that the factor should be generically reduced to 1.7, while, alternatively, Baker [5] proposes a value of 1.8. Note that both factors were

obtained through empirical observation, and hence, depending upon the ground surface's characteristics, might become invalid. The scaled distance may thus be expressed by:

$$Z = \frac{R}{(1.7W)^{\frac{1}{3}}} \qquad \text{or} \qquad Z = \frac{R}{(1.8W)^{\frac{1}{3}}} \tag{2.20}$$

As seen in Section 2.1.2, the UFC usually defines the shock wave parameters through an empirical abacus. In Figure 2.21 one can observe the abacus presented in the UFC for surfaces bursts.
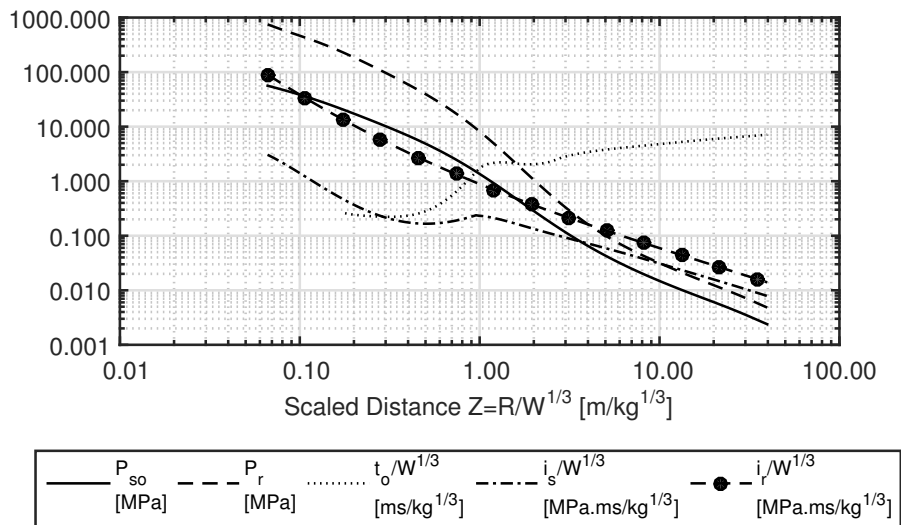
Figure 2.21: Ground burst environment parameters (Adapted from [13])

2.3 External blast loads on structures

In the previous sections, blast phenomena and the characteristics of blast waves according to their classification were reviewed. In this section, methods for determining the blast loads on structures are discussed, with emphasis on a simple approximate procedure that is present in the UFC, and therefore widely applied in practical blast-resistant design.

The dynamic loads resulting from explosions are due to the instantaneous rise in the air pressure caused by the passage of the shock front and to the transient forces associated with the blast winds that follow it [7]. According to the UFC, the blast loading on structures is dependent upon several factors:

- The magnitude of the explosion;

- The location of the explosion relatively to the structure in question;

- The geometrical configuration and stiffness of the structure;

- The structure's orientation with respect to the explosion and ground surface.

The first two points on the list were reviewed in the previous section and will not be discussed further. The geometry of the structure will influence how the blast wave interacts with it. On the other hand, the stiffness will determine if the explosive actions are influenced by the structure or not. If the structure has enough stiffness, the explosive actions will not be influenced by the structural behaviour under loading. However, there are structures that deform or move in such a way that their behaviour changes the receiving loading [7].

2.3.1 UFC's simplifications

In order to facilitate the calculation of the structural response to actions resulting from a detonation, several simplifications are assumed in the UFC:

- The structure is generally rectangular in shape and positioned above the ground surface;

- The structure has enough stiffness not to influence the behaviour of the shock wave;

- The peak incident pressure of interest is $P_{so} = 1.38$ MPa (200 psi) or less;

- The Mach stem extends above the height of the building, i.e. the structure is being loaded by a plane shock wave front characteristic of the Mach stem region.

Pressure-time curve

For design purposes, the decay of the incident pressure is usually approximated to the rise of an equivalent triangular pressure pulse that can be observed in Figure 2.22.
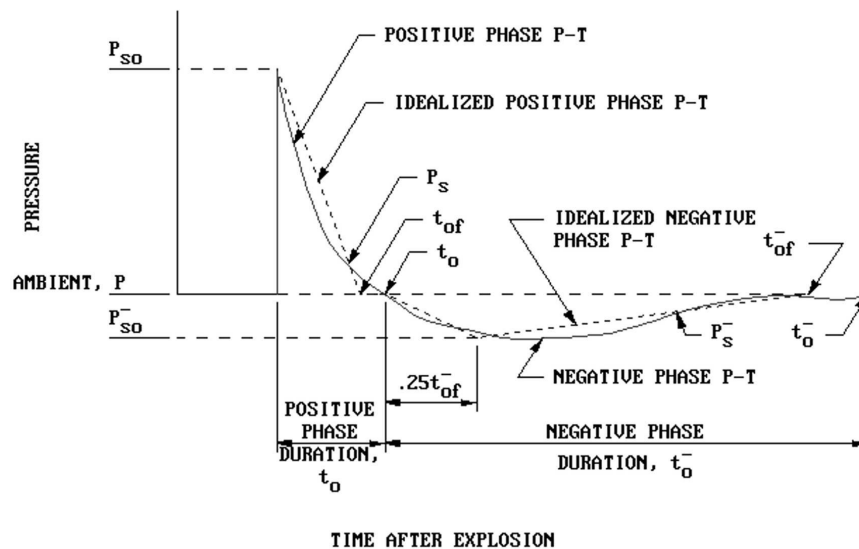
Figure 2.22: Idealized pressure-time variation [13]

However, in order to maintain the total positive impulse, it is necessary to replace the real positive duration by a fictitious duration expressed as a function of the total positive impulse and peak pressure:

$$t_{of} = \frac{2i}{P} \tag{2.21}$$

The relationship above is applicable to both the incident pressure and the reflected pressure, using, for the latter, the pressure and impulse values obtained for the reflected wave. Note that since the fictitious duration, t_{of}, is smaller in magnitude than the real duration, t_o, a time gap will occur between the fictitious duration and the beginning of the negative phase. This time gap, which is represented in Figure 2.22, should be maintained if one wants a full displacement analysis.

2.3.2 Front wall loads

The pressure-time history on a front wall exposed to a detonation with a normal incidence is illustrated in Figure 2.23.
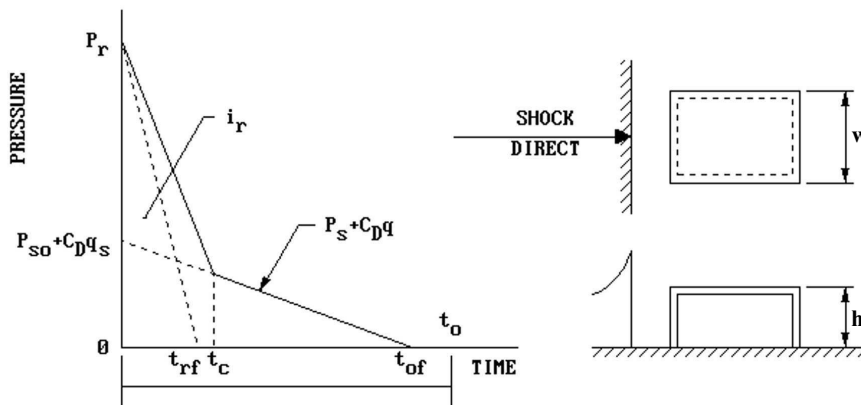
Figure 2.23: Front wall loading (normal reflection) (Adapted from [13])

When the shock front impacts the structure, the pressure immediately rises to the normal reflected pressure, P_r, which can be obtain through the abacus represented in Figure 2.21. After the initial impact, the reflected pressure is relieved in the clearing time, t_c [13]:

$$t_c = \frac{4S}{(1+R)\,C_r} \tag{2.22}$$

where S is the clearing distance given by either h or $w/2$, whichever is smaller, R is calculated by the S/G ratio where G is equal to either h or $w/2$, whichever is larger, and C_r is the sound velocity in the reflected region interpolated from Figure 2.24.

After the clearing time, t_c, the pressure acting in the front wall is characterized by the algebraic sum of the incident pressure P_s and the drag pressure $C_D \times q$, which
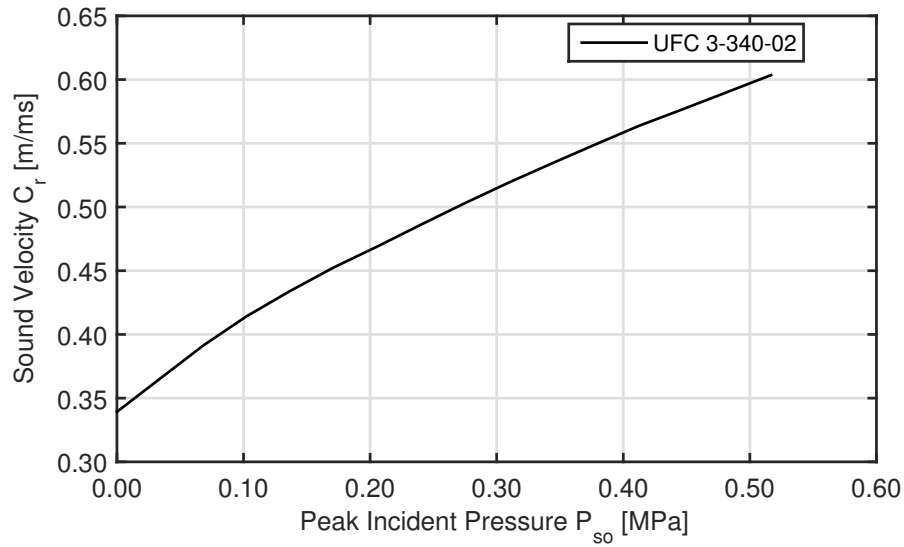
Figure 2.24: Sound velocity in the reflected overpressure region [13]

results from the multiplication of the drag coefficient C_D with the dynamic pressure q corresponding to P_s.

$$P = P_s + C_D \times q \tag{2.23}$$

The drag pressure is obtained through the drag coefficient which determines the relation between the dynamic pressure and the total translational pressure in the direction of the wind produced by the dynamic pressure, and varies with the Mach number and the relative geometry of the structure. Usually, a value of $C_D = 1$ is considered adequate for the pressure ranges assumed in the UFC.

However, for higher pressures, the drag coefficient above may produce an inadequate pressure-time history due to the extremely short impulse involved. Hence, one must verify the accuracy of the previous pressure-time curve through the construction of a second curve (dotted triangle presented in Figure 2.23) using the total reflected impulse i_r for a normal reflected shock wave. The new duration is obtained from:

$$t_{rf} = \frac{2i_r}{P_r} \tag{2.24}$$

Lastly, one must compare the resulting impulses from both methods and calculate the front wall loading with the method that results in the smaller impulse. The procedure above may be applied when the shock wave approaches the structure at an oblique angle. In this case, one must use the reflected pressure as a function of the incident pressure and the angle between the shock front and the front wall. This phenomenon can be observed in Figure 2.25 [13].

As referred above, generally only the positive phase is considered for the front wall design since the negative pulse seldom affects the design. However, in order to determine the overall motion of the structure, one must take into account the
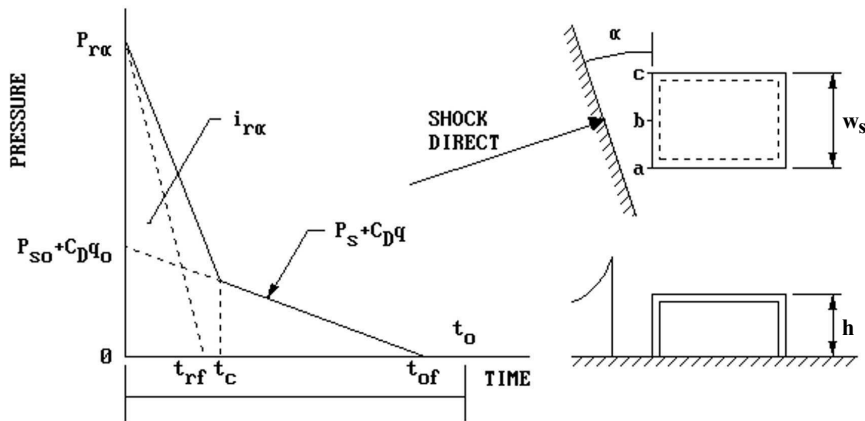
Figure 2.25: Front wall loading (oblique reflection) (Adapted from [13])

effects of the negative pulse.

2.4 Application to the case study

In order to obtain a better comparison between the reviewed formulations and to predict the panel's maximum displacements, the displacements resulting from the loads of a free-air burst will be analysed. Consider the shock wave resulting from the blast of 8 kg of TNT with the charge placed 3.0 m above the upper surface of the panel, as illustrated in Figure 2.26, which results in the scaled distance presented in Table 2.2.
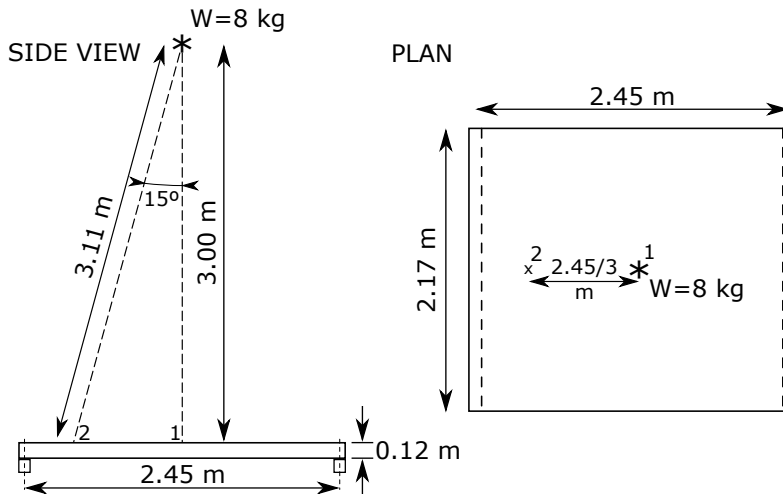
Figure 2.26: Free-air burst (Case study)

Through the formulations reviewed in Section 2.1.2, one can readily obtain the results presented in Tables 2.3 and 2.4 and the differences depicted in Table 2.5. Through the analysis of these results, one can verify that different formulations result in different blast wave parameters. Note that these differences reach a

Table 2.2: Scaled distance

Parameter	Point 1	Point 2
Weight [kg]	8.00	8.00
Distance [m]	3.00	3.11
Scaled Distance (Z) [m/kg$^{1/3}$]	1.50	1.56

maximum value of 57.56 % between the specific impulses. This difference is noticeable in Figure 2.5 when comparing the UFC's 5 kg curve with the Kinney and Graham's curve.

Table 2.3: Free-field parameters (UFC [13])

Point No.	P_{so} [MPa]	t_o [ms]	i_s [MPa.ms]
1	0.373	3.35	0.241
2	0.344	3.35	0.233

Table 2.4: Free-field parameters (K&G and R-H [23, 35])

Point No.	P_{so} [MPa]	t_o [ms]	i_s [MPa.ms]
1	0.406	1.76	0.10
2	0.374	1.83	0.10

Table 2.5: Difference between formulations

Point	P_{so}	t_o	i_s
1	8.13 %	47.39 %	57.56 %
2	8.03 %	45.36 %	56.86 %

For the present example, due to the panel's geometry, only the pressures acting on the exposed surface of the panel will be analysed. After the computation of the free-field blast parameters, one must compute the loading for the exposed surface of the panel. From the previous tables, one can observe that the blast parameters applied to the two points are different. However, according to [50], the blast load at mid-span of the panel can be used as an equivalent uniform load over the whole panel if there is not too much variation, which is limited to a 25 % reduction in the blast load over the two-thirds of the component span length. Considering the formulation presented in the UFC, one can calculate the reflected overpressure for both points as represented in Table 2.6 and observe that the reduction for this case is lower than the limit. Hence, the mid-span, Point 1, blast parameters will be considered as the blast load of the whole panel.

Afterwards, one can compute the values presented in Table 2.7 through the UFC's

Table 2.6: Reflected overpressures

	Point 1	Point 2	Reduction [%]
P_r [MPa]	1.51	1.31	13.33

and the Kinney and Graham and Rankine-Hugoniot's formulations, and verify that the two formulations conduct to different loading values, specifically with a difference of 36.02 % for the reflected impulse.

Table 2.7: Front surface loading

Formulation	P_r	i_r
	[MPa]	[MPa.ms]
UFC	1.506	0.668
K&G and R-H	1.699	0.428
Difference [%]	11.38	36.02

Analysing Figure 2.26, one can verify that the model, which will be tested as a slab, is simply supported at two ends, resulting in a cylindrical bending. Slabs with this behaviour are usually designed for flexure and shear on a per unit width basis, assuming that they act as a series of independent strips. Using the reflected impulse values presented in Table 2.7, one can compute the reflected impulse applied to a one meter strip of the panel for both formulations as:

$$I_r = i_r \times 1 \times L = i_r \times 2.45 = \begin{cases} I_r^{UFC} & = 1.637 \text{ [kN.s/m]} \\ I_r^{K\&G\ R-H} & = 1.047 \text{ [kN.s/m]} \end{cases} \tag{2.25}$$

In order to obtain the maximum displacement, a one meter strip can be accurately reproduced by idealizing a spring-mass system, as observed in Figure 2.27.
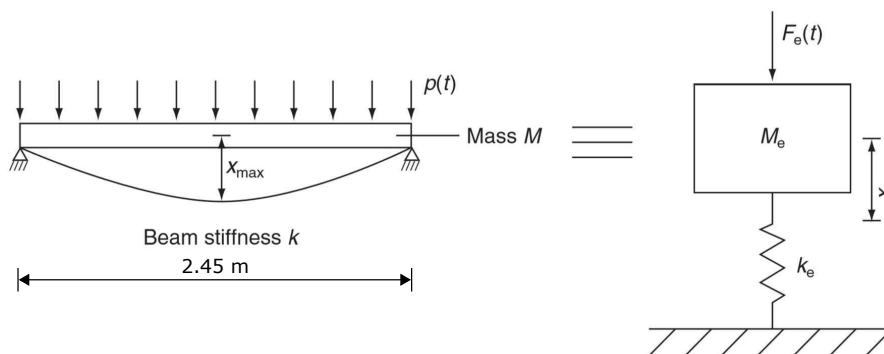
Figure 2.27: Idealization to a mass-spring system (Adapted from [43])

Afterwards, the Principle of Conservation of Energy can be used to determine the maximum displacement:

$$T = \Omega \tag{2.26}$$

where Ω is the strain energy of the panel, until the end of the explosion, and T is the kinetic energy, which can be defined for a spring-mass system as:

$$T = \frac{1}{2} M_{eq} v_{eq}^2 \tag{2.27}$$

Considering Newton's second law of motion:

$$\vec{F} = m \times \vec{a} = m \frac{\Delta \vec{v}}{\Delta t}$$

Through its application during the interaction time, one obtains:

$$\vec{F} \Delta t = m \Delta \vec{v}$$

Lastly, an impulse can be computed for a spring-mass system as:

$$I = \vec{F} \Delta t = m \Delta \vec{v}$$

Hence, one can define the kinetic energy as:

$$T = \frac{1}{2} \frac{I^2}{M_{eq}} \tag{2.28}$$

where, for the case study, the equivalent mass M_{eq} of the mass-spring system for a one meter strip is determined as:

$$M_{eq} = h \times 1.0 \times \frac{L}{2} \times \rho = 0.12 \times 1.0 \times \frac{2.45}{2} \times 2.5 = 0.368 \text{ [ton/m]}$$

Hence, the kinetic energy for the case study results in:

$$\begin{cases} T^{UFC} & = \frac{1}{2}\frac{1.637^2}{0.368} = 2.861 \text{ [kJ/m]} \\ T^{K\&G \ R-H} & = \frac{1}{2}\frac{1.047^2}{0.368} = 1.171 \text{ [kJ/m]} \end{cases} \tag{2.29}$$

Considering that the panel's materials and reinforcement bars have the characteristics presented in Table 2.8 and assuming a plastic behaviour of the reinforcement after yielding, a rectangular stress distribution for concrete in the compression zone and neglecting the compression in the rebars; where A_s is the area of the reinforcement bars, $f_{cm,cube}$ is the mean compressive strength

Table 2.8: Properties of the materials and reinforcement bars of the panel

A_s	$f_{cm,cube}$	$f_{cm} = 0.8 f_{c,cube}$	f_y	d	b
[cm^2/m]	[MPa]	[MPa]	[MPa]	[m]	[m]
1.964	46.0	36.8	500.0	0.0875	1.0

of concrete obtained through compression tests of cubic specimens, f_{cm} is the mean compressive strength of concrete obtained through compression tests of cylinder specimens, f_y is the characteristic yield strength of reinforcement and d is the effective depth; one can determine the moment capacity (M_r) of a one meter strip of the panel, whose width is represented by b, resorting to the following expressions:

$$\rho = \frac{A_s}{b\,d} = 0.002$$

$$M_r = \rho\,f_y\,d^2\left(1 - \frac{\rho\,f_y}{2\,f_c}\right) = 8.459 \text{ [kNm/m]} \tag{2.30}$$

where ρ is the reinforcement ratio. For the present case, the yield displacement at mid-span was considered to be small when compared to the maximum deformation. Additionally, the deformation of the panel until yield and the strain hardening of the reinforcement bars were not considered. Hence, the rigid-plastic behaviour depicted in Figure 2.28(a) was adopted. Lastly, in Figure 2.28(b), it is possible to observe the mid-span displacement and the support's rotation $\theta/2$, which result from the formation of a plastic hinge at mid-span.

(a) Strain energy   (b) Mid-span displacement
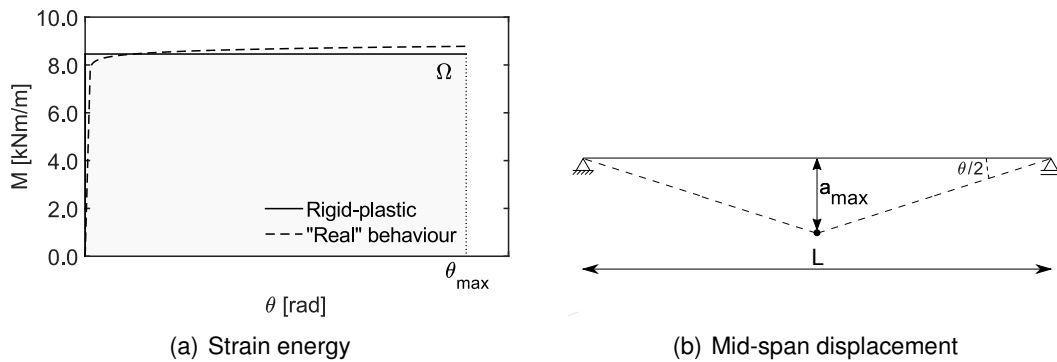
Figure 2.28: Idealisation of structural response

Therefore, the strain energy may be calculated as:

$$\Omega = M_r\,\theta \tag{2.31}$$

where

$$\theta = \frac{4\,a_{max}}{L}$$

Lastly, from the Principle of Conservation of Energy, one obtains:

$$\Omega = T = M_r\frac{4\,a_{max}}{L} \Leftrightarrow a_{max} = \frac{T\,L}{4\,M_r} = \begin{cases} a_{max}^{UFC} & = 264 \text{ [mm]} \\ a_{max}^{K\&G\ R-H} & = 108 \text{ [mm]} \end{cases} \tag{2.32}$$

Analysing the values obtained in equation (2.32), one can observe a difference of 59 % between them, which results from the differences between the formulations used to determine the blast parameters, as the method used to compute the maximum displacement was equal for both formulations.

Additionally, through the analysis of the free-air burst parameters, one can conclude that the presented formulations can lead to different results, with differences that reached approximately 60 %.

2.5 Structural response under dynamic loading

When loaded with rapidly changing loads, the behaviour of structures may change significantly when compared with their behaviour under static and quasi-static loads. This is more significant if the applied load has a high peak value and a short duration. In dynamic loadings, inertial effects appear due to the accelerating mass. However, these inertial effects lead to a resistance to speed changes that need to be considered in dynamic analysis. Every load applied to the structure will create a certain degree of deformation rates in different parts of the structure as these deform. If one considers rapidly changing loads, these deformation rates will be high and will create the commonly referred strain rate effects. These strain rate effects will highly affect the material's response, as they will lead to an increase in the material strength [26].

2.5.1 Material properties

As referred before, a material suffers an increase in its strength when subjected to dynamic loads. This is due to the inertial effects that appear when the structure resists to abrupt velocity changes provoked by shock wave's loads. Thereby, one must convert the static properties of the materials to their equivalent dynamic resistance through the use of the Dynamic Increase Factor (DIF). The procedure to incorporate the strain rate effects in the analysis is illustrated in Figure 2.29. A preliminary analysis must be performed without considering the strain rate effects. Afterwards, with the results obtained through the preliminary analysis, the strain rates are calculated for different materials, and the corresponding DIFs estimated. Performing the analysis again, incorporating the estimated DIFs, new strain rates are obtained and new DIFs are calculated and compared to the previous ones.

This iterative procedure must be performed until the new dynamic increase factors are close to the previous ones, then the analysis can be accepted as the final one.
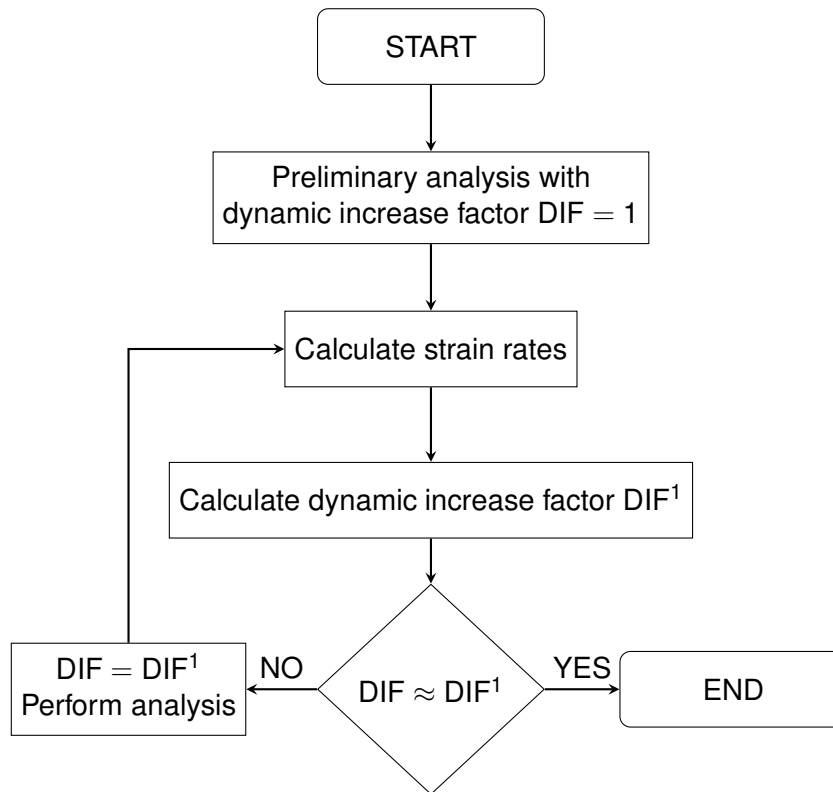
Figure 2.29: Procedure to incorporate the strain rate effects (Adapted from [4])

Dynamic properties of concrete

Several studies have experimentally defined the compressive and tensile strength of concrete at different strain rates. In Figure 2.30 one can observe the most commonly referred published results. The large scatter for the compressive behaviour of concrete might be due to the used experimental techniques and the diversity of methods employed in the analysis [6]. Therefore, one must be careful when comparing results from different authors. Through the analysis of the plots in Figure 2.30, one can verify the existence of two distinct intervals with different strain rate dependencies and a relatively sharp transition zone between them. The more moderate first dependency can be explained, for compression loads, by the build-up of internal pressure due to water movement inside the concrete, resulting in a delay of the crack initiation. A similar effect occurs when the specimens are subjected to tension loads, due to the resisting force of the water inside the micropores of the concrete. If the strain rates exceed the transition zone, the strain rate dependency can be attributed to lateral confinement and inertia effects, which can be explained as follows. An elastic material, such as concrete, statically loaded in compression, will suffer lateral expansion due to Poisson's ratio effect. However, if the compressive load is rapidly applied in the axial direction, the specimen will

not be able to instantaneously expand in the radial direction due to inertial restrain. This creates a finite lateral confinement, resulting in an increase in the compressive strength of the material [26].
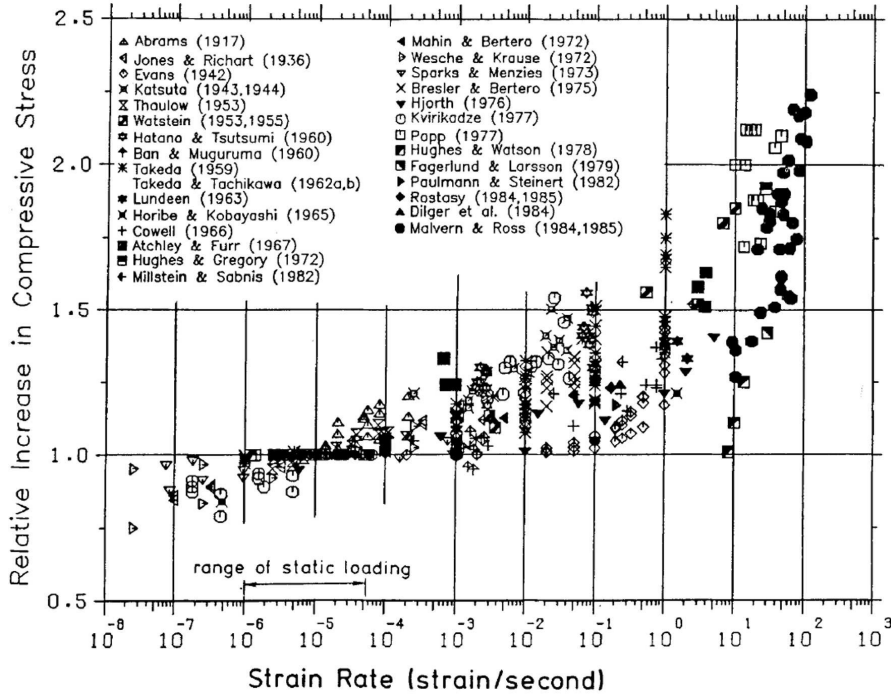
Figure 2.30: Strain rate effects on the concrete compressive strength [6]

A model for the strain rate dependence, valid for strain rates up to 300 s^{-1}, is presented in the CEB-FIP Model Code 1990 [30]. Figure 2.31(a) illustrates the CEB-FIP model for a 30 MPa compressive strength concrete. Additionally, Figure 2.31(b) represents the Malvar and Crawford's [27] model, which considers that a change in the tension curve's slope at 1 s^{-1} instead of 30 s^{-1}, as defined by the CEB-FIP model, fits the experimental tests' data better.

(a) Compression [30]

(b) Tension [27, 30]
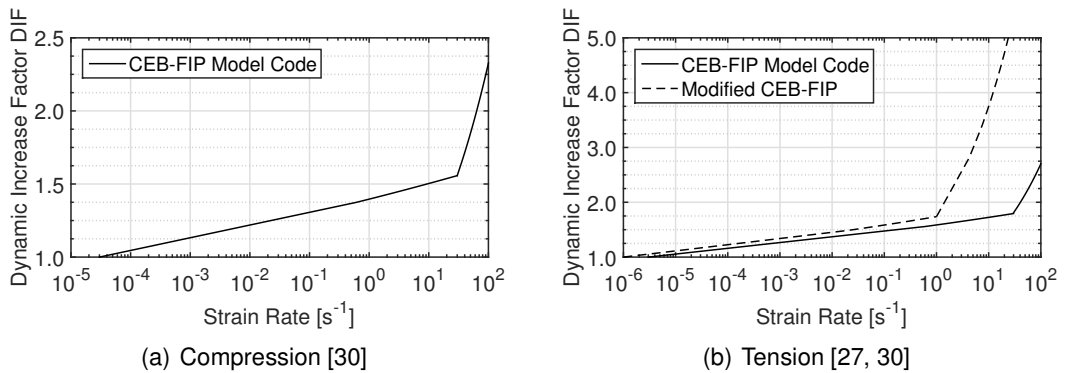
Figure 2.31: Dynamic increase factors for concrete

The Young's modulus of concrete is also affected by the strain rate. According to Bischoff and Perry [6], the increase of the Young's modulus for dynamic loadings might be due to the decrease in the internal micro-cracking, for a given stress level, as the strain rate increases. This results in the strain rate dependency model defined by the CEB-FIP Model Code 1990 [30] and illustrated in Figure 2.32.
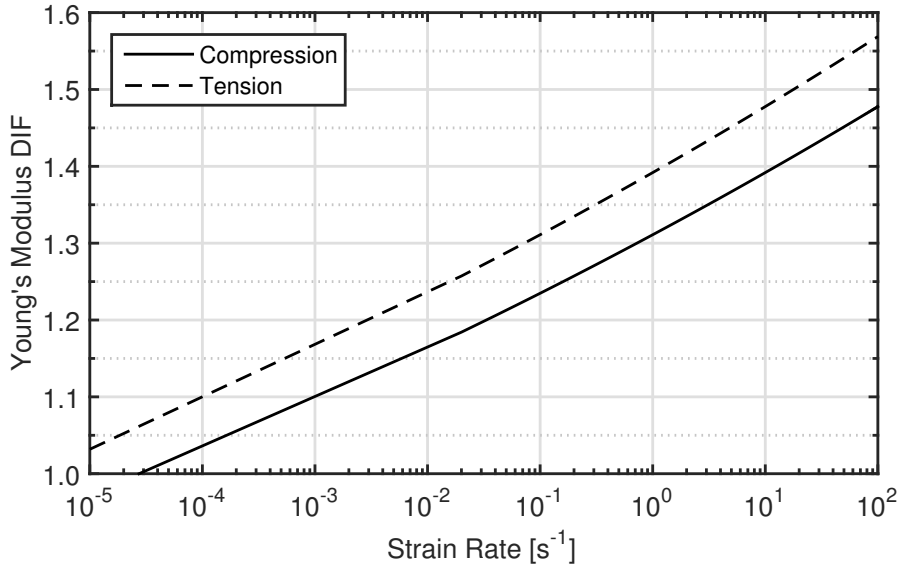
Figure 2.32: Dynamic increase factors for concrete's Young's modulus [30]

Dynamic properties of reinforcement steel bars

Similarly to the concrete, the steel used in reinforcement bars is also affected by the strain rate effects, increasing the values of the yield and the ultimate stresses. However, according to Malvar and Crawford [28], the Young's modulus remains constant regardless of the strain rate. Malvar and Crawford [28] proposed a formulation where the DIF can be approximated by a straight line in a logarithm of the DIF versus logarithm of the strain rate plot. The proposed formulation is, for both the yield and ultimate stress, defined as follows:

$$DIF = \left(\frac{\dot{\varepsilon}}{10^{-4}} \right)^{\alpha} \tag{2.33}$$

where for the yield stress, $\alpha = \alpha_{f_y}$

$$\alpha_{f_y} = 0.074 - 0.040 \frac{f_y}{414} \tag{2.34}$$

while for the ultimate stress, $\alpha = \alpha_{f_u}$

$$\alpha_{f_u} = 0.019 - 0.009 \frac{f_y}{414} \tag{2.35}$$

and where the strain rate $\dot{\varepsilon}$ is expressed in s⁻¹ and the yield stress f_y is expressed in MPa. The previous formulation only depends on the steel's f_y for both strengths,

being valid for steel bars with yield stresses between 290 and 710 MPa. According to this formulation, the yield stress's DIF gradient is higher than that for the ultimate stress, as depicted in Figure 2.33.
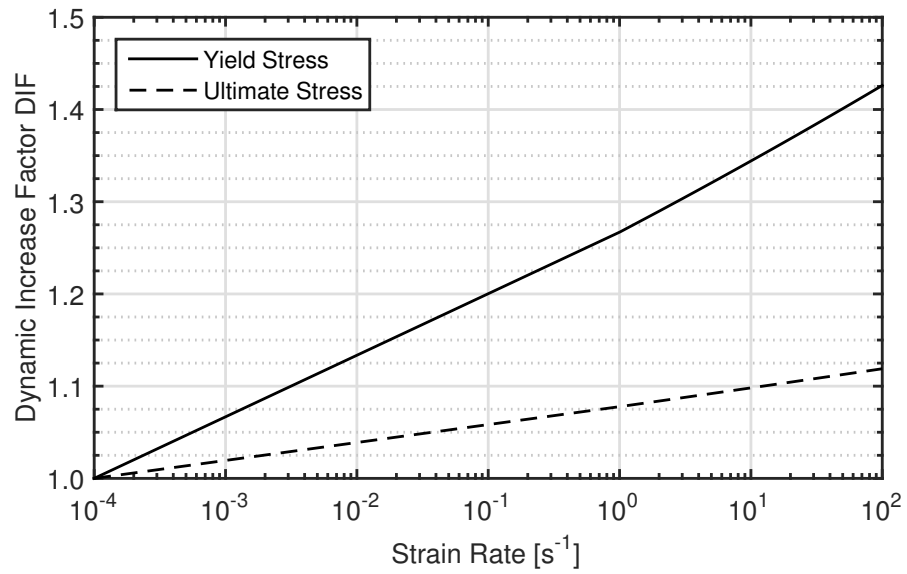
Figure 2.33: Dynamic increase factors for steel [28]

Chapter 3

Applied Element Method

The purpose of the present chapter is to review the Applied Element Method (AEM) formulation and its implementation in the commercial software *Extreme Loading for Structures* (ELS) [15].

3.1 Introduction

The method was developed in 1995 as part of Dr. Hatem Tagel-Din's research studies. However, only in 2000 the term *"Applied Element Method"* appear in a paper [31]. Since then, the method was applied and verified for: elastic analysis [31]; crack initiation and propagation; estimation of failure loads of reinforced concrete structures [49]; reinforced concrete structures subjected to cyclic loads [32]; buckling and post-buckling behaviour [33]; non-linear dynamic analysis of structures subjected to collisions and severe earthquakes [46, 47]; fault-rupture propagation [38]; non-linear behaviour of brick structures [29] and blast analysis [4, 10].

The numerical methods conventionally used in structural analysis can be classified into two categories. In the first category, the model is based in continuum material equations. The finite element method (FEM) is the most common example for the first category, with the division of the domain into finite elements with the respective material properties. The FEM yields good results for structural analysis before collapse, even if one consider non-linear materials and non-linear geometry. However, if the structure's behaviour advances to a discrete state, as a result of crack opening and propagation, the FEM looses its efficiency, as indicated in Figure 3.1.

On the other hand, the second category can be defined by the use of discrete element techniques, such as the extended distinct element method (EDEM), which allows the mechanical interaction between elements and can simulate the cracking process more easily when compared to FEM, depending, however, on the size, shape and arrangement of the elements. Despite its advantages, in small displacement analysis, the EDEM is less accurate than the FEM and the analysis time is quite large for a reasonable number of elements that simulate real problems.

In order to overcome the EDEM's drawbacks, Tagel-Din and Meguro developed the Applied Element Method [31]. The major advantage of the AEM is its capacity to simulate the structure's behaviour from zero loading until collapse, through the elastic phase, opening and propagation of cracks, yielding of reinforcement bars and separation and collision of elements, as illustrated in Figure 3.1. However, the computation time required to simulate large structures' behaviour from zero loading until collapse might become very large due to the necessity of small time increments, in order to ensure numerical stability.
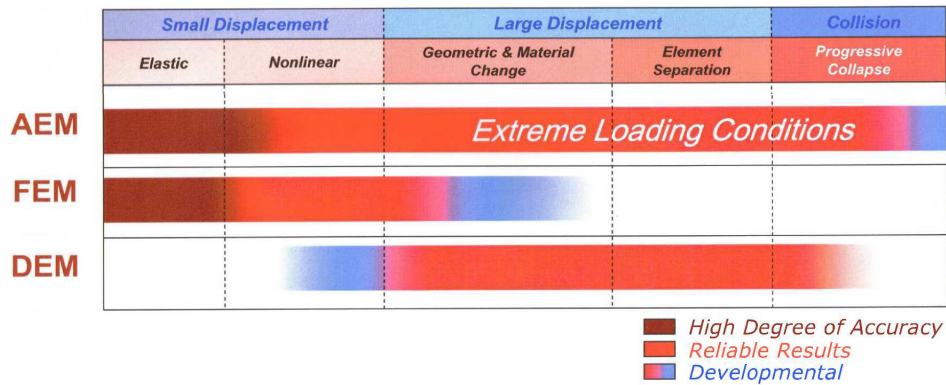
Figure 3.1: Analysis domain of AEM compared to FEM [2]

3.2 Element formulation

3.2.1 Small displacement analysis

The AEM models the structure as an assembly of small rigid elements, as represented in Figure 3.2. Adjacent elements are connected to each other by pairs of normal and shear springs distributed along the interface, which allow the total representation of the stresses and deformations of the studied elements. The axial (K_n) and shear stiffness (K_s) of each spring can be expressed as:

$$K_n = \frac{E\,d\,T}{a} \qquad \text{and} \qquad K_s = \frac{G\,d\,T}{a} \tag{3.1}$$

where d is the distance between springs, T is the thickness of the element and a is the length of the representative area, E and G are the Young's and shear modulus of the material, respectively.

As observed in Figure 3.2, each group of springs completely defines the stresses and deformations of a certain volume for 3D analysis or a certain area for 2D analysis. In the presence of reinforcement, this area is replaced by that of the reinforcement bar.

Three degrees of freedom (DOF) represent the rigid body motion of each element in the 2D formulation. Although the element's motion is a rigid body motion, the assembly of elements is deformable, and thus, its internal stresses and
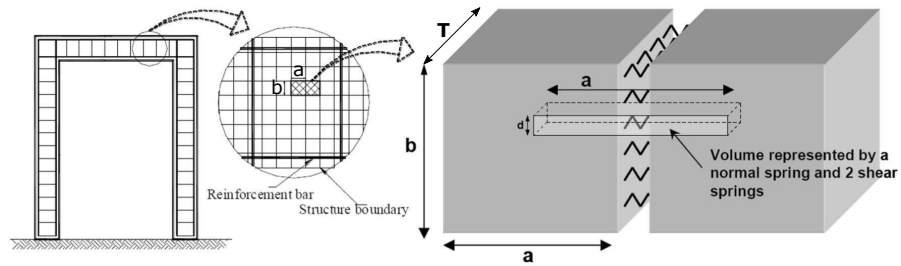
Figure 3.2: Modelling of structure to AEM (Adapted from [2])

deformations are calculated by its springs. In Figure 3.3 one can observe two 2D elements connected by a single pair of normal and shear springs with the stiffness defined in equation (3.1). It is also possible to observe the DOFs u_1, u_2, u_4 and u_5 representing the rigid body translations and the DOFs u_3 and u_6 representing the rigid body rotations of the elements. The relative position of the contact point with respect to the centroid can either be represented in cartesian coordinates with values of d_x and d_y or polar coordinates with the distance to the centroid defined by L and the angle between L and the face of the element where they are located defined by α.
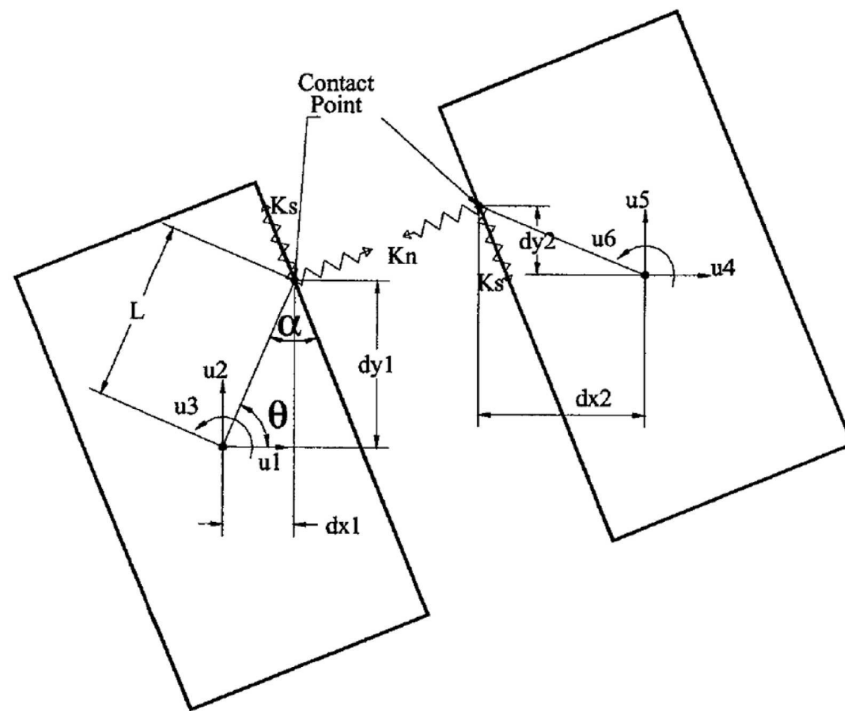
Figure 3.3: Element shape, contact location and degrees of freedom [33]

The commercial software *Extreme Loading for Structures* considers elements in a three-dimensional space with 6 degrees of freedom. In Figure 3.4 one can observe the loaded springs in an restrained adjacent element, through the application of a unit displacement in each DOF of the adjacent element.
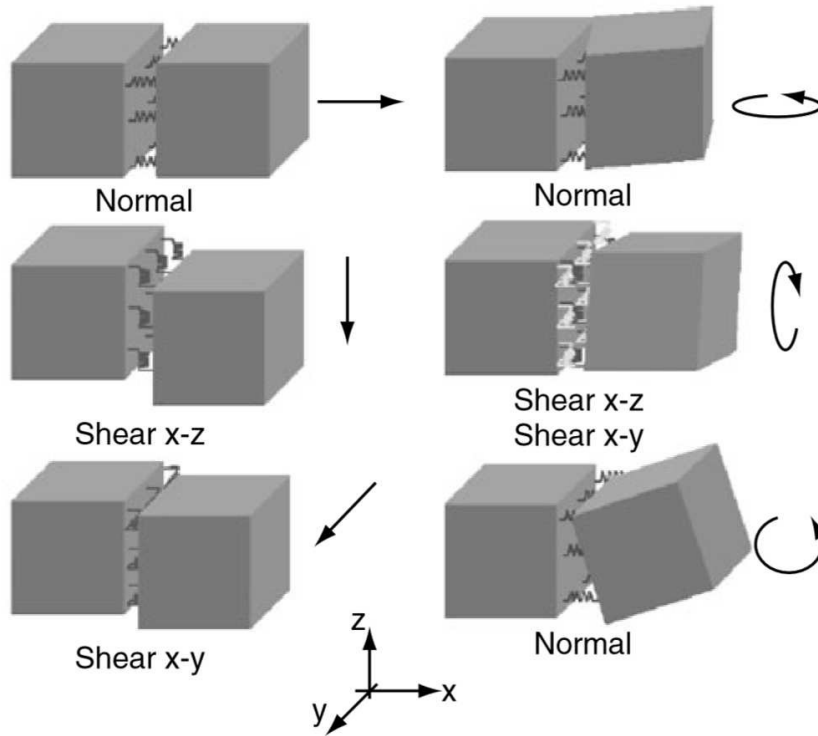
Figure 3.4: Rigid body translations and rotations [4]

The total stiffness matrix of each element results from the summation of the stiffness matrices of individual pairs of springs, which depend upon the axial and shear stiffness as well as the location of each spring. Hence, the resultant stiffness is an average stiffness matrix for the element, according to the stress situation around it. Referring to [31], it is possible to define the governing equation as:

$$\boldsymbol{K_G u} = \boldsymbol{f} \tag{3.2}$$

where $\boldsymbol{K_G}$ is the global stiffness matrix, $\boldsymbol{u}$ the displacement vector and $\boldsymbol{f}$ the applied load vector. The AEM allows for both load and displacement control. In the former, the applied load vector $\boldsymbol{f}$ is known before the analysis. However, in the latter, the load vector becomes unknown and must be determined through the application of a unit virtual displacement to one or more degrees of freedom.

Additionally, one must consider the element rotation, which is resisted by shear and normal springs. It is possible to calculate the theoretical rotational stiffness K_r from normal springs as [31]:

$$K_r = \int_{-b/2}^{b/2} \frac{E\,T}{b} z^2 \, \mathrm{d}z = \frac{E\,T\,b^2}{12} \tag{3.3}$$

where T is the element's thickness, E the Young's modulus, b the element's height and z the spring's distance to the element centroid as represented in Figure 3.5. Therefore, it is possible to obtain the element's rotational stiffness as the sum of

each spring's rotational stiffness, which leads to:

$$K_r = \frac{E\,T\,b^2}{4\,n^3} \sum_{i=1}^{n} (i - 0.5)^2 \tag{3.4}$$

where n is the number of springs and i the spring number.
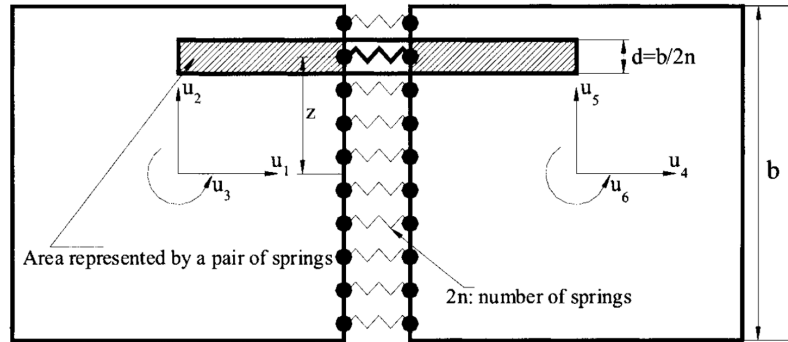
Figure 3.5: Normal springs for rotational stiffness [31]

3.2.2 Large displacement analysis

While using FEM, one must use a geometrical stiffness matrix in order to consider large displacement effects. In AEM there is no need for such matrix, which results in a more general and applicable method for any type of loading. However, in static analysis, the AEM assumes that the direction of the applied force is constant. This results in a limitation because, for example, when a member buckles, the force's direction changes and this change cannot be analysed by the AEM [33].

To adapt the formulation reviewed in the previous section to account for large displacements, the following modification to equation (3.2) is introduced [33]:

$$K\Delta u = \Delta f + r_m + r_G \tag{3.5}$$

where K is the non-linear stiffness matrix, Δu the incremental displacement vector, Δf the incremental load vector, r_m the residual force vector due to cracking or incompatibility between stress strains and stresses and r_G the residual force vector due to geometrical changes in the structure during loading. The previous equation is solved in the AEM through the following steps [33]:

1. Vectors r_m and r_G are defined as null and equation (3.5) is solved to obtain Δu;

2. The structure's geometry is modified according to the calculated incremental displacements;

3. Modify the direction of the spring's force vectors according to the new element configuration. The geometrical changes generate incompatibility between the applied forces and internal stresses;

4. Verify if cracking occurred and calculate r_m. When performing elastic analysis, r_m remains null;

5. Calculate the element's force vector f_m, through the summation of the spring forces around each element;

6. Calculate the geometrical residues around each element with equation (3.6);

$$r_G = f - f_m \tag{3.6}$$

where f is the applied load vector. The previous equation implies that the geometrical residues account for the incompatibility between the external applied and internal forces due to the modification of the structure's geometry.

7. Calculate the structure's stiffness matrix with the new configuration and considering stiffness changes due to cracking or yielding;

8. Repeat the entire process.

In order to reduce computation time, residues calculated in the previous increment are incorporated in the solution of equation (3.5). However, the method presents the following limitations:

- In buckling analysis, complete symmetry of the structure and loading must be avoided, thus ensuring the start of the buckling. The symmetry can be broken by slight changes in the material properties;

- One must use small increments of load and displacement because small displacement's theory is assumed during each increment;

- In load control analysis with a positive increment, the cumulative difference between the applied and internal loads increases after buckling. This results in large geometrical changes within a few increments. Hence, displacement analysis is suggested to overcome this problem.

3.2.3   Dynamic analysis

Referring to [48], one can observe that the general dynamic equation of motion for small deformation range is given by:

$$M\Delta\ddot{u} + C\Delta\dot{u} + K\Delta u = \Delta f(t) - M\Delta\ddot{u_G} \tag{3.7}$$

where M, C and K are the matrices of mass, damping and non-linear stiffness, respectively; $\Delta f(t)$ is the incremental applied load vector; Δu is the incremental displacement vector and $\Delta\ddot{u}$, $\Delta\dot{u}$ and $\Delta\ddot{u_G}$ are the incremental acceleration, velocity and gravity acceleration vectors, respectively. The differential equation (3.7) is solved numerically using the Newmark Beta technique [37].

According to [48], the AEM considers the element mass and inertia lumped at the element's centre, which results in a diagonal positive definite matrix. In a diagonal

positive definite matrix, all elements should be greater than zero. This matrix is very important in rigid body analysis because inertia forces play an important role in failure mechanisms during collapse.

When analysing reinforced structures, the AEM deals with structural damping through the consideration of the following sources:

- Cracking of concrete;

- Energy dissipation during the loading and unloading process when contact occurs;

- Unloading of reinforcement after yielding;

- Friction between elements during contact;

- Energy dissipation due to the process of crack opening and closure.

The previously presented damping sources only affect the structural behaviour in the non-linear stage. Therefore, the material damping matrix C accounts for other sources of damping with dominant effects in the elastic stage in order to obtain a more precise analysis. The damping matrix is calculated based on the fundamental mode of deformation as follows:

$$C = r\,M = 2\,\zeta\,\omega_1\,M \qquad (3.8)$$

where ζ is the damping ratio and ω_1 is the first natural frequency of the structure. Thereby, one must estimate the structure's first natural frequency in order to determine the damping ratio r. This ratio has a default value of zero because in most non-linear analysis cases, internal damping is sufficient to ensure good accuracy. However, if one uses an elastic material, the factors above will not occur. Hence, one must use the damping factor to account for viscous damping. However, the consideration of external damping causes a deceleration force on falling objects, which results in objects falling "unrealistically" slow [2].

Large displacement range

In order to consider large displacements under dynamic loading conditions, the general dynamic equation of motion becomes:

$$M\Delta\ddot{u} + C\Delta\dot{u} + K\Delta u = \Delta f(t) + r_m + r_G \qquad (3.9)$$

The term r_m simply represents the additional load vectors due to the non-linear behaviour of the material, while r_G represents the effects due to geometrical changes as previously explained. The algorithm adopted in the AEM to solve equation (3.9) is the following [48]:

1. Obtain internal forces under static conditions due to gravity loads;

2. Apply a load increment, $\Delta f(t)$;

3. Assume that r_m and r_G are null and solve equation (3.9) using the Newmark Beta method in order to obtain the incremental displacement, Δu;

4. Compute incremental strains and stresses;

5. Calculate incremental and total velocities and accelerations;

6. Modify the geometry of the structure according to the calculated incremental displacements;

7. Modify the direction of spring force vectors according to the new structural configuration. This leads to a incompatibility between applied loads and internal stresses, damping forces and inertia forces;

8. Check cracking evolution through the calculated stresses and calculate the material residual load vector r_m;

9. Calculate the element force vector from the adjacent springs of each element f_m;

10. Calculate the geometrical residual load vector around each element as follows:

$$r_G = f(t) - M\ddot{u} - C\dot{u} - f_m \qquad (3.10)$$

Note that residual forces are calculated based on total stress value and gravity forces are considered as an external applied force.

11. Calculate the stiffness matrix with the structure in the new configuration, considering stiffness changes at each spring location due to cracking and/or yield of reinforcement;

12. Apply a new load increment and repeat the procedure starting from step 2.

As referred in Section 3.2.2, material and geometrical residuals calculated from the previous increment can be incorporated in the solution of equation (3.10) to reduce calculation time. In order to obtain accurate results, one should use small time steps because the previously defined procedure considers small deformations during each increment.

In the case of static loading conditions, this technique is applicable by setting the mass and damping matrices to zero. However, element separation is not permitted in static analysis as it results in a singular stiffness matrix, i.e. equation 3.9 becomes impossible.

3.3   Material modelling

In the Applied Element Method, the structure is simulated as an assembly of virtually separated elements connected between each other by springs, which contain the material properties of the structure.

Because the present dissertation analysed only prefabricated reinforced concrete structures, the only material models addressed in the following sections refer to concrete and steel.

3.3.1 Concrete model

The adopted material model for concrete is the Maekawa's non-linear model [36]. Its generic stress-strain curve is presented in Figure 3.6. In this model, through the definition of the initial Young's modulus, the fracture parameter (representing the extent of the internal damage in concrete) and the compressive plastic strain it is possible to define the envelope for compressive stresses and compressive strains. Additionally, a linear model is considered until the ultimate tension strain is reached. Hence, it is possible to simulate unloading and reloading for compression and a fracture model for tension.
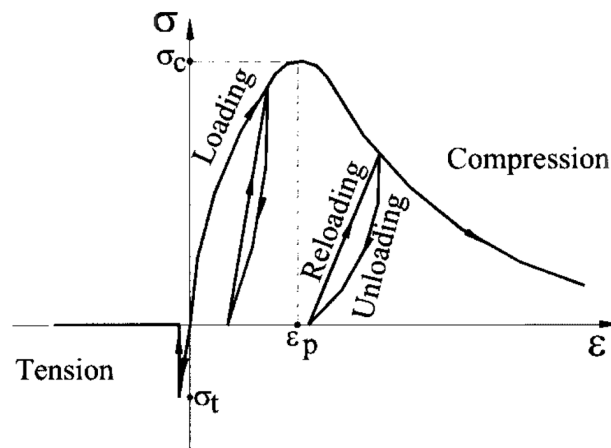
Figure 3.6: Maekawa's compression and tension model for concrete [36]

While the initial Young's modulus is a characteristic of the material, the tangent modulus is calculated according to the strain at the spring location. Additionally, in order to consider the confinement effects in compression zones, Kupfer's [25] biaxial failure function is considered. Hence, the modified compressive strength, f_{ceq}, is calculated as a function of the principal stress components (σ_1 and σ_2) and the compression stress f_c as follows:

$$f_{ceq} = \frac{1 + 3.65\,(\sigma_1/\sigma_2)}{(1 + \sigma_1/\sigma_2)^2} f_c \tag{3.11}$$

Once the spring's tension reaches the ultimate compression strength, the spring's stiffness is assumed as 0.1% of the original value in order to maintain connection between elements and avoid negative stiffness values. This leads to a difference between the calculated stresses and the stress that corresponds to the spring's strain, which develops residual stresses that are redistributed in the next step of loading trough the application of equivalent forces in the opposite direction. For concrete springs subjected to tension, the spring's stiffness is assumed as constant

until the spring reaches the cracking point. After this point, stiffness is set to be zero and the residual stresses are redistributed.

As reviewed, normal spring's tensions after cracking are redistributed to have zero tension stress. However, there may be some resistance in the shear's direction due to the effect of friction and interlocking between the cracked faces. This effect is taken into account through a redistributed value (RV), as shown in Figure 3.7.
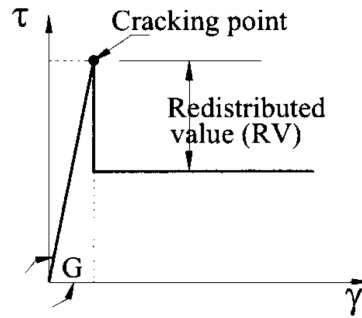
Figure 3.7: Shear model for concrete [49]

Cracking criteria

The AEM resorts to Mohr-Coulomb's failure criteria to define crack opening and propagation. However, using elements through the virtual division of a structure, which is not really composed of elements, such as concrete structures, and applying the Mohr-Coulomb's failure criteria calculated from normal and shear springs, and not based on principal stresses, might lead to inaccurate simulation of the fracture's behaviour [49].

Hence, in order to overcome this problem, the AEM resorts to the spring stresses present around each element to detect the occurrence of cracks. In Figure 3.8, one can observe that the shear and normal stress components, τ and σ_1, are determined from the shear and normal springs attached to contact point (A).

The secondary stress, σ_2, can be calculated through equation (3.12) from normal stresses at points (B) and (C), as illustrated in Figure 3.8.

$$\sigma_2 = \frac{x}{a}\sigma_B + \frac{(a-x)}{a}\sigma_C \qquad (3.12)$$

It is now possible to calculate the principal stress as:

$$\sigma_p = \left(\frac{\sigma_1 + \sigma_2}{2}\right) + \sqrt{\left(\frac{\sigma_1 - \sigma_2}{2}\right)^2 + (\tau)^2} \qquad (3.13)$$

Afterwards, the principal stress σ_p is compared with the tension resistance value defined for the studied material. If σ_p exceeds the tension resistance value, the normal and shear spring forces are redistributed in the next increment through the
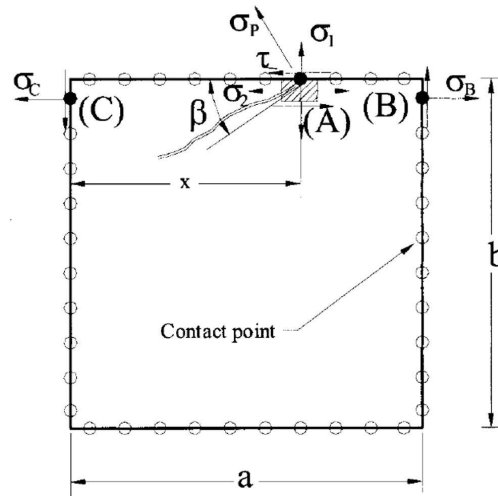
Figure 3.8: Principal stress determination [49]

application of normal and shear spring forces in the reverse direction. These forces are transferred to the element's centre as a force and a moment and applied to the structure in the following increment.

One must note that the redistribution of springs' forces at the crack location is very important to properly follow the crack propagation. While in normal springs the whole force is redistributed to have zero tension at crack faces, this is not the case for shear springs, where the cracking tension might have some resistance due to friction and interlocking. However, in the AEM the shear stiffness is assumed to be zero after cracking. In order to consider the previously described effects, the method adopts the redistributed value (RV) illustrated in Figure 3.7, which depends on the aggregate interlock and friction at the crack surface.

The local crack inclination angle relative to the element's edge β, as shown in Figure 3.8, can be obtained as follows:

$$\tan{(2\beta)} = \left(\frac{2\tau}{\sigma_1 + \sigma_2}\right) \tag{3.14}$$

Lastly, if the shear springs are subjected to compression stresses, Mohr-Coulomb's failure criteria is applied for shear compression failure. When shear compression failure is verified, the shear force is redistributed and shear stiffness is assumed to be null in the following increments.

After the determination of the failure criteria, it is possible to analyse the cracking of the whole element. There are two techniques to deal with the occurrence of cracks. The first one, which is not used in the reviewed method, breaks the elements into two segments with three DOFs, as depicted in Figure 3.9(a). The second one, illustrated in Figure 3.9(b), assumes that the failure inside the element is represented by the failure of connection springs.

(a) Element separation into two segments (Not used in AEM)

(b) Redistribution of spring forces at element edge
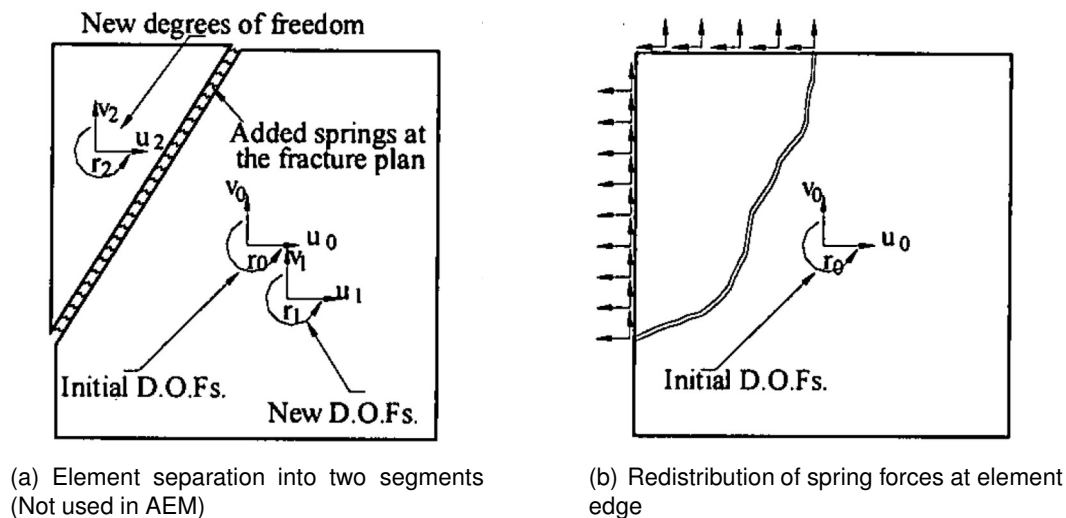
Figure 3.9: Techniques to deal with cracking [49]

Although the first technique is more accurate, the method uses the second one due to the absence of the following complications [49]:

- The increase in the number of elements would be too great;

- The time of analysis would increase after cracking due to the increase in the number of elements;

- The stiffness of springs at the cracked elements cannot be accurately calculated as before;

- In the case of cyclic loading, successive cracking of the same elements would lead to a drastic decrease in the solution's accuracy;

- Numerical errors appear due to the small aspect ratio of cracked elements.

Additionally, the second technique is simpler and has the advantage of not requiring special treatment to simulate and represent crack opening and propagation. High accuracy is expected in cases where the shear stresses are not dominant, which lead to an angle β close to zero, because the crack's direction is parallel to the element edge. On the other hand, if shear stresses are dominant, one must reduce the size of the elements in order to enable a more realistic cracking behaviour. Another disadvantage of the method is the impossibility to calculate with accuracy the crack width, which might modify the post-cracking behaviour.

The formulation above can be extended to the 3D case as well.

3.3.2   Reinforcement bars model

The reviewed method uses the constitutive model presented by Ristic [40] for steel reinforcement bars. Its generic stress-strain curve is illustrated in Figure 3.10. The

tangent stiffness of the reinforcement bars is calculated using the strain present in the reinforcement's spring, the loading status (either loading or unloading) and the previous loading history, which controls the Bauschinger's effect.
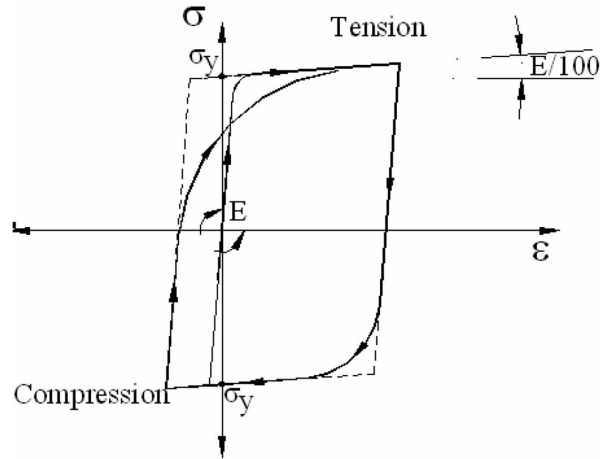
Figure 3.10: Ristic's constitutive model for steel [40]

However, the implementation of the Ristic's constitutive model in the commercial software ELS [15] does not consider the buckling of the reinforcement bars [32].

3.4 Poisson's ratio effect

The Poisson's ratio effect is taken into account in two-dimensional analysis through the correlation of each element's stiffness matrix with that of the adjacent elements. Even if all the elements move as a rigid body, the assembly of elements is deformable.

To explain the procedure, in Figure 3.11 one can observe the effects of an horizontal displacement of one element (element 0) surrounded by restrained elements. This results in springs subjected to compression, represented by A in Figure 3.11. These compression forces result in a lateral (vertical) displacement, in the area defined as A', which is a function of the Poisson's ratio. However, this resultant vertical displacement is restrained by the surrounding elements' restrained degrees of freedom, leading to additional stresses in A'. These stresses, assumed as uniform over the element edges, are transformed into a force and a moment applied to the element centre and added to the global stiffness matrix.

However, there is another approach that can be used to account for the Poisson's ratio effect. This approach consists in the addition of two degrees of freedom to the two-dimensional elements. This increases the number of degrees of freedom to each element from 3 to 5. Three degrees of freedom (u, v and r) for rigid body motion and two additional components (uu and vv) for the relative deformations between the vertical and horizontal edges, as depicted in Figure 3.12.
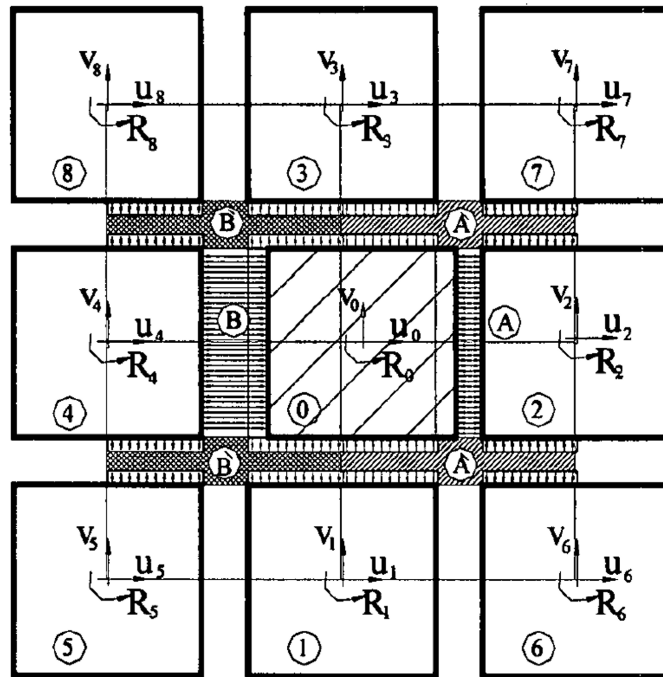
Figure 3.11: Secondary stresses due to element's 0 horizontal displacement [31]
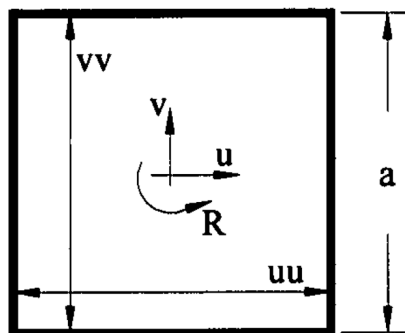
Figure 3.12: Degrees of freedom to consider Poisson's ratio effect [31]

The uu and vv correlate the deformations of the element's edges based on the Poisson's ratio by adding these effects to the stiffness matrix and, therefore, considering Poison's ratio effects. However, due to the increase in the number of the degrees of freedom, analysis time is longer. Additionally, a coupling effect occurs between the degrees of freedom associated with rigid body motion and those associated with relative deformations. Hence, this technique is not implemented in the AEM.

Despite the successful application of Poisson's ratio effect to two-dimensional cases, the *Extreme Loading for Structures* does not consider this effect in three-dimensional analysis due to the increased analysis time and the relatively small effect to most problems [2].

3.5 Elements contact

The AEM's formulation implemented in the commercial software ELS considers the effect of collisions, contact and re-contact between elements. In order to simplify the problem, the element's shape is assumed to be circular or spherical during contacts in 2D or 3D analysis, respectively, as illustrated in Figure 3.13. This assumption is acceptable if the element's size is relatively small. However, if relatively large elements are used, it might still be reasonable because in the deformation range of collision, sharp corners of elements are broken due to the stress concentration and the edges of the elements become round. Based on the previous phenomenon, the AEM only calculates the distance between the elements' centres to check for collisions [46].
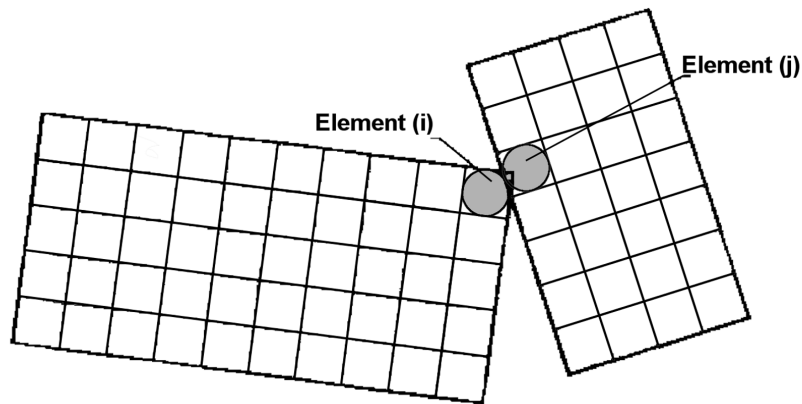
Figure 3.13: Two-dimensional collision between elements (i) and (j) [46]

Checking for collisions between an element and all other elements using global coordinates would result in a very long calculation time. To overcome this problem, the geometrical coordinates technique is used. Through the application of a coordinate system to each element, that depends on the element's location, collisions are checked between an element and its neighbour elements, instead of all elements, resulting in a smaller computation time. If collision occurs, normal and shear collision springs are added to the element's edge, as represented in Figure 3.14. The normal spring's direction passes through the centroid of the elements, while shear spring's direction is tangent to the assumed circles.

As reviewed, while a collision between two elements occurs, collision springs are added between the elements to represent the material behaviour during contact. Hence, the need to set the stiffness of the normal and shear springs arises. The normal spring stiffness is obtained through the following equation:

$$k = \frac{E\,A}{D} = \frac{E\,(N_F \times D)\,D}{D} = E\,N_F\,D \tag{3.15}$$

where E is the minimum Young's Modulus of the two elements, D is the average distance between element centres and N_F is the normal contact stiffness ratio which is assumed by default as 0.01, although it might be changed by the user. The
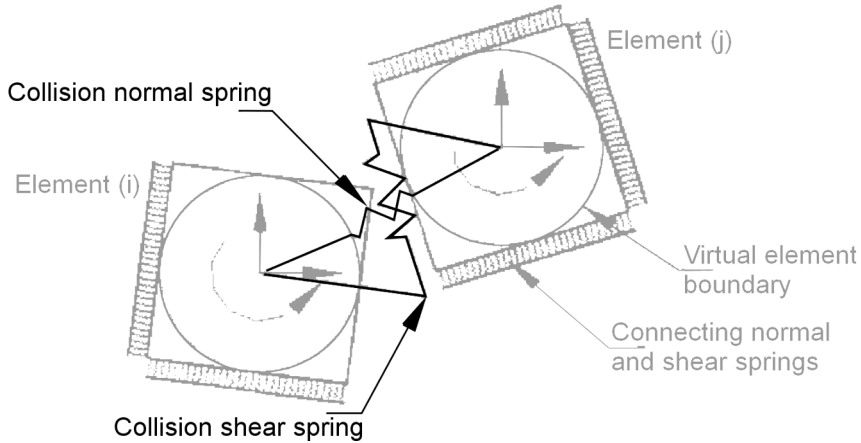
Figure 3.14: Spring formation in collision process [46]

product between $N_F D$ and D results in the contact area A illustrated in Figure 3.15.
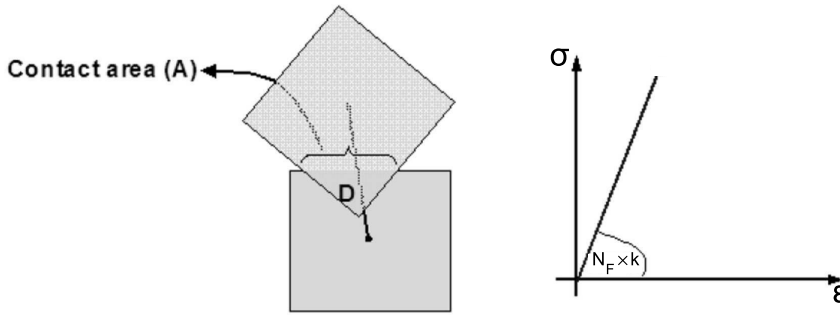
Figure 3.15: Contact normal spring factor (Adapted from [2])

Alternatively, the contact shear spring factor depends mainly on the friction properties between the elements.

$$k = G \, S_F \, D \qquad \text{if } V < \mu N \tag{3.16a}$$

$$k = \frac{G \, S_F \, D}{1000} \qquad \text{if } V > \mu N \tag{3.16b}$$

where G is the minimum Shear Modulus of the two elements, S_F is the contact shear stiffness ratio, D is the average distance between element centres, as illustrated in Figure 3.16, μ is the friction coefficient and N and V are the applied normal and shear forces, respectively.

During the collision of elements, some kinetic energy is dissipated. The rebound factor r is defined as the ratio between the element's relative velocity before and after collision, and its values vary between 0 and 1. One can use the rebound factor and momentum theory to represent energy dissipation during the collision process.
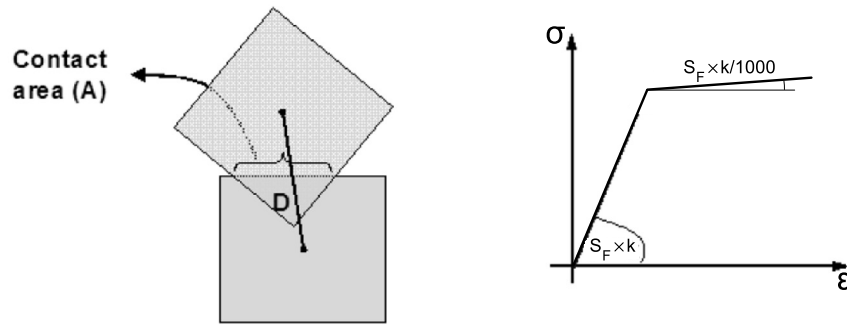
Figure 3.16: Contact shear spring factor (Adapted from [2])

However, this simple technique applied to continuum material like concrete requires a very small time increment in order to simulate the transmission of the stress wave through the other elements.

In order to save computation time, the AEM resorts to the load-displacement relation of a spring during loading (approaching) and unloading (leaving), as illustrated in Figure 3.17 [46].
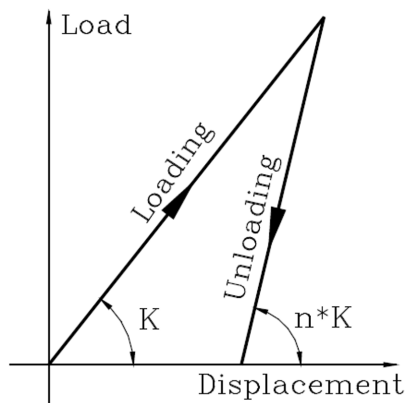
Figure 3.17: Shear contact spring factor [2]

Referring to Figure 3.17, one can define factor n, which represents the ratio between the unloading and loading stiffness and should be greater than 1. If there is no energy dissipation during contact, n should take a value of 1. This unloading factor can be correlated with the rebound factor r by equating the rebound energy of elements in both techniques, the obtained correlation is:

$$r = \frac{1}{\sqrt{n}} \tag{3.17}$$

Through this correlation, one can conclude that both techniques can be used to simulate energy dissipation during contacts. The main advantage of the latter is that the used time increment can be smaller during collisions and larger after separation.

Chapter 4

Case Study

The present chapter describes all the experimental tests reported by Gonçalves [18], which are used, in the present dissertation, to verify the applicability of the AEM when simulating the blast load effects on RC panels strengthened with fibre reinforced grout. Afterwards, it defines the numerical model that was created and calibrated using the results of the experimental field tests in order to allow the correct simulation of the experimental models' response to blast effects. Lastly, the obtained numerical results are presented and compared to the experimental tests.

4.1   Definition of the experimental models

The experimental campaign presented by Gonçalves [18] was designed to analyse the effects of blast loads on RC slabs strengthened with three solutions. Note that all three strengthening solutions are formed by a reinforced cement-based grout. Hence, in order to study the improvement in the structures' behaviour when subjected to blast loads due to the application of these reinforcements, four experimental models were created from façade panels, represented in Figure 4.1, three of which were strengthened, each by one type of reinforcement, and a fourth with no reinforcement. Additionally, one should observe in Figure 4.1 two false joints approximately 1.5 cm deep, which were created due to aesthetic reasons.

As previously stated, all three types of strengthening solutions are formed by a reinforced cement-based grout. However, the steel reinforcement used in the cement-based grout was different for each type of strengthening solution. In strengthening type A, a galvanized steel stretched mesh was used. In strengthening types B and C, continuous steel fibres were embedded in the cement-based grout. Namely, 1 % of the grout's volume was applied in one direction for strengthening type B, while on strengthening type C, 0.5 % of the grout's volume was applied in two orthogonal directions.

The experimental models were obtained through the cut of two prefabricated façade panels with 4.34 by 2.6 m and 0.12 m thick. This cut was made due to the weight of the prefabricated façade panels (approximately 3.4 tons each) and enabled the creation of four experimental models.

Figure 4.1: Prefabricated façade panels before cutting [18]

4.1.1   Geometrical definition

The final geometry of each experimental model, obtained with a cutting floor machine, was 2.6 by 2.17 m and 0.12 m thick. Each experimental model contained two NC50 reinforced steel meshes and two reinforcement bars ϕ12 on the edges. In Figure 4.2, the detailing of the reinforcement bars can be observed and the absence of the two reinforcement bars at the cut edge verified.
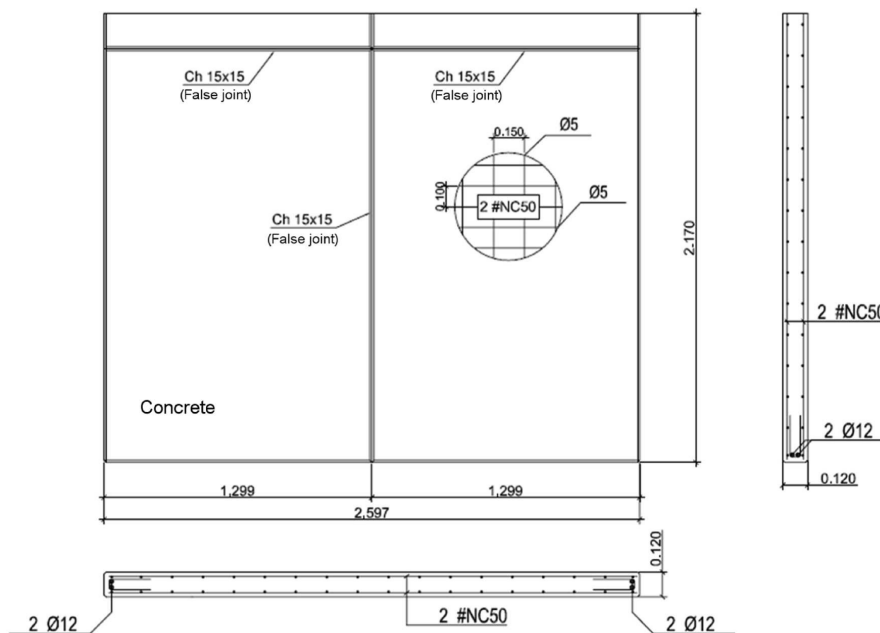
Figure 4.2: Experimental model detailing [18]

The geometrical properties of the NC50 reinforcement bars mesh are presented in Table 4.1.

Table 4.1: NC50 reinforcement bars mesh properties [9]

Direction	Diameter	Distance between axis
	[mm]	[mm]
Longitudinal	5.0	100
Transversal	5.0	150

4.1.2 Material properties

The materials used for the construction of the prefabricated panels are listed bellow:

- Concrete: NP EN 206-1; C30/37; Cl 1.0, D_{max}1.4; F5[1];

- Reinforcement type A: Galvanized steel stretched mesh [18] (Not modelled in the present dissertation);

- Reinforcement type B: Unidirectional Fibre Reinforced Grout (UFRG) with 1% of steel fibres [18];

- Reinforcement type C: Fibre Reinforced Grout (FRG) with 0.5% of steel fibres in both orthogonal directions [18] (Not modelled in the present dissertation);

- Reinforcement bar mesh: A500 ER[2];

- Reinforcement bars: A500 NR-SD[3].

Concrete

The mean secant modulus of elasticity (E_{cm}), characteristic compressive cylinder strength (f_{ck}) and the mean tensile strength (f_{ctm}) of a C30/37 class concrete, according to the NP EN 206-1 [20], are defined in Table 4.2.

Table 4.2: C30/37 properties according to the NP EN 206-1 [20]

Class	E_{cm}	f_{ck}	f_{ctm}
	[GPa]	[MPa]	[MPa]
C30/37	33	30	2.9

However, the compressive strength of concrete cubes was determined according to the NP EN 206-1 [20]. This property was determined 2, 7 and 28 days after the concrete's casting. In Table 4.3 the results from these tests can be observed.

Through the analysis of Table 4.3, the experimental mean compressive strength at 28 days of $f_{cm,cube} = 46$ [MPa] will be considered in order to calibrate the concrete's behaviour when subjected to compression stresses.

---

[1]C30/37 concrete resistance class, with a chloride class of Cl 1.0, maximum aggregate size shall be 1.4 mm and with a specified flow class of F5

[2]Cold worked steel with a characteristic yield stress of 500 MPa

[3]Hot rolled steel with a characteristic yield stress of 500 MPa and a ductility class C

Table 4.3: Cubic compression tests results [18]

Cube	f_c (2 days)	f_c (7 days)	f_c (28 days)
[No.]	[MPa]	[MPa]	[MPa]
1	34.22	42.33	45.78
2	34.79	43.70	46.22

Grout

Referring to [17], it is possible to conclude that the grout is self-compacting and presents a high mechanical resistance and controlled shrinkage. Hence, the optimized mixture was maintained as defined in [17], as presented in Table 4.4.

Table 4.4: Grout's composition [17]

Matrix Composition		
Portland Cement Type I Class 42,5R	-	1536 [kg/m^3]
Silica fume	2 %	31 [kg/m^3]
Water-binder ratio	0.30	470 [kg/m^3]
Super-plasticizers: *SikaViscoCrete 3005*	0.5 %	8 [kg/m^3]
Total		2045 [kg/m^3]

Furthermore, in order to define the mechanical properties of the grout, 6 specimens were tested in laboratory conditions according to the NP EN 206-1 [20]. These tests were conducted in the Department of Civil Engineering of the Faculdade de Ciências e Tecnologia - UNL and are illustrated in Figure 4.3.

(a) Bending test
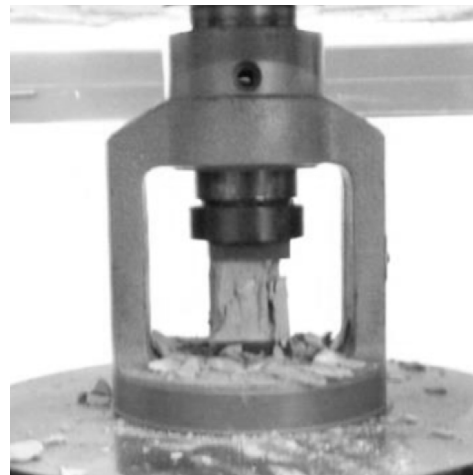
(b) Compression test

Figure 4.3: Grout laboratory tests [18]

The force-displacement values recorded during the bending tests, provided by the author of [18], are presented in Figure 4.4, in which it is observable that the curve obtained with specimen 3 presents only one stage, while the remaining

curves present two stages. Hence, the results obtained with specimen 3 can not be considered in the analysis due to the difference between this curve and all the others. The first stage of the remaining curves, more horizontal than the final stage, will not be considered in the grout's behaviour calibration because it is a result of the accommodation of the testing machine to the specimen.
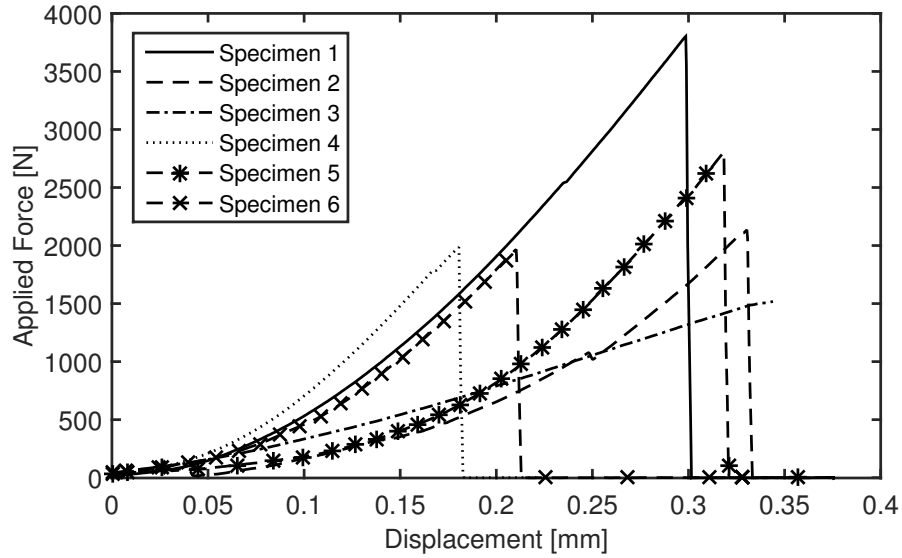
Figure 4.4: Force-displacement curves for bending tests

From the bending test, one can compute the maximum tension present at the mid-span of the specimen as:

$$f_{ct,b} = \frac{3}{2} \frac{N_{a,b}\, l}{b\, h^2}$$ (4.1)

where $f_{ct,b}$ is the experimental failure tension due to bending, $N_{a,b}$ is the perpendicular applied force to the specimen's surface, l is the used span (100 mm), b is the specimen's width (40 mm) and h is the specimen's height (40 mm).

For the compression test, the failure compression stress is calculated through the following equation:

$$f_c = \frac{N_a}{A}$$ (4.2)

where N_a is the applied force and A is the specimen's area (40x40 mm^2). Through the previous equations, the average failure stresses ($f_{ctm,b}$ and f_{cm}) were calculated, and presented in Table 4.5.

In experimental model B, which was obtained through the application of the strengthening type B onto the bottom surface of the reference model, the UFRG was 20 mm thick with its fibres placed in the span's direction, as seen in Figure 4.5.

Table 4.5: Grout's bending and compression tests' results

Spec.	$N_{a,b}$	$f_{ct,b}$	$f_{ctm,b}$	N_a	f_c	f_{cm}
[No.]	[N]	[MPa]	[MPa]	[kN]	[MPa]	[MPa]
1	3802.52	8.91		132.00	82.50	
2	2135.75	5.01		118.00	73.75	
3	2214.85	5.19	5.82	136.00	85.00	78.75
4	1984.87	4.65		108.00	67.50	
5	2806.01	6.58		161.00	100.63	
6	1966.57	4.61		101.00	63.13	
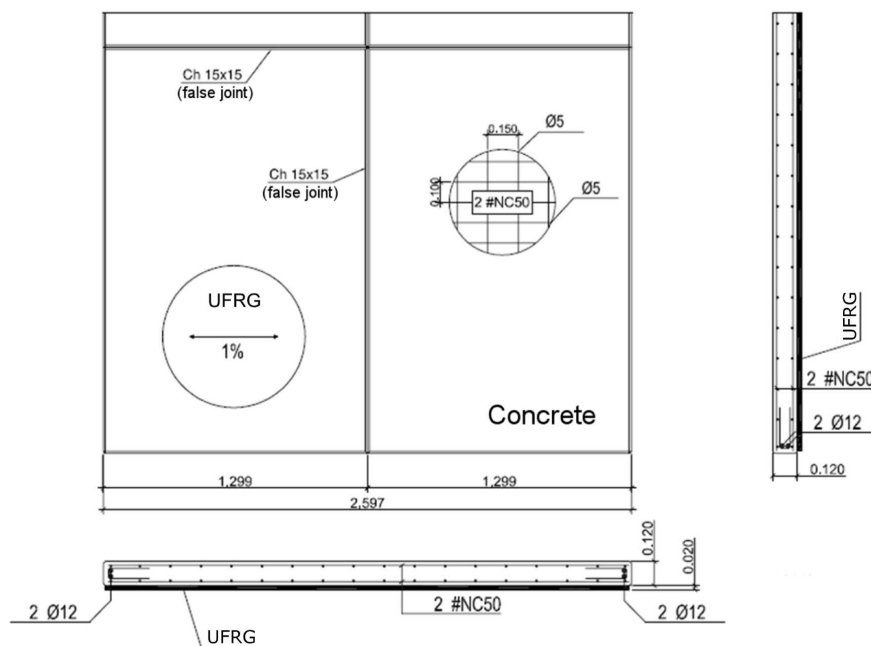
Figure 4.5: Reinforced experimental model detailing (Model B) [18]

4.2   Experimental models subjected to blast loads

The experimental models defined in the previous section were tested against explosion effects in the military camp situated in *Santa Margarida*, Portugal. The transportation, storage and handling of the explosive materials were made by the military, according to the rules and safety procedures approved by the Portuguese Army.

4.2.1   Experimental set-up

As reviewed, the original façade panels were cut in order to create four experimental models, which were tested as slabs. For each test, 4 inverted T beams with a height of 0.3 m and a length of 1.65 m were used to obtain a simply supported slab with a clear span of 2.3 m. When positioned in place, the UFRG was

placed on the underside of the slab in order to increase its resistance to bending.

The explosive charges were suspended above the slab, aligned with its centre. The suspension was obtained through a supporting device with a cantilever beam, as observed in Figures 4.6, 4.7(b) and 4.9. The distance between the charge and the slab was measured by supporting the charge on the slab and then, while lifting the charge to its final position, measuring the amount of rope used to lift it. After the positioning of the charge, in order to prevent changes in its position, three ropes were attached to it and fixed to the ground.
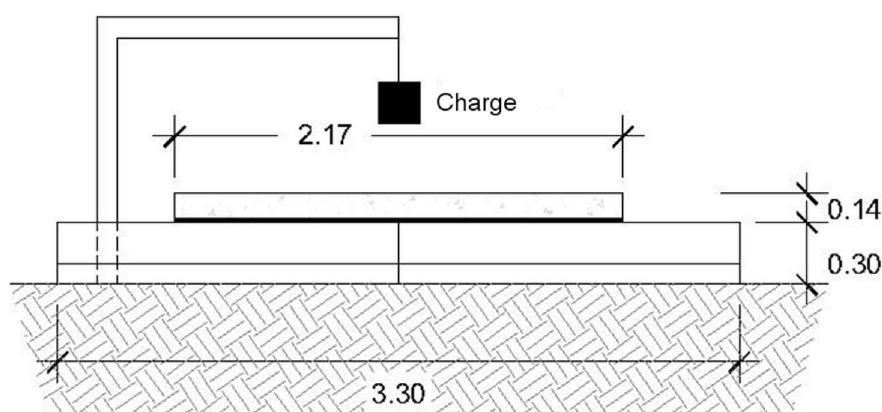
Figure 4.6: Lateral view of the experimental set-up [18]

With this set-up, the explosive was detonated in the air and there was no obstacle between the charge and the slab. Therefore, the slab was subjected to a free-air burst, which is characterized by a shock wave that suffers no amplification, as described in Section 2.1.2.

The explosive material was TNT, in the form of charges for military use. These charges, with a weight of 1 kg, have the shape of a rectangular prism. Hence, in order to obtain a higher mass, the charges are joined together with tape, always resulting in a prismatic shape, as illustrated in Figure 4.7(a). Additionally, in Figure 4.7(b) one can observe the explosive charge in its final position above the slab.

Hence, the controlled parameters that influence the shock wave generated by the explosion of the charge are:

- Weight of the explosive charge, W_{TNT};

- Distance between the centre of the charge and the slab's surface, R.

The objective of the experimental tests was the study of the resistance of reinforced slabs under the effect of loads resulting from an explosion. Therefore, all the experimental models must be subjected to the same load in order to obtain comparable results. However, the load must be sufficient to generate visible

(a) Explosive charge   (b) Explosive charge in its final position
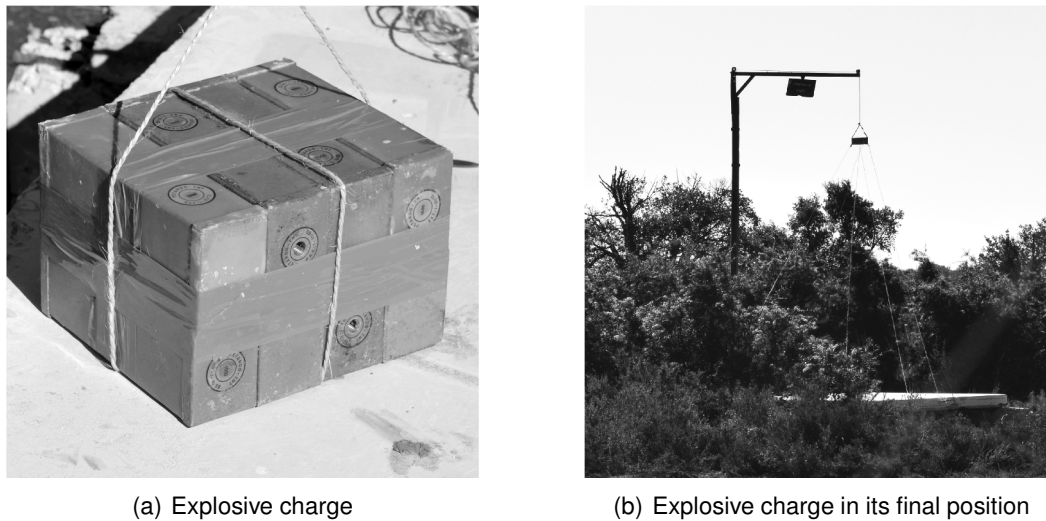
Figure 4.7: Experimental field test

damage to the slabs but, simultaneously, must not create excessive damage or collapse of the slab since this would make the results' comparison impossible. Additionally, in order to allow a better comparison, one of the slabs was tested without strengthening.

Due to the differences between the maximum displacement values obtained in Section 2.4, preliminary tests were performed in order to configure the test system and adjust the blast loads subjected to the slabs. This resulted in a total of 4 tests, the first two being for configuration, while the last two were used to assess the slab's resistance. In Table 4.6 one can observe the TNT weight and charge's distance used in the tests. Note that the presented distance is the distance between the lower surface of the charge and the slab's upper surface, which corresponds directly to the measured distance.

Table 4.6: Experimental tests' set-up

Test No.	Slab	TNT Weight [kg]	Distance [m]	Objective
1	Model C	2	3	Set-up
2	Model C	8	2	Set-up
3	Model B	8	3	Experimental Test
4	Reference	8	3	Experimental Test

Monitoring system

In order to compare the results of the performed tests, a monitoring system is required. In these tests, the monitoring system aimed to measure the maximum and the residual deformations.

A centred 2 m rule and a tape measurer were used to determine the

residual deformation after the experiments, as illustrated in Figure 4.8. For the maximum deformation, 24 rods, 200 mm long were pinned into three polystyrene plates, allowing measurements up to 150 mm. The definition of the maximum displacement monitoring system is depicted in Figure 4.9.

Figure 4.8: Residual deformation's measurement
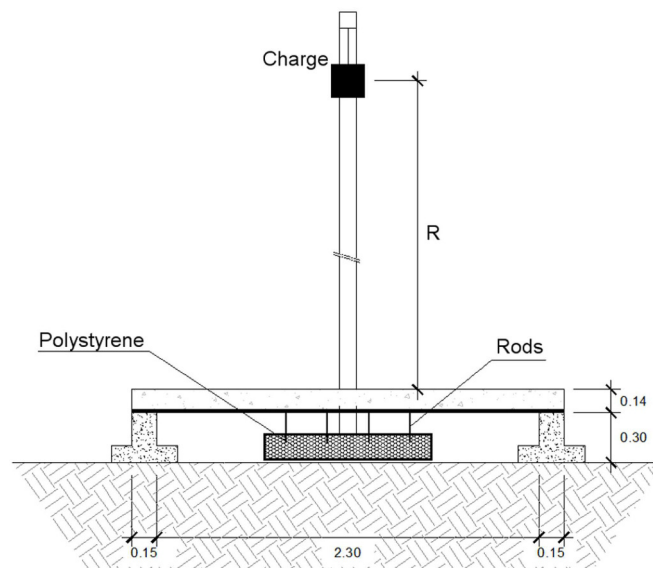
Figure 4.9: Maximum deformation's monitoring system [18]

Due to the uneven ground, special care was ensured in the setting of the monitoring system in order to achieve a reasonable precision. Hence, the assembly was executed as follows: initially, the rods were pinned into the polystyrene plates with a maximum depth of 30 mm; then, the slab was lowered to its final position, which drove the rods deeper into the polysteryne plate, allowing to record the distance between it and the slab; afterwards, the slab was lifted in order to mark the rods' depth; at last, the slab was placed in its final position and subjected to the blast effects, which drove the rods even deeper into the polysteryne. Through the measuring of the distance between the previously marked depth and the new depth of the rods, it is possible to obtain the maximum deformation of the slab. In

Figure 4.10 it is possible to observe the lifted slab to mark the rods' position and the slab in its final position with the mounted monitoring system.

(a) Monitoring system preparation   (b) Slab's final position
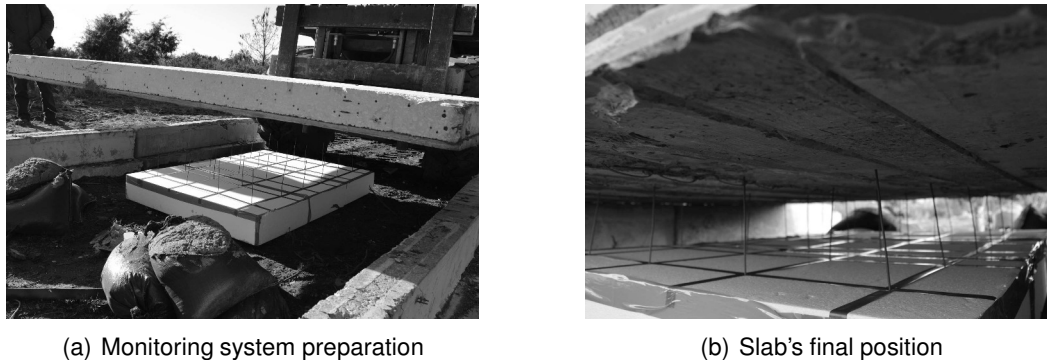
Figure 4.10: Maximum deformation's monitoring system setting

4.2.2   Experimental results

As represented in Table 4.6, the first two tests were performed to configure the test system. Thus, the monitoring system was only used in the last two. Furthermore, in the results' photographs presented, one should note that the principal cracks were highlighted in black to allow a better visualization.

Test No. 1

In Test No. 1, an explosive charge with 2 kg was used, at a distance of 3.0 m from the upper surface of the slab with type C reinforcement (model C). However, this test caused no significant damage or residual deformation to the experimental model. Additionally, in Figure 4.11, it is possible to observe a 2 frame photo sequence of the 2 kg TNT detonation used for the purpose of this test.

Test No. 2

From results of Test No. 1, it was possible to conclude that the explosion's strength was too low. Hence, it was necessary to increase it in order to obtain significant damage or residual deformation. This need led to the use of a 8 kg charge for Test No. 2, at a distance of 2.0 m from the upper surface of the slab with type C reinforcement (model C). One can observe a 2 frame photo sequence of the 8 kg TNT detonation used in this test in Figure 4.12. Moreover, through the comparison of Figures 4.11 and 4.12, it is visible the higher energy released by the 8 kg TNT detonation.

This test led to the collapse of the experimental model, with the failure of the mid-span section due to bending. One can verify, through the analysis of Figure 4.13(a), that the concrete, the reinforced steel mesh and the FRG failed. Additionally, in Figure 4.13(b), one can observe that the edge's reinforcement bars

(a) Frame 1

(b) Frame 2

Figure 4.11: Photo sequence of a 2 kg TNT detonation

(a) Frame 1

(b) Frame 2

Figure 4.12: Photo sequence of an 8 kg TNT detonation

did not fail and that the collapse happened due to compressive forces on the upper face, that led to concrete's crushing.

(a) Experimental model C collapse   (b) Concrete's crushing
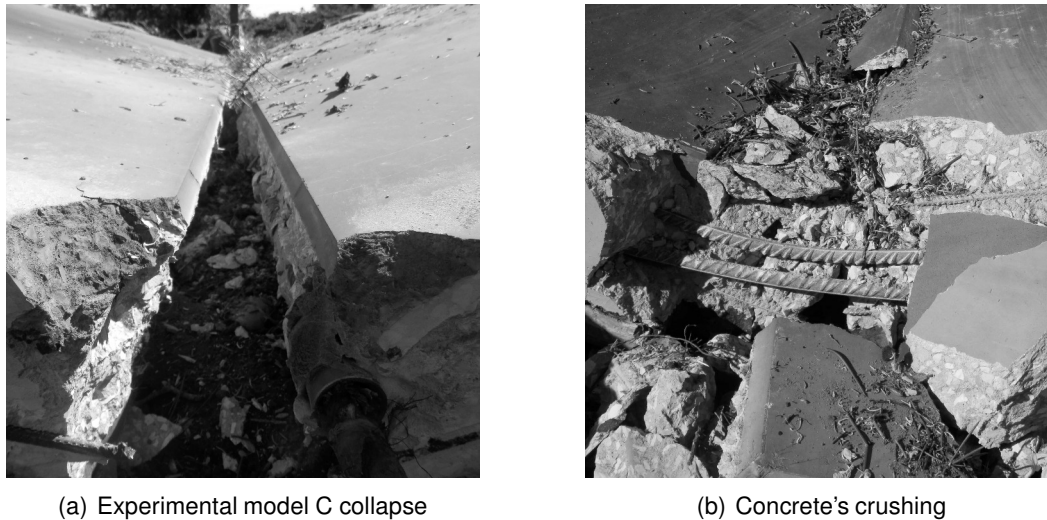
Figure 4.13: Experimental model C after Test No. 2

Test No. 3

The experimental set-up was assumed as ideal in Test No. 3, leading to the assembly of the monitoring system. As presented in Table 4.6, Test No. 3 resorts to a 8 kg charge at a distance of 3.0 m from the upper face of the slab with reinforcement type B (model B). After the loading, the presence of a residual deformation and cracking in the bottom surface at mid-span due to bending were verified. The resulting cracking is mainly characterized by a wider crack, as seen in Figure 4.14(b), which had a width ranging between 1.3 and 2.5 mm along its length. Additionally, as observed in Figure 4.14(a), there was some minor cracking in the upper face and some damage due to the impact of fragments.

During the explosion, the shock wave damaged the maximum deformation's monitoring system. However, the central zone of the monitoring system is considered reliable. The results for the maximum and residual deformation obtained with the monitoring systems are depicted in Table 4.7.

Table 4.7: Test No. 3 deformations [18]

Max. deformation	Max. deformation average	Residual deformation
[mm]	[mm]	[mm]
37.0		
32.5	33.5	10.0
32.5		
32.0		

(a) Experimental model B upper face

(b) Mid-span crack
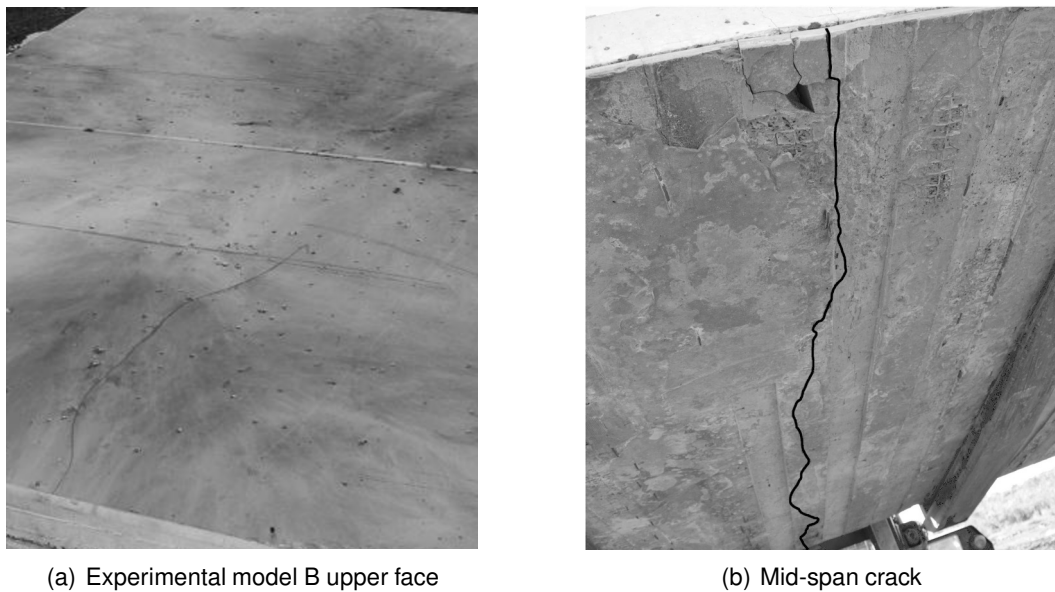
Figure 4.14: Experimental model B after Test No. 3

Test No. 4

In order to compare the resistance between the slab with the reinforcement type B and the reference slab, the same set-up was used in Tests No. 3 and 4. This led to similar results in both tests, such as the residual deformation, visible in Figure 4.15(a), and the mid-span cracking, illustrated in Figure 4.15(b). However, in Test No. 4, the crack's width varies between 2 and 3 mm along its length, which are greater than the obtained in Test No. 3.

(a) Reference model's residual deformation

(b) Mid-span crack
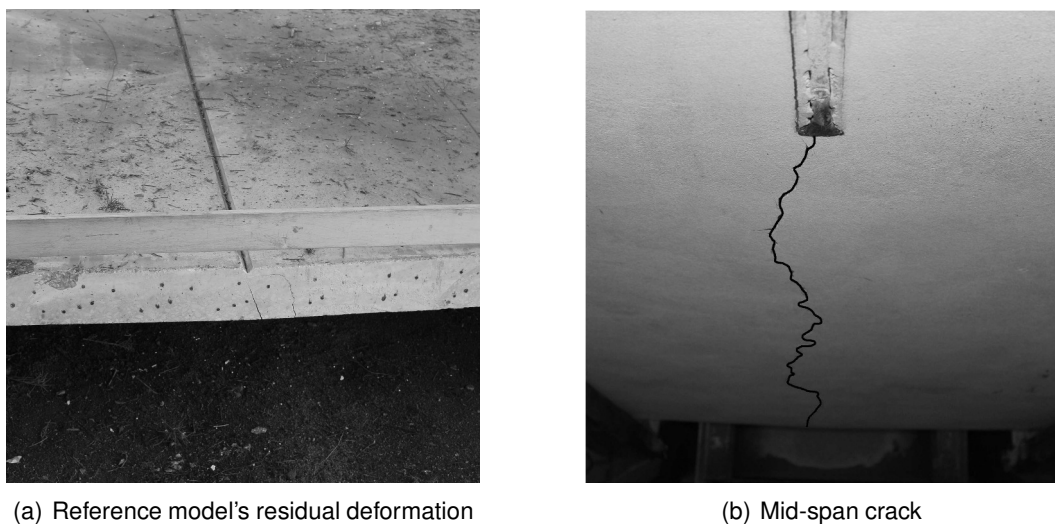
Figure 4.15: Reference model after Test No. 4

Due to the damage of the monitoring system, which occurred during Test No.

3, only one polystyrene plate with four rods was used to monitor the maximum deformation in Test No. 4, as can observed in Figure 4.16. Moreover, in Table 4.8, the deformations of the reference slab, which were measured by the monitoring system, are represented.

Figure 4.16: Maximum deformation's measurement in Test No. 4

Table 4.8: Test No. 4 deformations [18]

Max. deformation	Max. deformation average	Residual deformation
[mm]	[mm]	[mm]
65.0		
70.0	65.0	20.0
60.0		
65.0		

From Table 4.8, one can observe that the resultant maximum displacement had a value of 65 mm. Additionally, if one compares this value with the maximum displacement values obtained in Section 2.4, one can conclude that the Kinney and Graham and Rankine-Huginiot formulation led to a more precise value, when compared with experimental value, with a difference of 66 %, which is considered as acceptable due to the simplicity of the computational model.

4.3   Numerical model

The numerical model of the slabs was developed with the commercial software *Extreme Loading for Structures* (ELS) v3.1 [15], which resorts to the Applied Element Method, as reviewed in Chapter 3. Throughout the numerical model's development, the following steps were executed:

- Creation of the initial model, based on the project and the experimental set-up, as observed in Figures 4.2 and 4.6;

- Calibration of the initial model based on the experimental results obtained in Test No. 4;

- Implementation of the experimental model B in the ELS, taking into account the calibration performed in the previous item;

- Draw conclusions through the analysis of the obtained results.

4.3.1 Material calibration

The ELS has the capacity to simulate the non-linear behaviour of the model's materials, as illustrated in Figures 3.6 and 3.10. However, one must calibrate the previous models to ensure a correct structural simulation.

Concrete

Due to the lack of experimental tests performed for the concrete, except for the experimental mean compressive strength (f_{cm}), the values defined in the Eurocode 2 [21] for the mean secant modulus of elasticity (E_{cm}), the mean tensile strength (f_{ctm}), the strain at maximum compression stress (ε_{c1}) and the ultimate compression strain (ε_{cu1}) will be considered. In Table 4.9, one can observe the concrete properties implemented in the ELS.

Table 4.9: Concrete properties implemented in the ELS

Units	E_{cm}	f_{cm}	f_{ctm}	ε_{c1}	ε_{cu1}
S.I. [MPa]	33000	46.33	2.90	2.2 [‰]	3.5 [‰]
ELS [tonf/m^2]	3.70935x10^6	5207.70	325.97		

The cube used for the determination of the compressive strength of concrete cubes has a 15 cm edge, as defined in [20]. Hence, in order to simulate the laboratory test, a 15 cm cube was modelled in the ELS, as represented in Figure 4.17. The upper and lower plates were modelled as a High Strength Steel to reduce their influence in the numerical simulation. Additionally, taking into account that the 3D formulation of the AEM does not consider the Poisson's ratio effect, there is no need to extend the plates' size since the cube's radial deformations remain null throughout the simulation.

Considering that the cubic model illustrated in Figure 4.17 has the properties depicted in Table 4.9, one can obtain the stress-strain curve represented in Figure 4.18. Through the analysis of this figure, one can conclude that the obtained solution can accurately simulate the concrete's compression behaviour until collapse. Additionally, it is possible to observe that the failure compression stress obtained through the numerical simulation corresponds to the stress obtained through laboratory tests.
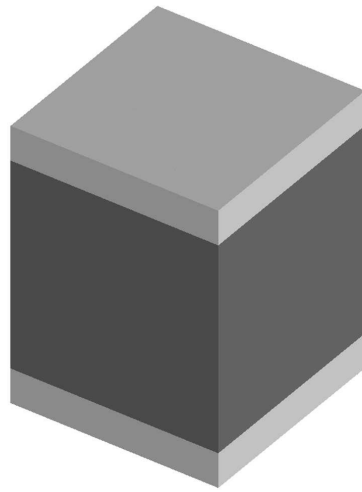
Figure 4.17: ELS model for the concrete compression test
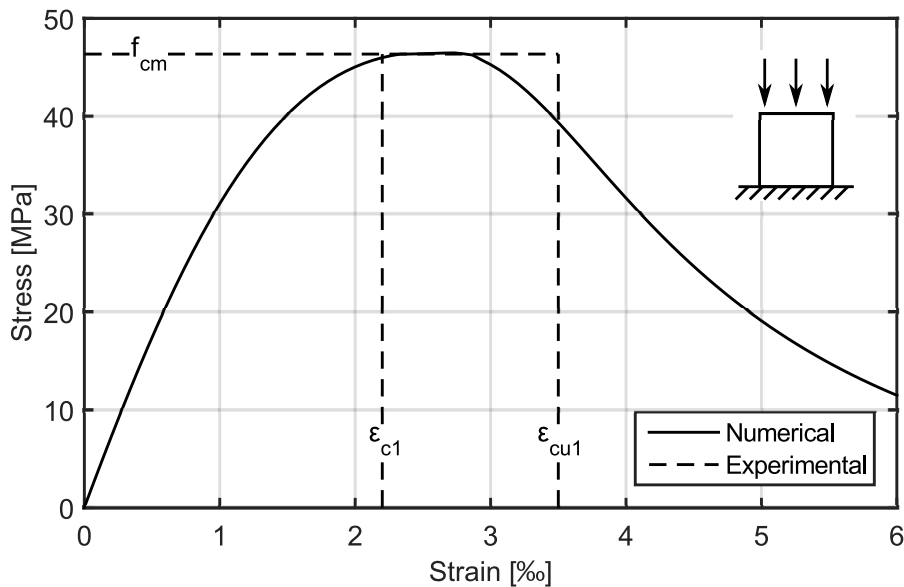
Figure 4.18: Stress-strain relation for concrete

Reinforcement bars

In order to calibrate the A500 ER and A500 NR-SD steel's behaviour, which was assumed to the same, an ELS model was created. The model consists of a 0.25 m long $\phi 6$ reinforcement bar divided into 150 parts in the longitudinal direction and 10 parts in each radial direction, resulting in 13200 elements, which ensures the model's convergence. Figure 4.19 illustrates the division of a quarter section of the steel reinforcement bar into elements implemented in the ELS. One should note that in Figure 4.19 only a quarter section was represented in order to allow a better visualisation of the section's division into elements, although the whole section was modelled in the ELS. The calibration was based on the traction test

results presented in [39] for a A500ER $\phi 6$ reinforcement bar, as illustrated in Figure 4.20. As reviewed in Section 3.3.2, the AEM resorts to the Ristic's steel model to simulate the reinforcement bar's behaviour, which is characterized by the following parameters:

- Young's modulus (E);

- Shear modulus (G);

- Tensile Yield stress (f_y);

- Ultimate strength / Tensile Yield stress (f_u/f_y);

- Ultimate strain (ε_u);

- Post Yield Stiffness ratio (E_1/E).
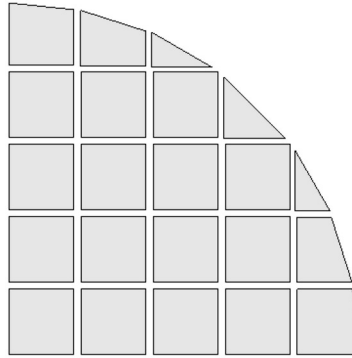
Figure 4.19: Division into elements of the reinforcement bar's quarter section

Through the calibration of the previous parameters to the experimental results, one can define the Ristic's constitutive model parameters as presented in Table 4.10. The calibration was performed iteratively through a sensitivity analysis, beginning with the values defined by the Eurocode 2 [21] for a A500 ER steel. Based on the differences between the results, a series of iterative changes were performed to all the parameters, except to the Young's and Shear Modulus, until a good approximation to the experimental result was obtained.

Table 4.10: A500 ER properties implemented in the ELS

Units	E	G	f_y	ε_u	f_u/f_y	E_1/E
I.S. [MPa]	200000	76923	600	13.50 [%]	1.19 [-]	0.011 [-]
ELS [tonf/m^2]	2.24809x10^7	8.64650x10^6	67442.68			

Grout

The Maekawa's concrete model [36] was considered to be accurate in the simulation of the grout's behaviour. Therefore, one must calibrate the parameters
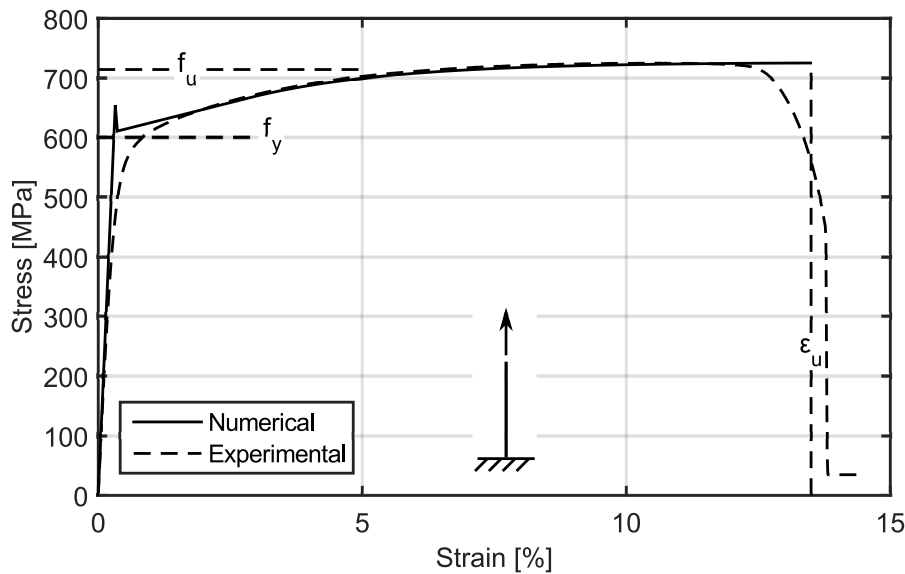
Figure 4.20: Stress-strain relation for steel [39]

required by the model in order to implement the grout's correct properties into the ELS. Through the performed compression tests, one can obtain the grout's failure compression stress (f_{cm}) to be implemented in the ELS as presented in Table 4.12.

Additionally, the flexural test results are required for the definition of the mean secant modulus of elasticity (E) and the mean tensile strength ($f_{ctm,b}$) of the grout. As observed in Figure 4.4, all the experimental curves exhibit two phases. However, as already indicated, only the last phase will be considered for the following calibration. In order to obtain an average force-displacement curve, a linear trend line must be obtained for each curve, as illustrated in Figures 4.21(a) through 4.21(e). Afterwards, an average curve is obtained through the calculation of the mean slope and mean maximum displacement, which conduct to the results depicted in Table 4.11 and represented in Figure 4.21(f).

Table 4.11: Slope of the force-displacement linear fit

Spec.	Slope	Mean slope	Max. disp.	Mean Max. disp.
[-]	[N/mm]	[N/mm]	[mm]	[mm]
1	18123.02		0.2055	
2	14038.34		0.1509	
4	16071.90	15974.59	0.1230	0.1543
5	17366.88		0.1583	
6	14272.83		0.1340	

Considering the flexural test represented in Figure 4.3(a), one can obtain the shear force and bending moment diagrams as illustrated in Figure 4.22.

Due to the specimens' short span, only 100 mm, one must compute the mid-span displacement with the Unit-Load Theorem considering both the bending moment

(a) Specimen 1

(b) Specimen 2

(c) Specimen 4

(d) Specimen 5

(e) Specimen 6

(f) Average curve determination
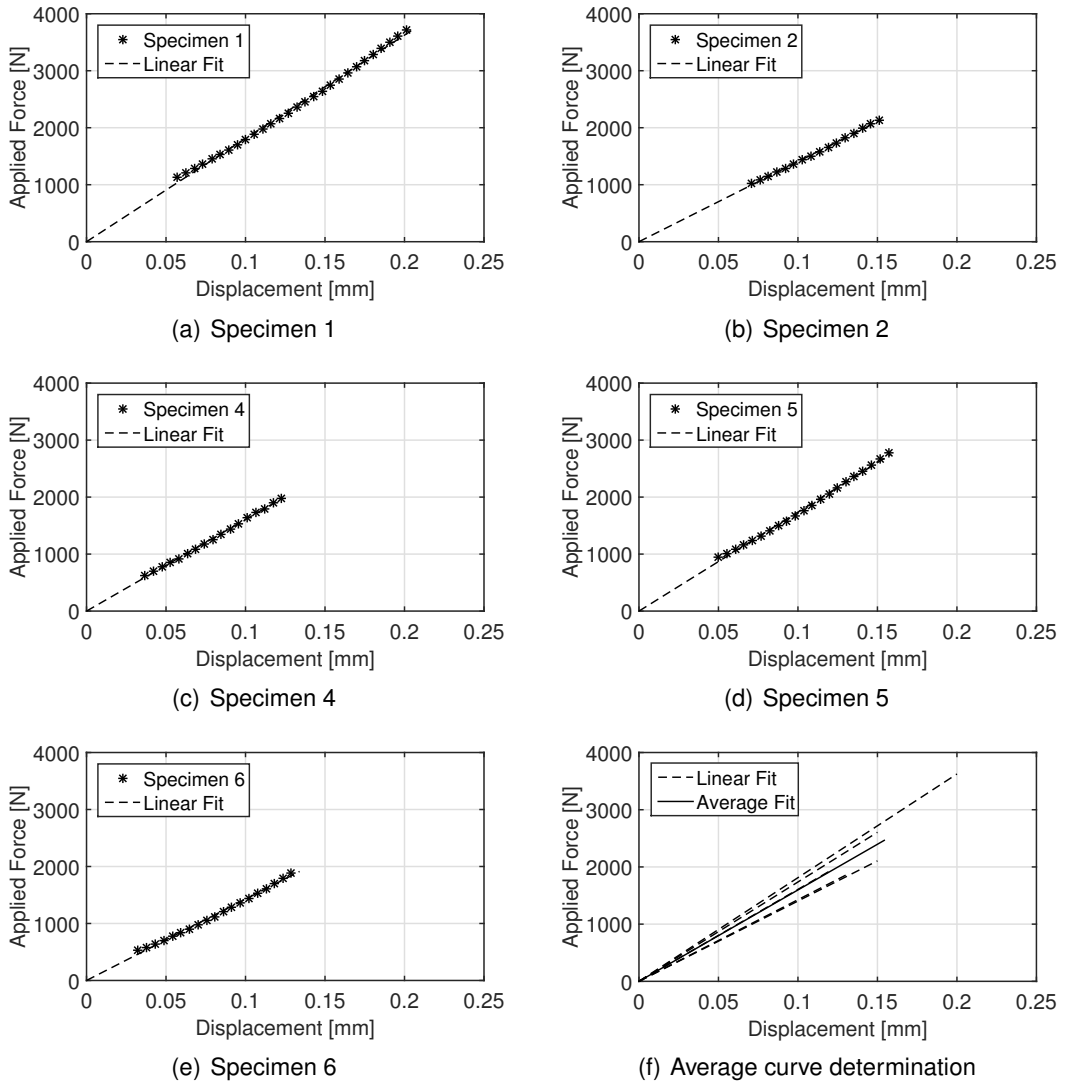
Figure 4.21: Grout laboratory tests
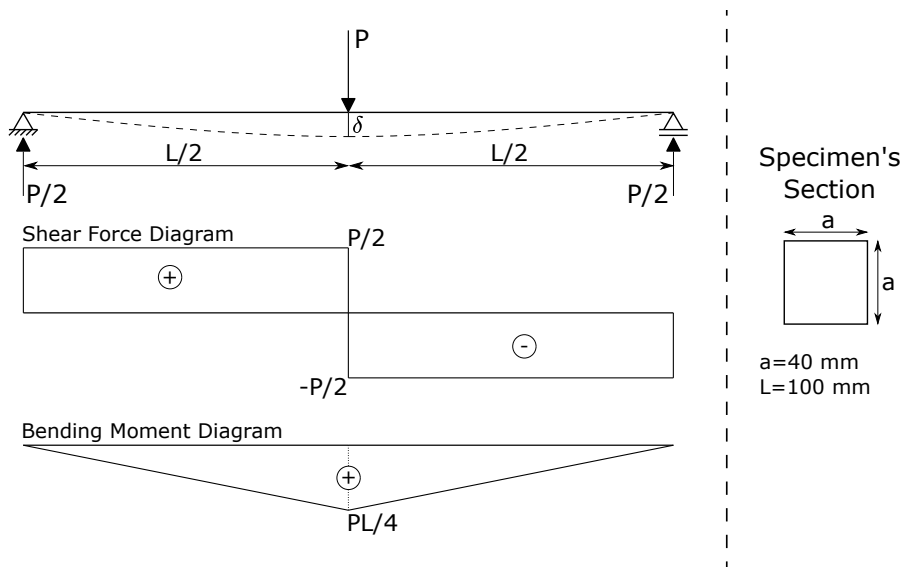
Figure 4.22: Shear force and bending moment diagrams for grout's bending test

and the shear force influence, as depicted in equation (4.3).

$$
\begin{aligned}
1 \times \delta = \int \frac{M\bar{M}}{EI} + \frac{V\bar{V}}{GA^*}\mathrm{d}x = \\
= 2\left[\frac{1}{3EI}\frac{PL}{4}\frac{L}{4}\frac{L}{2} + \frac{1}{GA^*}\frac{P}{2}\frac{1}{2}\frac{L}{2}\right] = \\
= \frac{PL^3}{48EI} + \frac{PL}{4GA^*}
\end{aligned}
\tag{4.3}
$$

where P is the applied force to the specimen, L is the specimens' length, I is the second moment of area and A^* is the shear area of the section. Through the mean slope obtained in Table 4.11 and equation (4.3), it is possible to calculate the theoretical mean secant modulus of elasticity of the grout as follows:

$$
15974.59 = \frac{P}{\delta} \Leftrightarrow 15974.59 = \frac{P}{\left(\frac{PL^3}{48EI} + \frac{PL}{4GA^*}\right)}
\tag{4.4}
$$

Solving equation (4.4), one obtains the grout's mean secant modulus of elasticity:

$$
E = 2278.88 \text{ [N/mm}^2\text{]}
\tag{4.5}
$$

Lastly, referring to Table 4.5, one can define mean tensile strength, $f_{ctm,b}$, as presented in Table 4.12.

After the definition of the previous parameters, the behaviour of the grout can be implemented in the ELS model using 80x8x20 = 12800 elements. This model, see Figure 4.23, has the specimens' geometry, as defined in [20], i.e. a rectangular prism 160 mm long with a 40 by 40 mm section, simply supported with a 100 mm clear span. The grout's implemented parameters in the ELS are depicted in

Table 4.12. Through the analysis of Figure 4.24, one can conclude that the grout's behaviour is calibrated, despite the greater stiffness when compared with the experimental curve. This slightly increased stiffness might be due to imperfect simulation of the boundary conditions (friction).

Figure 4.23: ELS implementation of the grout specimen's flexural test

Table 4.12: Grout properties implemented in the ELS

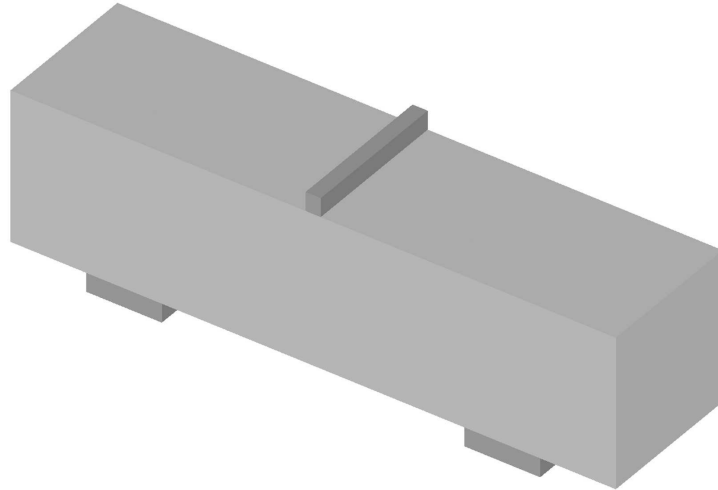| Units	E	G	f_{cm}	$f_{ctm,b}$
I.S. [MPa]	2278.88	949.53	78.75	5.82
ELS [tonf/m^2]	256156.30	106731.64	8851.85	654.19
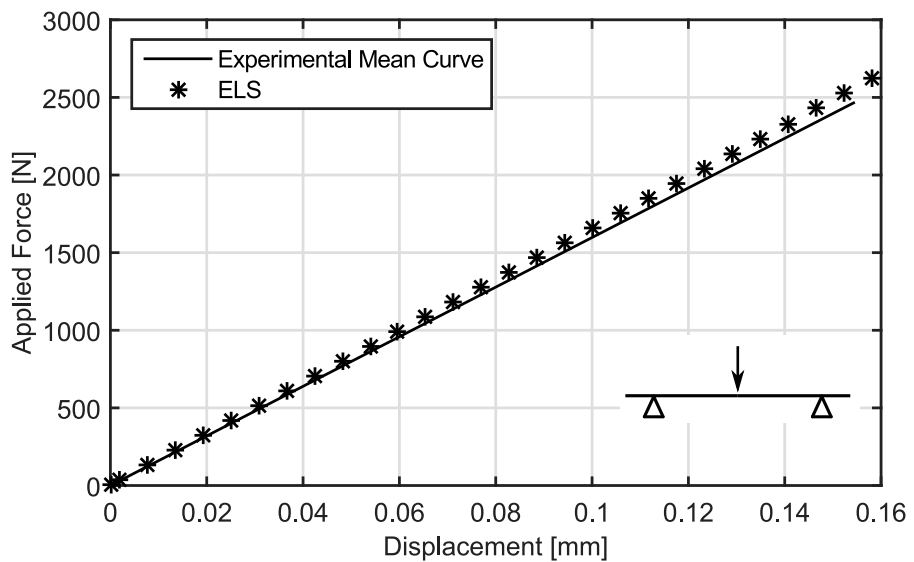
Figure 4.24: Force-displacement relation for grout

Steel fibres

The steel fibremat used in the present dissertation was provided by *Favir* [16] and produced from steel wires with a 3.1 mm diameter. The production process consists of a lamination procedure of the steel wire, resulting in a non-woven mat formed by filaments [17]. However, the numerical simulation of the steel fibremat's behaviour would be a very complicated process due to changes in the mechanical properties of the steel wires resulting from the lamination process, and to the fibremat's complex interaction with the grout. Therefore, conservatively, the fibremat will be simulated as a set of reinforcement bars with the mechanical properties of the steel wires.

In order to define the mechanical properties of the steel wires, three steel wires, 0.133 m long, were subjected to a tensile strength test, which resulted in the stress-strain curves depicted in Figure 4.25, which were provided by the author of [17]. Additionally, it is possible to observe in this figure the determined average stress-strain curve. Analysing this figure, one can define the main mechanical characteristics of a steel wire as presented in Table 4.13.
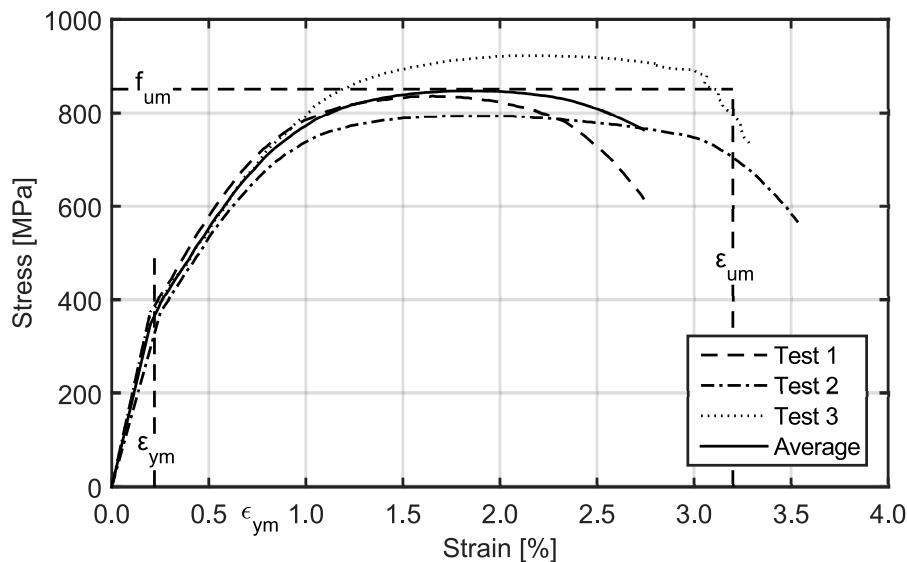
Figure 4.25: Experimental steel fibres' stress-strain curves

Table 4.13: Main mechanical characteristics of the steel wire [17]

Test	E	E_m	E_{1m}/E_m	f_u	f_{um}	ε_y	ε_{ym}	ε_u	ε_{um}
[No.]	[GPa]	[GPa]	[-]	[MPa]	[MPa]	[%]	[%]	[%]	[%]
1	188.54			836.02		0.20		2.7	
2	148.89	174.97	0.37	793.62	850.59	0.25	0.22	3.5	3.2
3	187.47			922.14		0.20		3.3	

Resorting to the numerical model used to simulate the reinforcement bar's behaviour, and correcting its length and diameter to 0.133 m and 3.1 mm,

respectively, one can simulate the steel wires's behaviour through the implementation of its mechanical characteristics into the numerical model. However, it is possible to conclude, through the observation of the initial model's stress-strain curve represented in Figure 4.26, that a calibration is necessary. Additionally, one can observe that there is no relaxation after the elastic phase in the numerical stress-strain curve, as observable in the experimental curves. Through the comparison between the strain energy of the numerical and experimental curves, one can verify the calibration of the numerical solution. For this case, if one compares the strain energy obtained with the average curve resulting from the experimental tests and the calibrated curve represented in Figure 4.26, one obtains a difference of 3.28 %, which is considered reasonable. Hence, one can consider that the calibrated stress-strain curve, obtained with the properties presented in Table 4.14, simulates the steel wire's behaviour with reasonable accuracy.
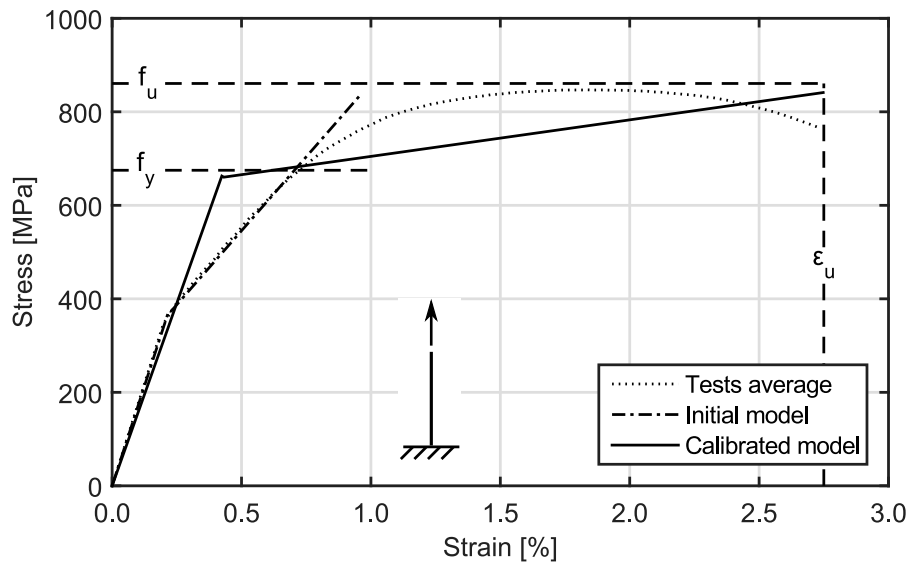
Figure 4.26: Calibration of the steel fibres' stress-strain curve

Table 4.14: Steel wire properties implemented in the ELS

Units	E	G	f_y	ε_u	f_u/f_y	E_1/E
I.S. [MPa]	160000	61538.46	675.00	2.75 [%]	1.275 [-]	0.05 [-]
ELS [tonf/m^2]	1.79847x10^7	6.91720x10^6	75873.02			

4.3.2 Numerical model geometry

The numerical model was created accordingly to the project, which is illustrated in Figure 4.2. However, in order to allow a better understanding of the created model, the present description will be reviewed in four parts:

- Slab;

- Supports;

- Reinforcement;

- Boundary conditions.

Slab

The slab's concrete, represented in Figure 4.27, was modelled with 8 node elements to simulate the slab's geometry, which is 2.60 by 2.17 m and 0.12 m thick. After a mesh sensitivity analysis, presented in Section 4.3.3, the resulting mesh to be implemented in the ELS is composed of 86x45x4 = 15480 regular elements with approximately 0.03 m edges.
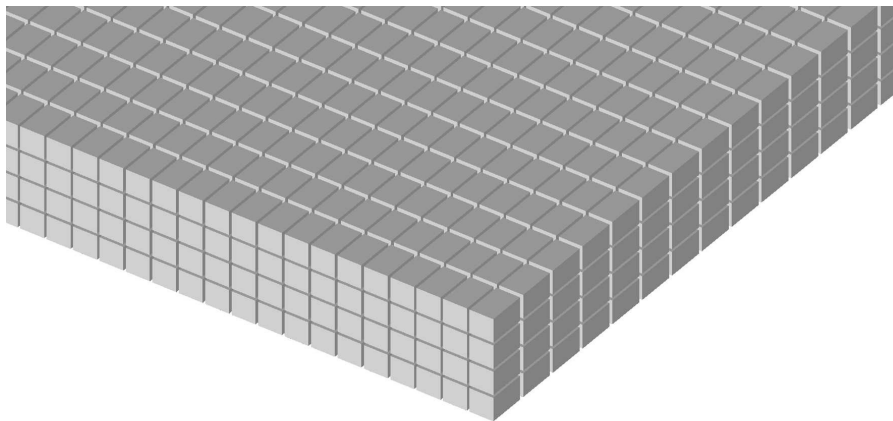
Figure 4.27: Slab geometry

Due to the use of 8 node elements, it was necessary to define the reinforcement bars separately. This definition was initially obtained using draft lines. Afterwards, the ELS allows their conversion to reinforcement bars with the properties defined by the user, i.e. their area and material properties. In Figure 4.28, one can observe the reinforcement bars' implementation in the ELS. Note the additional 2 U shaped $\phi12$ reinforcement bars presented in the referred figure. These additional bars are only present on three sides of the slab, as reviewed in Section 4.1.1.

Supports

Taking into account the experimental results, obtained with the monitoring system and presented in Section 4.2.2, and the lack of influence of the air beneath the slab in the numerical simulation, the final height of the supports was modelled with 15 cm, in order to reduce the number of elements used. This assumption led to a geometry of 0.15x0.15x2.17 m, which was modelled with 8 node elements, as depicted in Figure 4.29. To ensure a better connection between the slab and the supports, the same number of elements was used in the supports' longitudinal direction, resulting in a model with 5x5x45 = 1125 elements. The
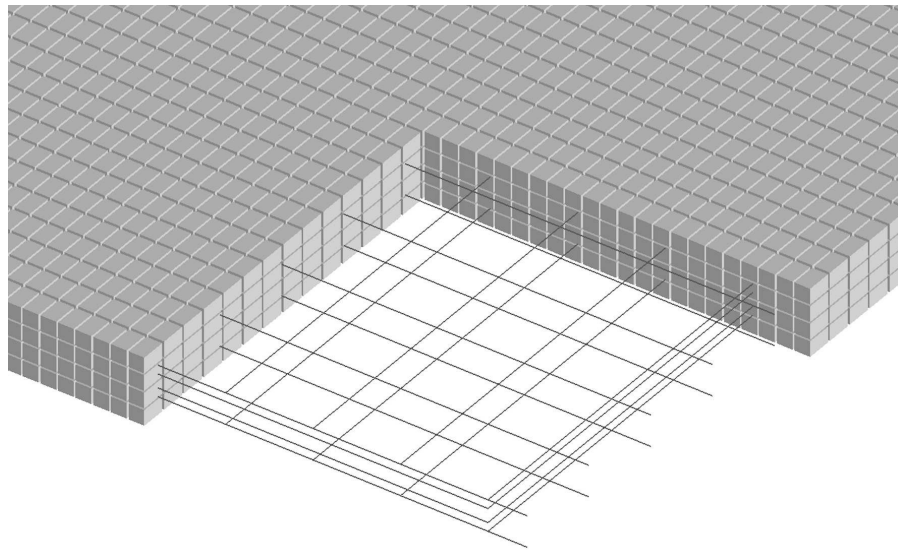
Figure 4.28: Reinforcement bars' implementation

material considered for the supports was the High Strength Concrete defined in the commercial software ELS. This consideration was based on the material that constitutes the supports used in the experimental tests.
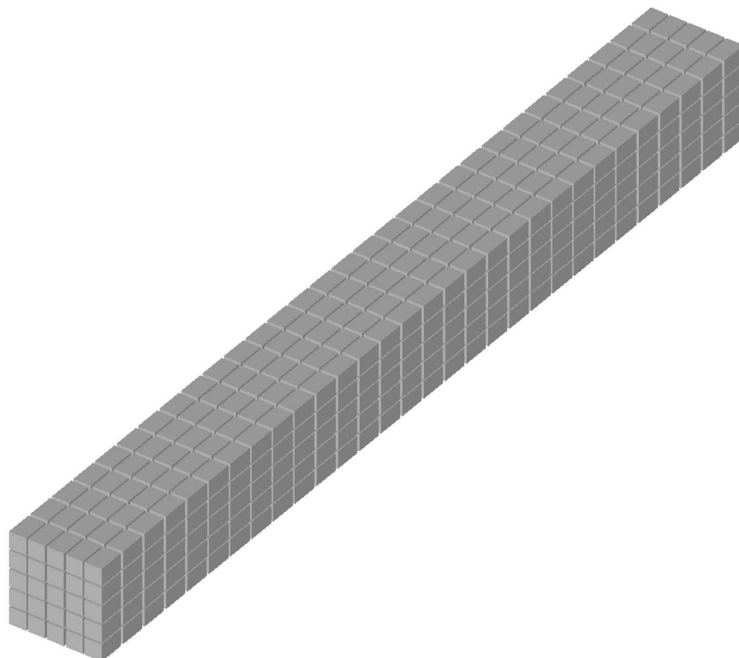
Figure 4.29: Supports' geometry and mesh

Strengthening

Taking into account the project depicted in Figure 4.5, one can define the thickness of the strengthening fibre grout as 20 mm, while the remaining dimensions are equal to the slab's, and model it with 8 node elements. Thus, the same number of elements was considered in all directions except for height, for which only one element was considered, resulting in an object with 86x45x1 = 3870 elements, as illustrated in Figure 4.30. Note that, to achieve a better representation of the reinforcement mesh, part of the image of the slab was hidden in this figure.
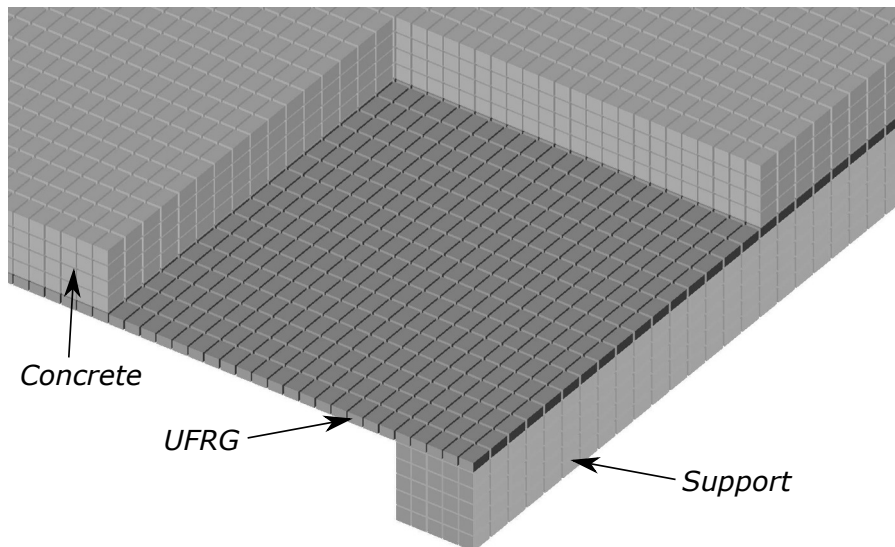
Figure 4.30: Geometry and mesh of the strengthening

In order to obtain a more correct simulation, the fibremat was modelled as a set of reinforcement bars placed in the fibres' direction. Each reinforcement bar has the length of the slab, i.e. 2.6 m. The reinforcement bars' set was achieved through the distribution of 25 bars in each row of elements, as represented in Figure 4.31.
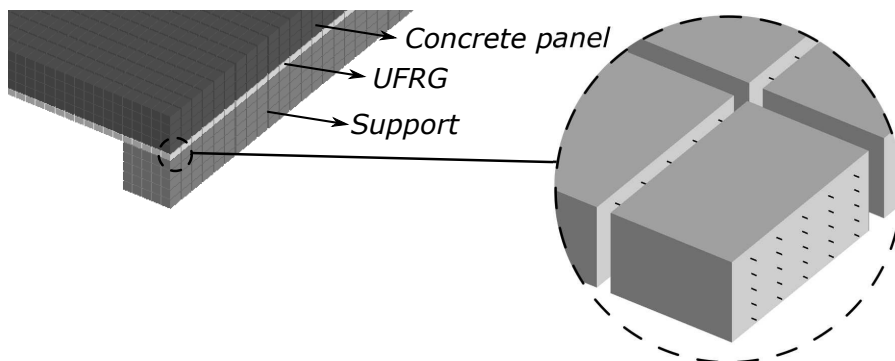
Figure 4.31: Reinforcement bars' distribution in reinforcement type B

The area of the reinforcement bars was defined through the following procedure. Firstly, one must determine the volume of the grout as:

$$V_t = 2.6 \times 2.17 \times 0.02 = 0.11 \text{ m}^3 \tag{4.6}$$

Afterwards, referring to the project, one verifies that in strengthening type B, the fibremat occupies 1 % of the grout's volume, which results in:

$$V_r = 1.13 \times 10^{-3} \text{ m}^3 \tag{4.7}$$

Next, it is possible to compute the total fibres' area in the span's direction for this reinforcement as:

$$A_t = \frac{V_r}{2.6} = 4.34 \times 10^{-4} \text{ m}^2 \tag{4.8}$$

Lastly, taking into account the number of reinforcement bars considered in the implementation of strengthening type B, one obtains the area of each reinforcement bar as:

$$A_{bar} = \frac{A_t}{45 \times 25} = 3.86 \times 10^{-7} \text{ m}^2 \tag{4.9}$$

Boundary conditions

In order to totally define the numerical model, one must define its boundary conditions. The base of the supports was considered to be fixed through the restraining of the bottom elements of the support. Additionally, one must define the characteristics of the interface between the supports and the slab. The interface material was considered to be a material with weak mechanical properties in order to correctly simulate the simply supported experimental model.

4.3.3 Convergence and sensitivity analysis

The calibration of the numerical model consists in the correction of some of its initial parameters to minimize the differences between the experimental and numerical results. In the present dissertation, the calibration of the numerical model were based on the experimental results obtained for the reference slab (Test No. 4), in particular, its residual displacement.

Mesh sensitivity analysis

The optimization of the numerical model is both related to the reliability and accuracy of the obtained results and to the computational effort and time of analysis necessary to obtain them. Therefore, the slab's numerical model was subjected to a mesh sensitivity analysis in order to ensure the numerical stability of the results, while maintaining a reasonable time of analysis.

The mesh sensitivity analysis of the slab was carried out through the application of a 50 kN force, statically applied in 1000 steps, equally distributed through all the elements of the slab. This value enables the study of the numerical stability throughout the whole structural behaviour of the slab because it guarantees its

collapse. During this process, the number of pairs of normal and shear connecting springs distributed along each common interface was constant, 5x5, while the number of elements in direction $N3$, defined in Figure 4.32, was successively increased and, in order to simplify the process, the number of elements used in the remaining directions was computed in order to maintain a cubic geometry in the slab's elements. Additionally, as previously stated, the number of elements used in the support's longitudinal direction was equal to the number of elements used in the slab's $N1$ direction.
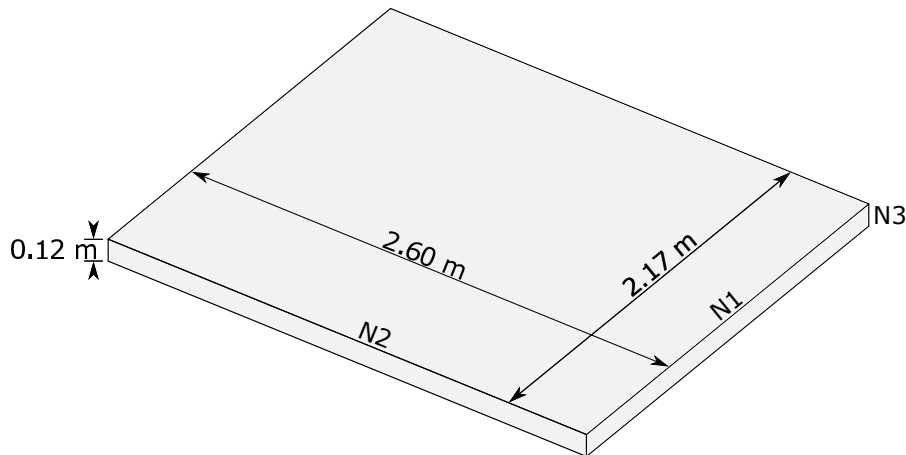
Figure 4.32: Mesh directions

In Table 4.15, one can observe the number of elements used in each direction, as well as the resultant number of elements used in the model of the slab for each mesh. Note that up to mesh No. 4, the number of elements in the $N3$ direction was successively increased.

Table 4.15: Mesh sensitivity analysis

Mesh No.	N1	N2	N3	No. of elements
1	18	21	1	378
2	36	43	2	3096
3	54	65	3	10530
4	72	86	4	24768
5	45	86	4	15480

Afterwards, the number of elements used in the $N1$ direction was decreased in mesh No. 5. This reduction, which allowed a reduction in the computation time, was based on the cylindrical bending of the slab and resulted in the force-displacement curve represented in Figure 4.33. Hence, through the analysis of Figure 4.33, one can conclude that mesh No. 5 leads to reliable and accurate results with reasonable computational effort and time of analysis.
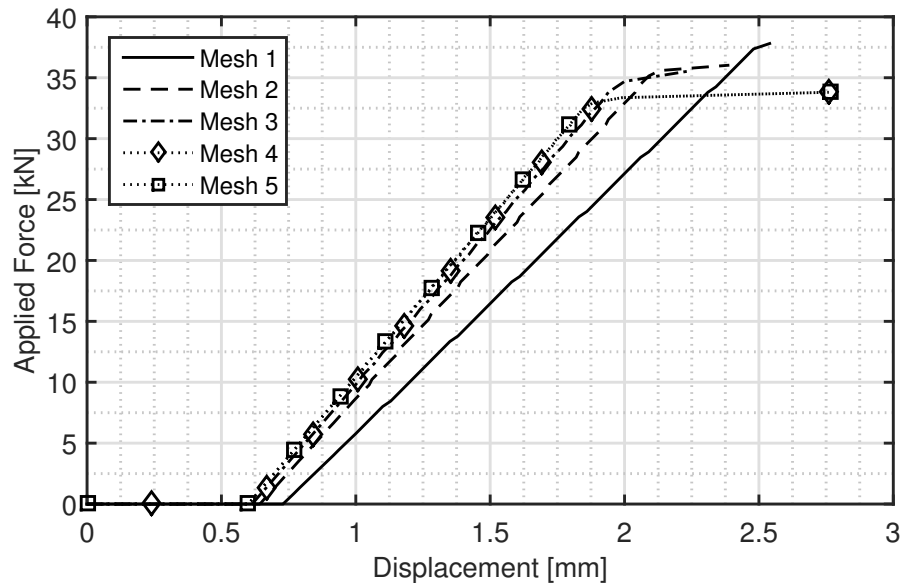
Figure 4.33: Mesh sensitivity analysis

Initial results

With the mesh sensitivity analysis complete and the determination of the mesh that conducts to reliable results in a reasonable time of analysis, the numerical model of the reference slab was subjected to the blast effects in the commercial software ELS, on an Intel Xeon CPU 5670 at 2.93 GHz with 16 GB of RAM.

Due to the nearly instantaneous rise of pressure that results from the charge's detonation, a very small analysis step is required to ensure a correct pressure-time loading simulation. The analysis time step used from the time of detonation until the overpressure on the exposed surface was null was 0.0001 s. After this phase, which is about 0.05 s, the analysis was performed for another 1.95 s, at a time step of 0.001 s, in order to study the post-blast behaviour of the structure. The time of analysis to calculate the 2450 time steps required was approximately 8-10 hours.

In order to calibrate the AEM and its prediction of the response of fibre reinforced RC panels when subjected to blast effects, the numerical model of the reference slab was subjected to the blast effects of a 8 kg charge at 3 m of distance, corresponding to experimental Test No. 4. This analysis resulted in the relative displacement-time curve, represented in Figure 4.34, which resulted from the subtraction of the average displacements obtained at the end of the measuring rule to the mid-span displacement.

Since this calibration comprises the appraisal of the relative displacement obtained in the numerical model in comparison to the residual displacement obtained through the monitoring system of the experimental tests, the experimental residual displacement, δ_{res}, is also represented in Figure 4.34.

Analysing this figure, it is possible to observe that these two results are still far
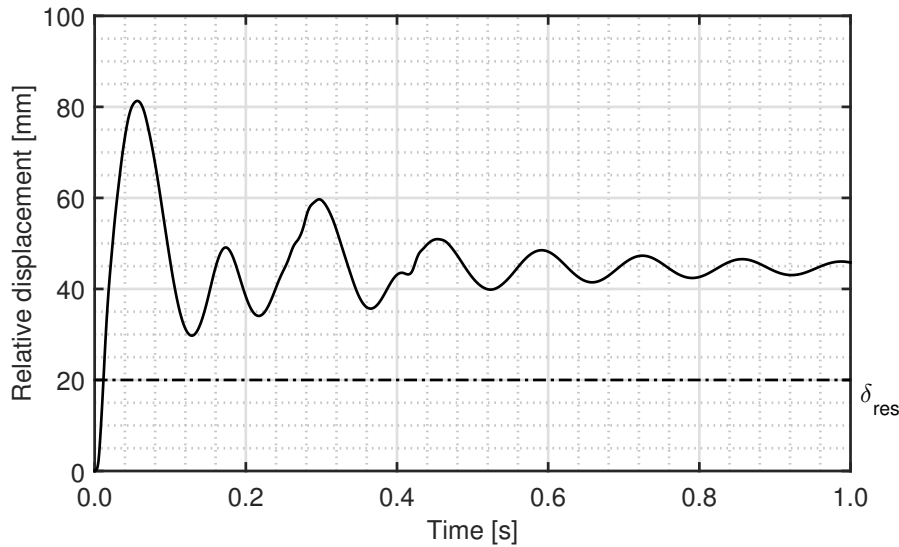
Figure 4.34: Initial relative displacement-time curve

apart from each other and that the numerical model must be calibrated in order to correctly simulate the behaviour of the experimental model. This calibration will be performed in the following sections.

Soil influence

As stated above, the material considered for the supports was the High Strength Concrete defined in the commercial software ELS. Additionally, it was considered that the base of the supports was fixed, which corresponds to a soil with infinite stiffness. However, through the observation of Figure 4.34, one can verify that the numerical test led to a greater residual displacement. Therefore, in order to dissipate some of the blast energy transmitted to the slab, the soil influence must be taken into account.

Due to the increased computational effort and time of analysis required to implement the soil explicitly in the ELS model, its influence will be incorporated in the supports.

Through the observation of Figure 4.35, one can consider that the soil present in the test site was a deposit of predominantly soft-to-firm cohesive soil, which is defined as a ground type D in the Eurocode 8 [14], and assume an $N_{SPT} = 15$. Using the expression defined by Stroud [44], one can estimate the Young's Modulus of the soil as a function of the N_{SPT}:

$$E \text{ [MPa]} = N_{SPT} \left(0.84 + 0.036 N_{SPT}\right) \tag{4.10}$$

resulting in $E = 20.7$ MPa.

Additionally, considering the soil as an elastic material with a Poisson's ratio of 0.2, it is possible to implement the soil's behaviour in the commercial software ELS with

Figure 4.35: Soil beneath the supports

the properties presented in Table 4.16.

Table 4.16: Soil properties implemented in the ELS

Units	E	G
I.S. [MPa]	20.70	8.63
ELS [tonf/m^2]	2326.77	969.49

Afterwards, in order to determine the behaviour of the soil and the support in series, an analysis was performed using the numerical model, illustrated in Figure 4.36. To ensure a correct simulation, the soil beneath the support should be large enough not to influence the model's stiffness. Therefore, assuming the soil's model as a cubic prism with 6.17x4.15x4.34 m created with 8 node elements, one can simulate the behaviour of the soil and the support in series.

In order to understand how the soil's mesh influenced the results, a mesh sensitivity analysis was carried out through the static application of a 1414.89 kN (120 tonf) distributed force to the support. Through the application of this force to each mesh, and ensuring that the model's behaviour is in the elastic phase, one can obtain the displacement which corresponds to the applied force and compare the results from different meshes. By analysing Table 4.17 and Figure 4.37, one can conclude that mesh No. 3 conducts to accurate results in a reasonable time of analysis. Hence, mesh No. 3 will be used to determine the behaviour of the soil and the support in series.

However, one must verify the soil's model dimensions to ensure a correct simulation. In Figure 4.38, the soil's total displacement plot is represented. Through its analysis, it is possible to conclude that the soil's model is large enough not to influence the model's stiffness, which was calculated through the static application of a distributed force to the support, resulting in the curve represented Figure 4.39.
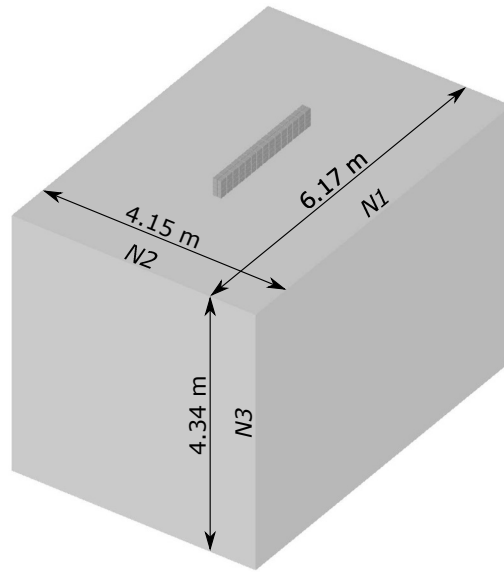
Figure 4.36: ELS numerical model of the support and the soil

Table 4.17: Soil mesh sensitivity analysis

Mesh No.	N1	N2	N3	No. of elements	Displacement [m]
1	12	10	9	1080	0.018
2	24	20	18	8640	0.029
3	50	40	35	70000	0.047
4	50	40	55	110000	0.045
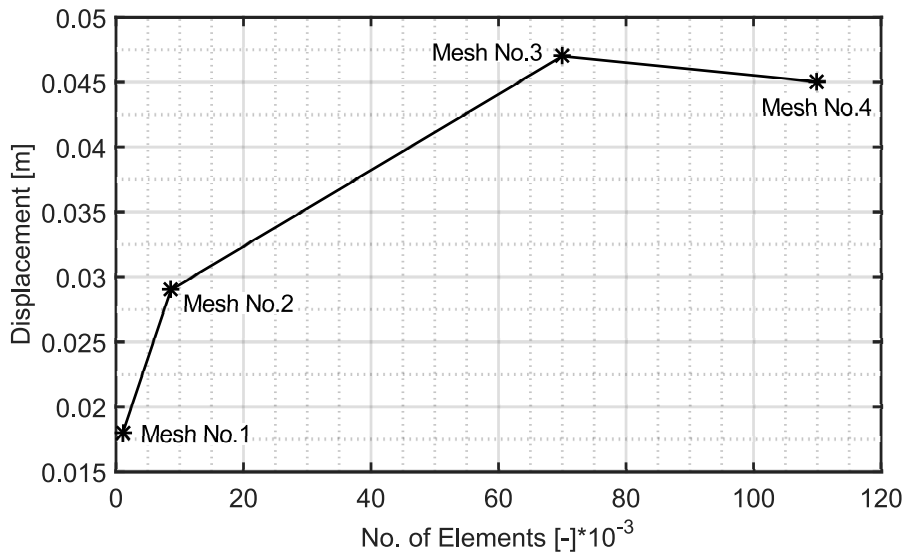
Figure 4.37: Soil mesh sensitivity analysis

With the determination of the stiffness of the soil and the support in series and the
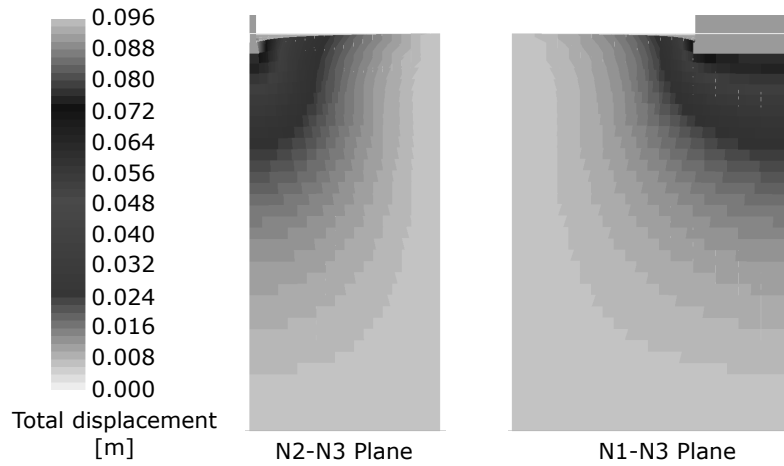
Figure 4.38: Soil's model dimensions verification
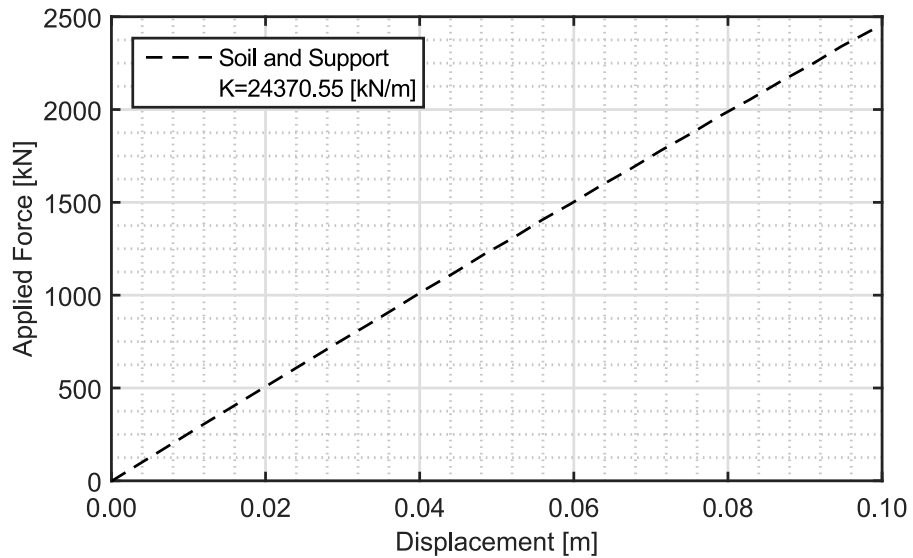
Figure 4.39: Soil and support force-displacement curve

definition of the support's geometry, the equivalent Young's and Shear modulus may be determined as follows:

$$K = 24370.55 \Leftrightarrow \frac{E_{eq}A}{L} = 24370.55 \Leftrightarrow \begin{cases} E_{eq} = 8984.53 \text{ kPa} \\ G_{eq} = 3743.56 \text{ kPa} \end{cases} \quad (4.11)$$

where $A = 0.3255$ m^2 and $L = 0.125$ m.

Considering the support's model presented in Section 4.3.2 with the material properties determined in equation (4.11), one obtains the force-displacement curves represented in Figure 4.40. Through the analysis of the referred figure, one can conclude that the final support correctly simulates the behaviour of the soil and support in series.
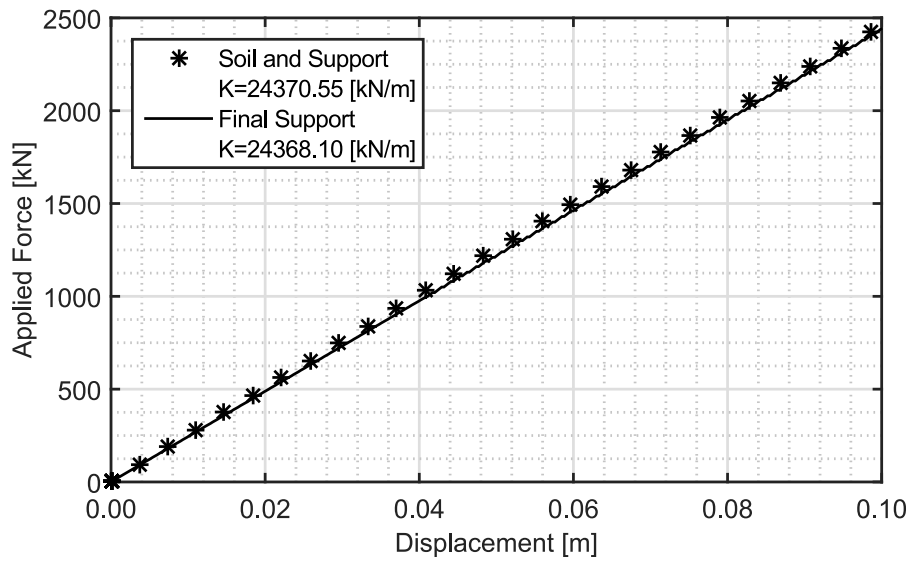
Figure 4.40: Final support force-displacement curve

However, due to the use of the Elastic Model implemented in the commercial software ELS, the final support's damping will be null.

As reviewed in Section 3.2.3, in order to obtain the damping ratio, r, implemented in ELS, one must determine the natural frequency of the structure. Hence, a modal analysis was performed to determine the first axial vibration mode of the final support, which is illustrated in Figure 4.41.
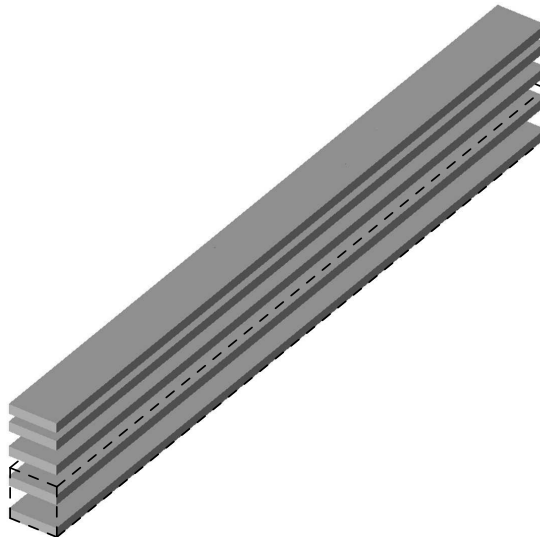
Figure 4.41: First axial vibration mode ($f = 721.83$ Hz)

If one considers a critical damping ratio $\xi = 1$ and the first axial natural frequency of the support $f = 721.83$ Hz, one obtains the critical damping ratio to be implemented

in the commercial software ELS r as:

$$r = 2\,\xi\,\omega_1 = 2 \times 1 \times 4535.36 = 9070.72 \text{ [s}^{-1}] \tag{4.12}$$

In order to verify the calculated result for the critical damping ratio $r = 9070.72$ s^{-1}, this same value was implemented in the model as a property of the final support's material. Afterwards, a constant force was dynamically applied to the support. In Figure 4.42, one can observe that a critically damped response of the final support was obtained for the implemented value of r, which verifies this value as the critical damping ratio. Additionally, in Figure 4.42, a displacement-time curve correspondent to $r = 0$ s^{-1} (undamped response), is also illustrated for comparison purposes.
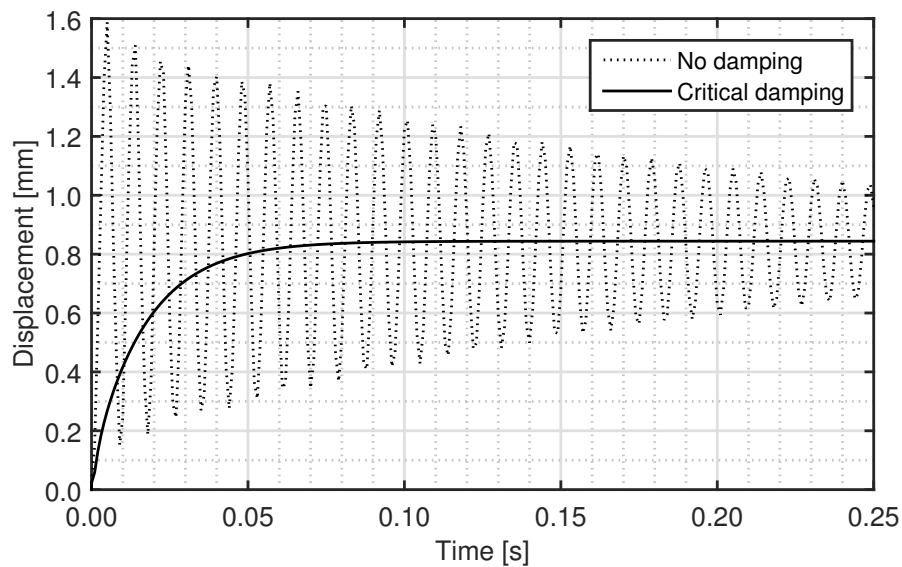
Figure 4.42: Final support's (undamped and critically damped) responses

As previously stated, the experimental models subjected to blast loads were simply supported slabs. Hence, in order to ensure correct boundary conditions in the numerical model, created with the commercial software ELS, a material with poor mechanical properties was assumed for the interface springs present between the slab and de supports. Thus, due to this assumption, the interface springs immediately fail after the contact of the shock wave with the slab, leading to the generation of contact springs, illustrated as circles in Figures 4.43 and 4.44.

Normal contact stiffness factor

As reviewed in Section 3.5, the commercial software ELS considers by default a normal contact stiffness factor N_F with a value of 0.01. However, this consideration led to inaccurate results due to the failure of the contact springs, as observed in Figure 4.44. Through the experimental field tests, it was possible to observe a total transfer of energy between the slab and the supports, without significant energy dissipation or loss of contact area during the loading phase due to failure,
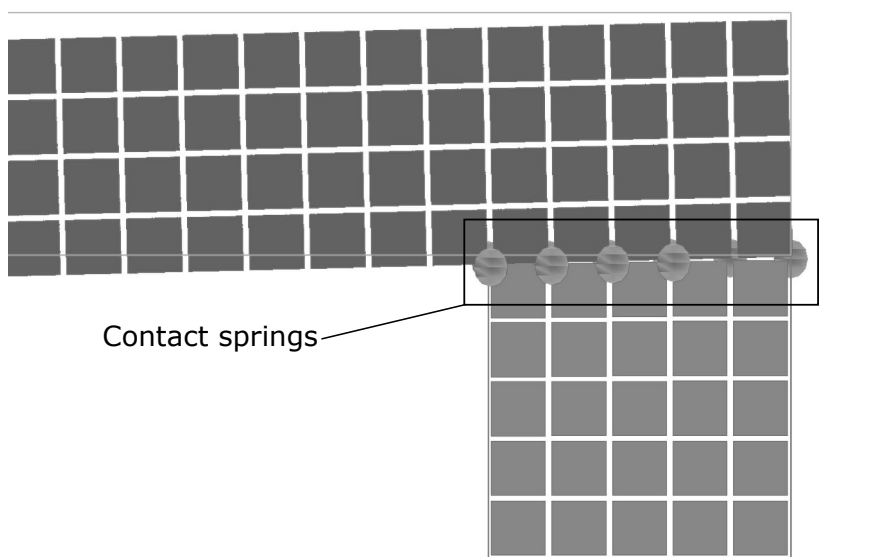
Figure 4.43: Contact springs created between the slab and the supports

cracking or stress concentrations, which is not compatible with an N_F value of 0.01. Therefore, a normal contact stiffness factor $N_F = 1$ is considered more appropriate than the default value assumed by the commercial software ELS.
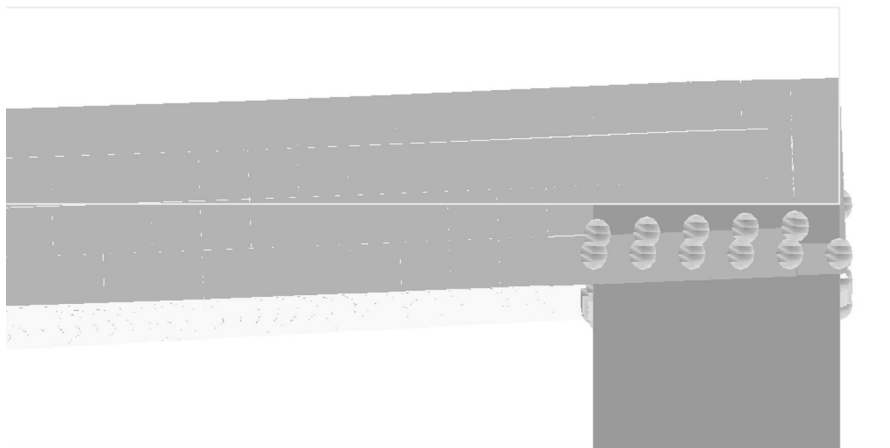
Figure 4.44: Failure of the supports' contact springs

Figure 4.45 represents both the initial result and the result obtained through the consideration of the soil's behaviour accounted for in the supports' behaviour and a normal contact stiffness factor $N_F = 1$ in order to obtain a comparison between them. Through this comparison, one can conclude that both considerations improve the obtained result.
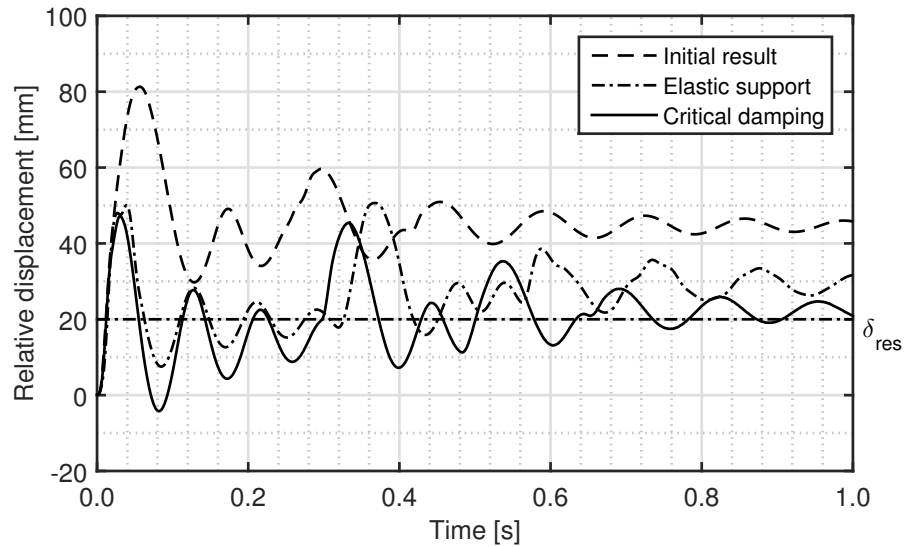
Figure 4.45: Soil and N_F's influence in the relative displacement-time curve

Contact spring unloading stiffness factor

Referring to Section 3.5, it is possible to verify that the ELS resorts to a ratio between the loading and unloading stiffness, defined as n, to consider energy dissipation during collisions. Thus, it is possible to conclude that this factor controls the amount of energy dissipated during contacts. Additionally, referring to [2], one can verify that the ELS considers that $n = 10$ as a reasonable value if the user does not have an estimation of a more accurate value. Considering the previous value for n means to consider that 90 % of the element's energy is dissipated during contact and only 10 % is recovered.

In Figure 4.46 one can observe the previous model's mid-span and supports displacements and verify the 60 mm lift of the slab from the supports, which might not correspond to the experimental model's results. Consequently, one can conclude that the considered energy dissipation during the unloading phase, defined by $n = 10$, was lower than required, and assume that a lower value for n is more appropriate.

Alternatively, values of 5 and 2.5 were tested for n, which resulted in the mid-span's displacement-time curves and the relative displacement-time curves illustrated in Figures 4.47 and 4.48. Through the observation of these figures, one can verify that the assumed values for n led to results that are very close to the results obtain with $n = 10$. In fact, considering $n = 2.5$ slightly increased the slab's lift from the supports and led to a larger residual displacement. Hence, the default value for n implemented in the commercial software ELS is considered to be accurate and will be maintained in the following analysis.
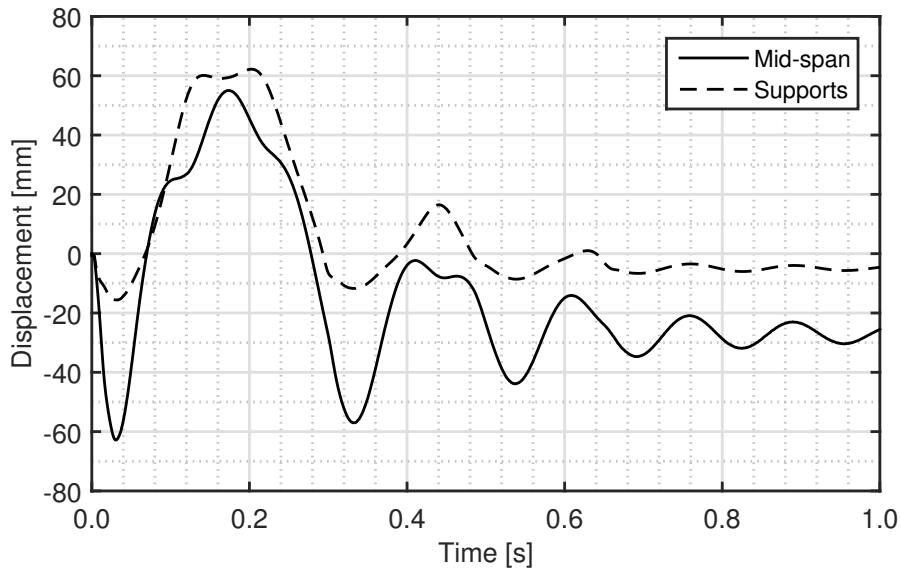
Figure 4.46: Displacement-time curves obtained with $N_F = 1$
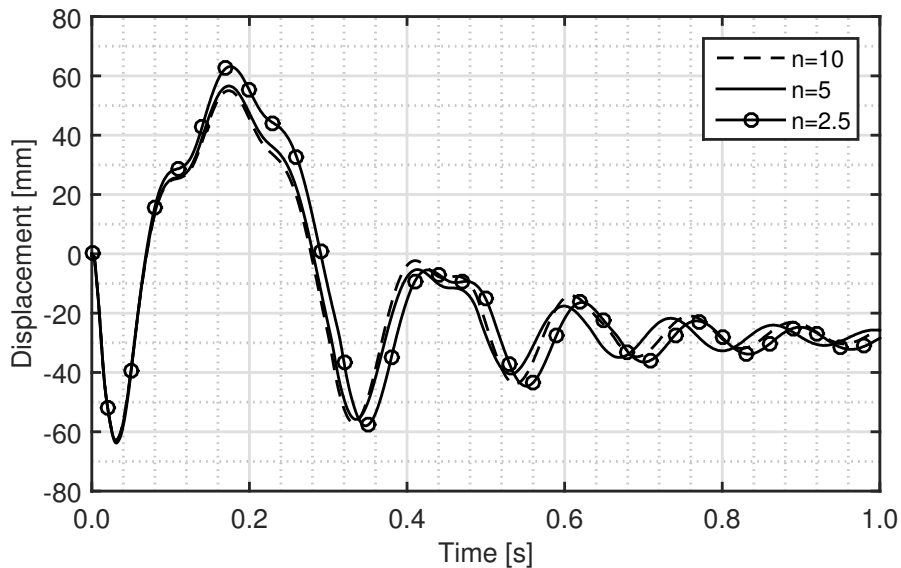
Figure 4.47: n's influence in the mid-span displacement-time curve

Dynamic Increase Factor

Assuming that the calibration of the numerical model is complete, i.e. that the material-independent numerical parameters are correct, one can consider the previously obtained results as the preliminary analysis for the implementation of the strain rate effects. First, one must determine the strain rates for the concrete and steel, which were computed from the deformations present in the springs represented in Figure 4.49. Due to the slab's cylindrical bending, only one set of springs for each material was required, which were the set of springs subjected to larger compression and tension stresses for the concrete and steel, respectively.
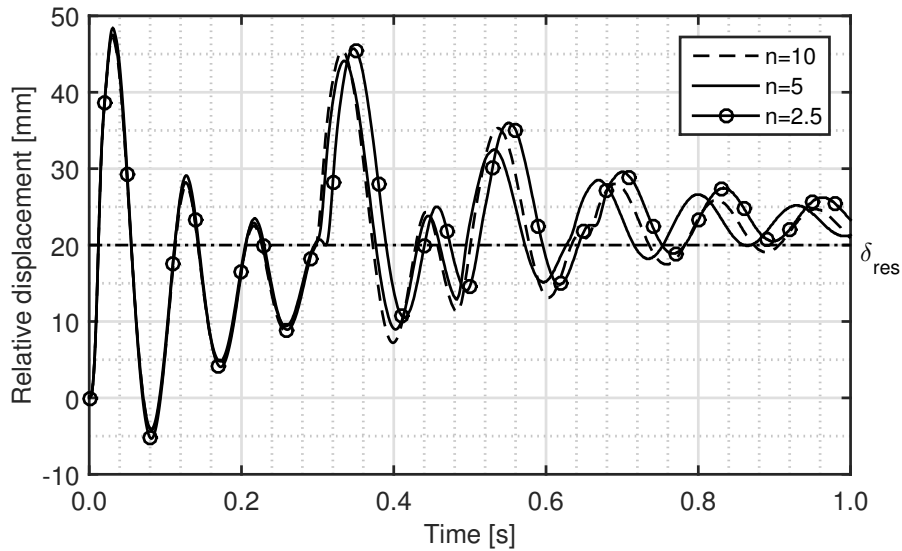
Figure 4.48: n's influence in the relative displacement-time curve

Furthermore, the same strain rate is assumed for the concrete's compression and tension strain rate effects.
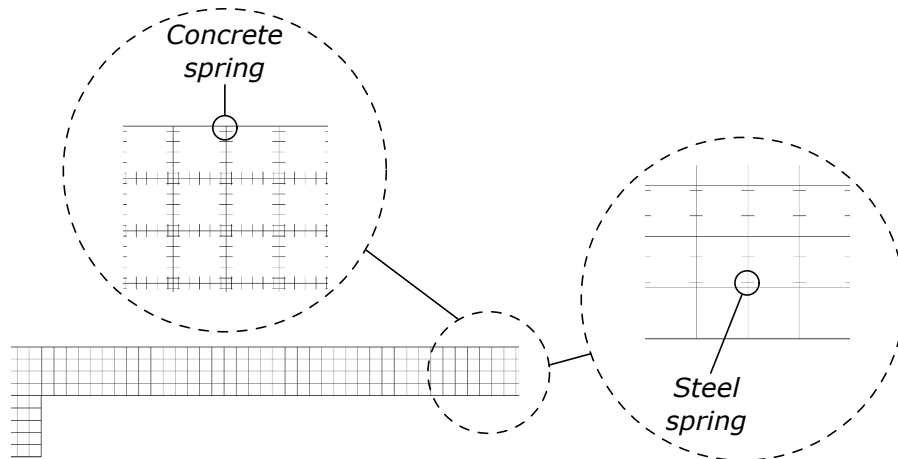
Figure 4.49: Concrete and steel springs used to measure the deformation

Figures 4.50(a) and 4.50(b) illustrate the strains obtained in the previously referred springs, while the strain rates of the concrete and steel, depicted in Figures 4.50(c) and 4.50(d), where obtained through the derivation of the strain curves represented in the former figures. Additionally, Table 4.18 presents the maximum strain rates for each material, which will be considered for the calculation of the DIFs.

Using the procedure reviewed in Section 2.5.1, one can compute the DIFs represented in Tables 4.19 and 4.20 for concrete and steel, respectively.

Through the multiplication of the concrete and steel properties presented in Tables 4.9 and 4.10, respectively, by the previously computed DIFs, one obtains the

(a) Concrete's strains

(b) Steel's strains

(c) Concrete's strain rates

(d) Steel's strain rates
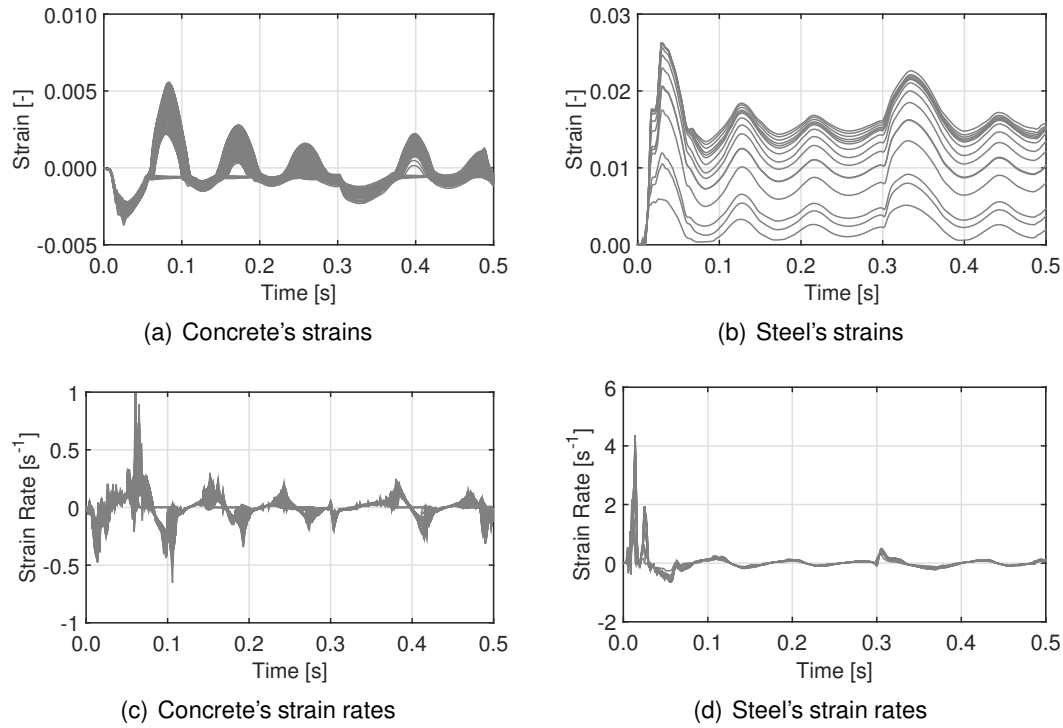
Figure 4.50: Strain rates obtained with DIF=1

Table 4.18: Strain rates obtained with DIF=1

Material	Max. strain rate
	[s^{-1}]
Concrete	0.9915
Steel	4.3730

Table 4.19: Concrete's DIFs

	Property	DIF
	f_{cm}	1.40
	f_{ctm}	1.59
E_{cm}	Compression	1.31
	Tension	1.39
	Average	1.35

Table 4.20: Steel's DIFs

Property	DIF
f_y	1.32
f_u	1.09

material mechanical characteristics represented in Tables 4.21 and 4.22. Note that

only the parameters which were altered are presented in these tables. Additionally, due to a greater f_y than f_u after the consideration of the strain rate effects, the f_y will be calculated as $0.9f_u$. Also, 0.01 is assumed as the value of the steel's post yield stiffness ratio.

Table 4.21: Concrete properties considering strain rate effects

Units	E_{cm}	f_{cm}	f_{ctm}
S.I. [MPa]	44586.87	64.71	4.60
ELS [tonf/m²]	5.01176x10⁶	7274.01	516.85

Table 4.22: Steel properties considering strain rate effects

Units	f_u	f_u/f_y	f_y	E_1/E
I.S. [MPa]	778.55	1.1 [-]	707.78	0.01 [-]
ELS [tonf/m²]	87512.91		79557.19	

Afterwards, by subjecting the updated numerical model to the blast effects, one obtains the strain rates for the concrete and steel depicted in Figure 4.51.

(a) Concrete's strains

(b) Steel's strains

(c) Concrete's strain rates

(d) Steel's strain rates
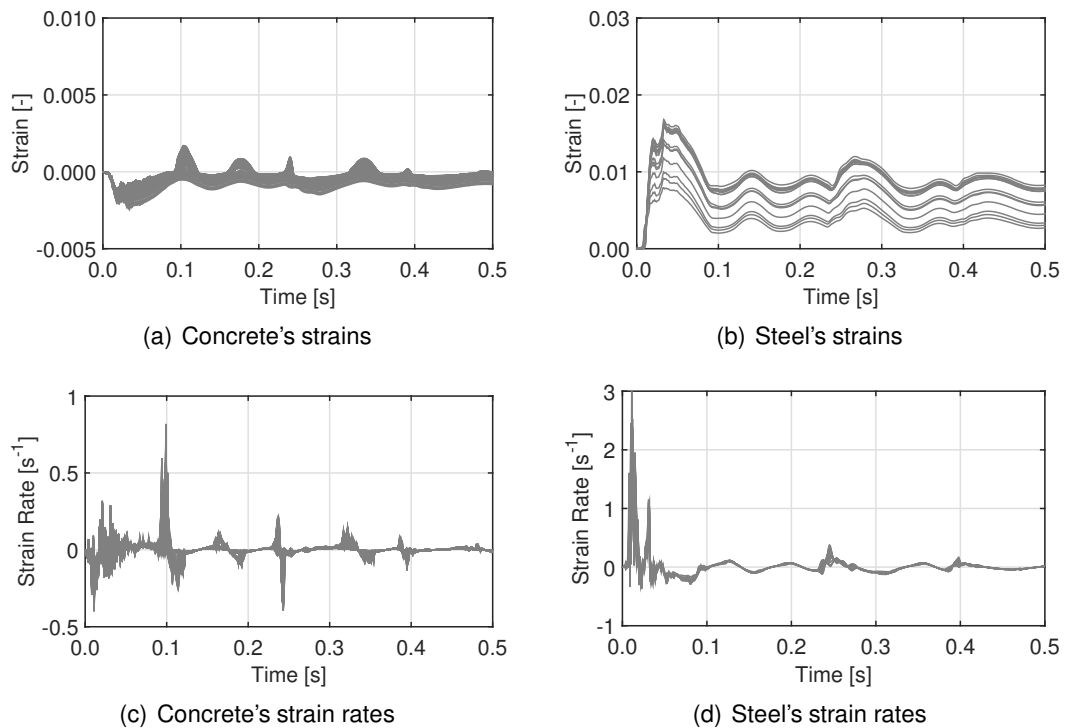
Figure 4.51: Updated numerical model strain rates

Additionally, in Table 4.23, one can observe the maximum strain rates obtained from the updated numerical model's results, and compute the DIFs presented in Tables 4.24 and 4.25.

Table 4.23: Updated numerical model strain rates

Material	Max. strain rate
	[s^{-1}]
Concrete	0.8191
Steel	2.9995

Table 4.24: Comparison of the concrete's DIFs

Property	Previous model	Updated model	Difference [%]
f_{cm}	1.40	1.39	0.61
f_{ctm}	1.59	1.57	0.69
E_{cm} (Average)	1.35	1.34	0.50

Table 4.25: Comparison of the steel's DIFs

Property	Previous model	Updated model	Difference [%]
f_y	1.32	1.30	0.96
f_u	1.09	1.09	0.30

Through the analysis of Tables 4.24 and 4.25, one can conclude that both DIFs are close to each other and that the end of the iterative procedure to determine the DIFs was reached. Hence, the convergence and sensitivity analysis is complete and the obtained results and parameters will be used to simulate the remaining experimental tests.

4.4   Numerical results and comparison

In the previous section, a convergence and sensitivity analysis was performed. Henceforth, numerically obtained results will be presented and compared to the experimental field test results.

4.4.1   Reference model

Figure 4.52 illustrates the displacement-time curves obtained when the reference numerical model was subjected to the blast effects of a 8 kg charge at a distance of 3.0 m, which corresponds to the configuration of experimental Test No. 4. In this figure, one can compare the experimental values of the residual and maximum displacement at mid-span with the corresponding numerical estimates.

Additionally, through the observation of this figure and Table 4.26, one can conclude that the calibrated model's results are similar to the results obtained in the experimental test. One can also observe a 26 and 55 % reduction in the difference between the numerical and experimental test results for the maximum and residual displacement, respectively, leading to the conclusion that the calibration for the reference model was successfully performed.
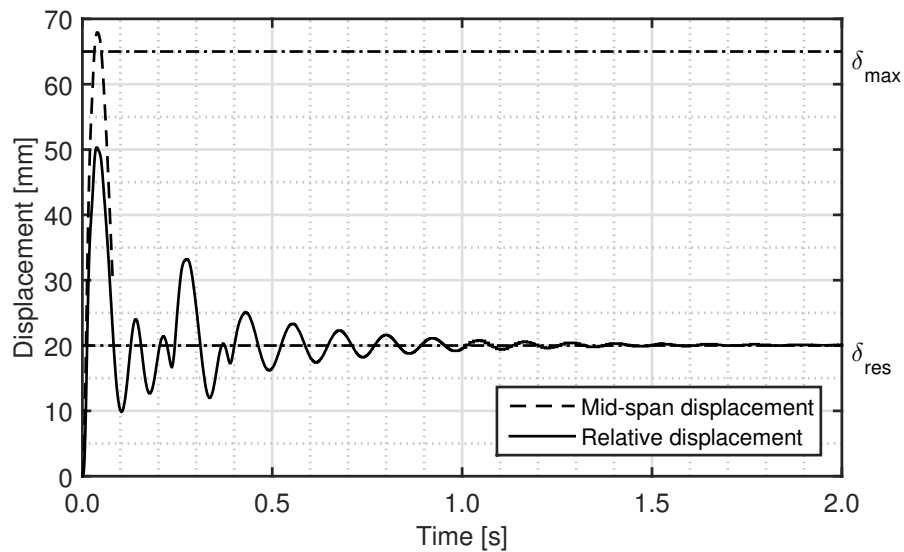
Figure 4.52: Reference model numerical results

Table 4.26: Differences between experimental and numerical model results

Displacement [mm]	Maximum	Residual
Experimental model	65	20
Initial numerical model	104	45
Difference [%]	30	55
Calibrated numerical model	68	20
Difference [%]	4	0

The cracking pattern of the bottom surface of the numerical model is presented in Figure 4.53 for the final step of analysis. The numerical model underestimates the cracking present in the bottom surface of the model, with the greatest crack width measuring 0.9 mm, while on the experimental model the measured crack widths varied between 2 to 3 mm. The difference between the widths of the cracks might be due to their greater distribution of cracking in the numerical model, when compared with the experimental model, whose cracking was characterized by a single main crack at mid-span, as observed in Figure 4.15(b). Note that the single main crack at mid-span present in the experimental model might result from the presence of the false joint, which probably led to a stress concentration at mid-span. However, in order to correctly model the false joint, the use of elements of a very small dimension becomes necessary, which would result in a high number of elements, resulting in an impracticably high time of analysis.

4.4.2 Experimental model B

With the calibration concluded and verified, and considering the parameters used for the reference model, a numerical model of the experimental model B was created. The initial DIFs considered in the reference numerical model will be used for all the materials present in numerical model B, i.e. the concrete's DIFs will
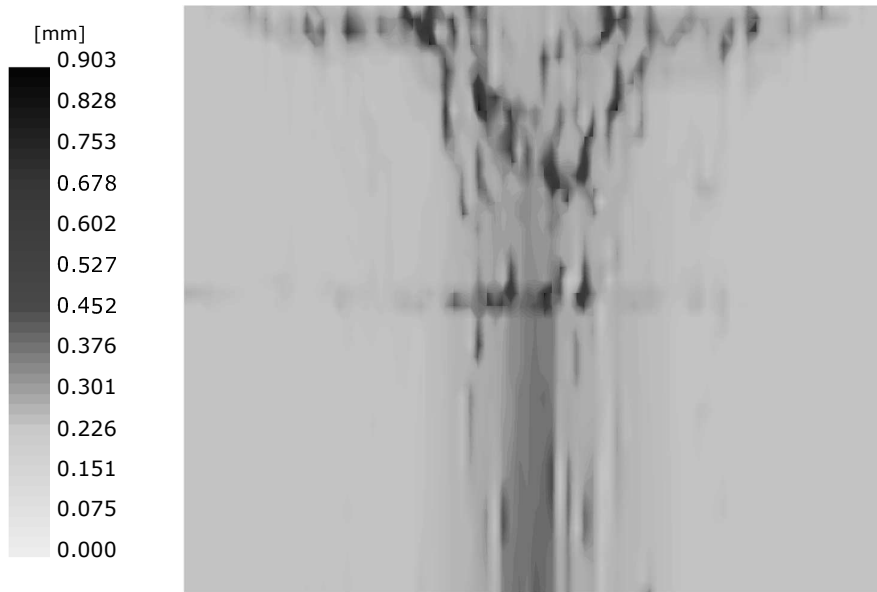
Figure 4.53: Cracking on the bottom surface of the reference numerical model

be considered for model B's concrete and grout, while the steel's DIFs will be considered for model B's steel reinforcement bars and fibres. By subjecting the numerical model B to the blast effects of the configuration used in Test No. 3, one obtains the displacement-time curves represented in Figure 4.54.
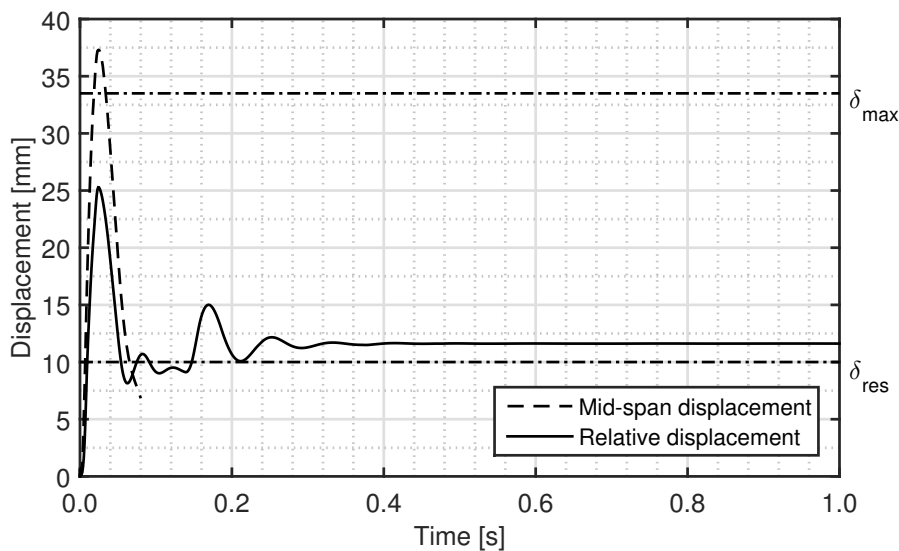
Figure 4.54: Experimental model B numerical results

Nonetheless, it is necessary to check the accuracy of the considered DIFs. To this end, Figure 4.55 is represented and analysed in order to obtain the maximum strain rates presented in Table 4.55, which lead to the DIFs illustrated in Tables 4.28 and 4.29. Through the comparison of these updated DIFs to the initially considered

DIFs, one could conclude that the initial DIFs considered for the steel are accurate. However, the initial DIFs considered for the concrete and the grout do not possess a reasonable accuracy. Therefore, it becomes necessary to update the numerical model in order to account for these differences.

(a) Concrete's strains

(b) Steel's strains

(c) Concrete's strain rates

(d) Steel's strain rates
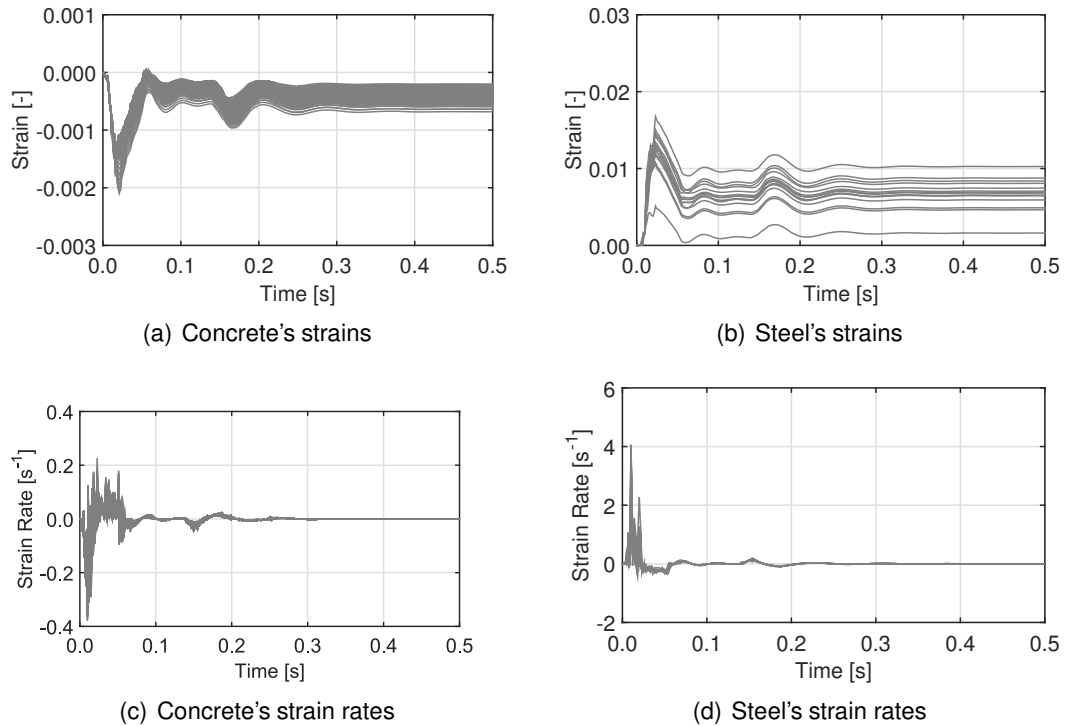
Figure 4.55: Numerical model B strain rates

Table 4.27: Strain rates with the initial DIFs

Material	Max. strain rate
	[s^{-1}]
Concrete and grout	0.3787
Steel and steel fibres	4.0617

Table 4.28: Comparison of the numerical model B concrete and grout's DIFs

Property	Reference model	Model B	Difference [%]
f_{cm}	1.40	1.35	3.04
f_{ctm}	1.59	1.53	3.43
E_{cm} (Average)	1.35	1.32	2.47

By subjecting the numerical model B with updated material parameters to the blast effects of Test No. 3, one obtains the strain-time and strain rate-time curves illustrated in Figure 4.56 and the maximum strain rates presented in Table 4.30,

Table 4.29: Comparison of the numerical model B steel and steel fibres' DIFs

Property	Reference model	Model B	Difference [%]
f_y	1.32	1.31	0.19
f_u	1.09	1.09	0.06

which can be analysed in order to obtain the DIFs depicted in Tables 4.31 and 4.32.

(a) Concrete's strains

(b) Steel's strains

(c) Concrete's strain rates

(d) Steel's strain rates
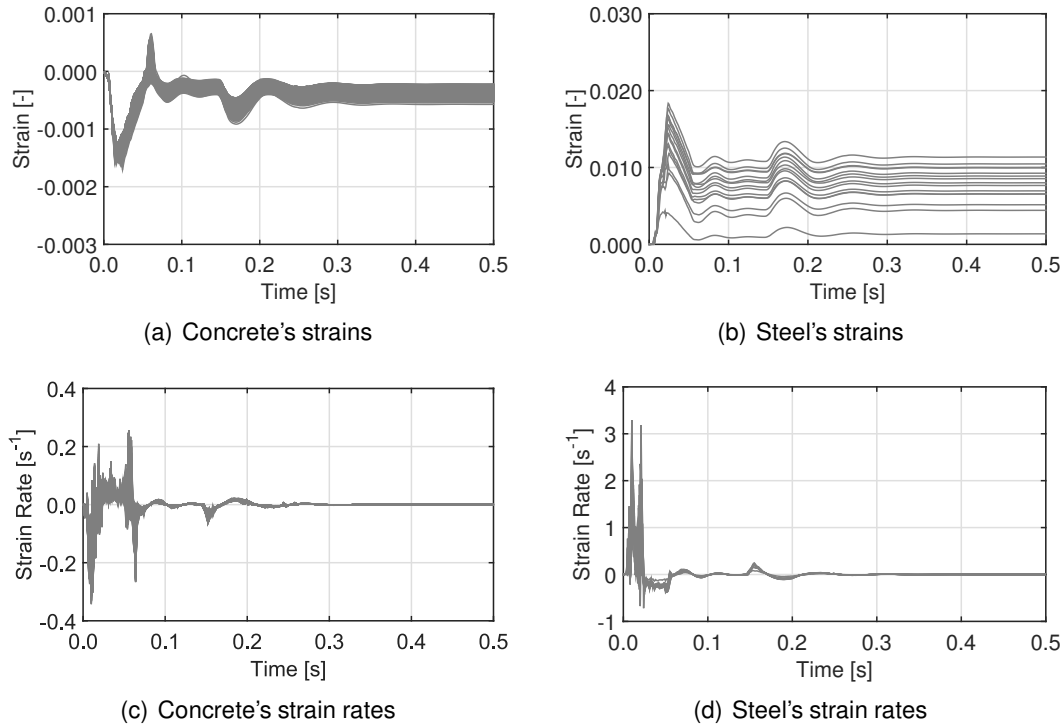
Figure 4.56: Strain rates of the updated numerical model B

Table 4.30: Strain rates with the updated DIFs

Material	Max. strain rate [s^{-1}]
Concrete and grout	0.3430
Steel and steel fibres	3.2908

Afterwards, through the comparison of the DIFs presented in Tables 4.31 and 4.32, one can conclude that the obtained DIFs are close to the DIFs resultant from the updated model and that the end of the iterative procedure to determine the DIFs was reached. Hence, it is possible to conclude that the obtained results correctly account for the strain rate effects.

Lastly, one must compare the numerically obtained results with the results obtained in the experimental Test No. 3 in order to verify the prediction capabilities of

Table 4.31: Comparison of the updated numerical model B concrete and grout's DIFs

Property	Previous model	Updated model	Difference [%]
f_{cm}	1.35	1.35	0.32
f_{ctm}	1.53	1.53	0.36
E_{cm} (Average)	1.32	1.31	0.26

Table 4.32: Updated numerical model B steel and steel fibres' DIFs

Property	Previous model	Updated model	Difference [%]
f_y	1.31	1.31	0.54
f_u	1.09	1.09	0.17

the commercial software ELS. Such comparison is presented in Figure 4.57 and Table 4.33, from which one can infer an acceptable difference between the experimental and numerical results, of 4 and 10 % for the residual and maximum displacement, respectively.
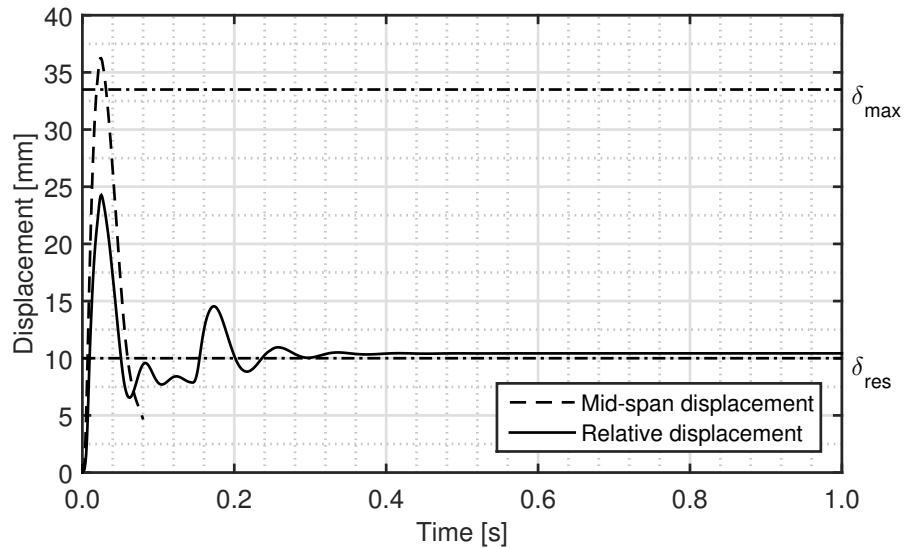
Figure 4.57: Updated numerical results of experimental model B

Table 4.33: Differences between experimental and numerical model B results

Displacement [mm]	Maximum	Residual
Experimental model	33.5	10.0
Numerical model	37.3	10.4
Difference [%]	10	4

Despite the calibration process, it is possible to observe larger difference between the numerical and experimental results for model B, which might result from differences in the applied blast effects, which were considered to be equal for

both models and greatly depend on the environmental factors. Additionally, the blast tests might have changed the soil properties, which might led to differences of the soil properties in the successive tests, hindering the generic application of the calibrated soil properties. Lastly, the fibremat's behaviour was calibrated from the experimental tests performed to the steel wires, from which the fibremat was produced, and modelled as a set of reinforcement bars, which might not be accurate since the mechanical properties of the steel wires change in the lamination process. Furthermore, the steel fibres are not straight and regular, which results in a very complex behaviour of the fibremat inside the grout, which leads to a limitation in the simulation of the fibre grout's behaviour, as set of 8 node elements and reinforcement bars.

Also, as performed for the reference model, the cracking present on the bottom surface of the slab in the numerical and experimental models was also compared. This comparison can be achieved through the observation of Figure 4.58, from which one can conclude that the cracking present on the bottom surface is similar to the obtained in the experimental model, which was characterized by a main crack at mid-span with a width of 1.3 to 2.5 mm along its length.

Figure 4.58: Cracking on the bottom surface of the numerical model B

Comparing Figures 4.53 and 4.58, it is possible to observe that the obtained cracking patterns are different. In order to understand why a cracking concentration occurs in model B's results and not in the results of the reference model, a time-history analysis of the model was performed. From this analysis a separation of elements in the model's height, as represented in Figure 4.59, was possible to observe. This separation led to a concentration of stresses at mid-span and resultant concentrated cracking. However, additional studies are required in order to understand the reason why this slit occurred.

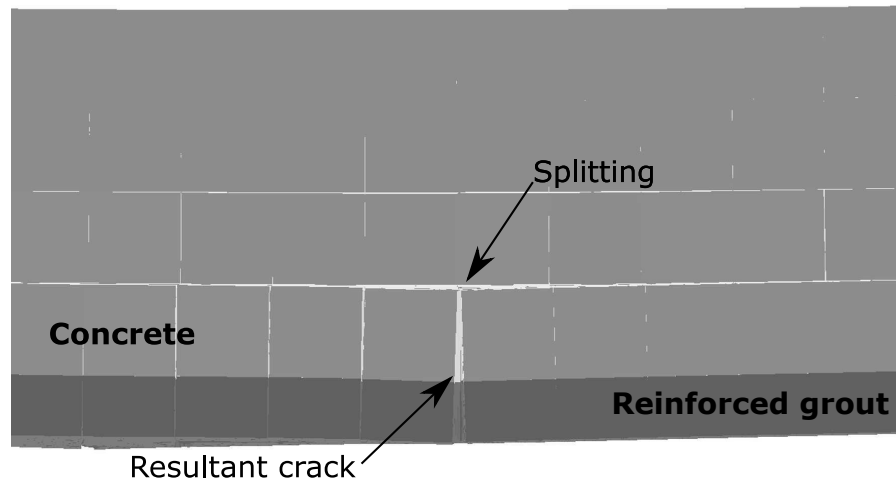Through the comparison of the numerical and experimental results, it is possible

Figure 4.59: Splitting of elements at mid-span

to conclude that the Applied Element Method can accurately predict and simulate the response of fibre grout RC panels when subjected to blast effects.

Chapter 5

Conclusions and Future Work

This chapter presents the conclusions of the performed study and some future work of interest to the field of study.

5.1 Conclusions

Currently, the crescent risk of explosions caused by accidents or terrorist attacks, which cause thousands of fatalities annually, calls for the need to design structures that are able to withstand the dynamic effects caused by an explosion or investigate reinforcement methods that can strengthen the existing structures in order for these to do so as well. However, most of the research in this field was performed by the armed forces, government research facilities or by large industrial explosive manufacturers, and thus, designers do not have access to the results obtained.

On the other hand, the physics of the detonation process, from initiation to the formation of the shock front and blast wave, has been well documented by Kinney and Graham [23], Baker [5], Henrych [19] and in the UFC [13]. Hence, a review and comparison of the main effects of an explosion, namely, its blast overpressures and the shock loads produced by the blast wave, defined by the different formulations, was performed in order to achieve a better understanding of the topic.

Through the analysis of the performed review and application to the case study, it was possible to conclude that, depending on the considered formulation, one obtains different values for the main effects of an explosion. These differences reached approximately 60 % for the determined free-air burst parameters and 59 % for the maximum displacement estimates of the case study.

As a result of the highly dynamic loading conditions that outcome from the blast scenarios, complex methods must be used in the numerical analysis of this scenarios. Due to the limitations of the Finite Element Method, specifically in the simulation of large deformations and cracking of reinforced concrete structures, this method is inappropriate to simulate the behaviour of structures when they are severally loaded and close to the collapse.

Therefore, the Applied Element Method was used as an alternative to simulate the

response of fibre grout strengthened RC panels when subjected to blast effects, as a part of the *Segurança e Integridade Estrutural de Edifícios Estratégicos face a explosões acidentais ou provocadas - SI4E* project.

The Applied Element Method implementation on the commercial software *Extreme Loading for Structures* proved to be a reliable tool in the simulation of blast scenarios, due to its ability to simulate with reasonable accuracy the non-linear structural behaviour through the various loading phases. To ensure a correct pressure-time loading simulation, an analysis time step of 0.0001 s was used from the time of detonation until the overpressure on the exposed surface was null. After this phase, which is about 0.05 s, the analysis was performed for another 1.95 s, with a time step of 0.001 s. This led to approximately 8-10 hours of analysis time to calculate the 2450 time steps required. Therefore, every effort in order to minimize the processing time should be applied, as long as reasonable accuracy is maintained.

Through the collaboration with the Portuguese Military Academy, it was possible to perform an experimental campaign in the military camp situated in *Santa Margarida*, Portugal. This experimental campaign allowed the definition of the blast effects on a RC panel (reference model) and a fibre grout strengthened RC panel (model B). However, the lack of definition of the boundary conditions, specifically the soil underneath the supports, and the lack of a pressure monitoring system led to difficulties in the calibration process of the numerical model created in the commercial software *Extreme Loading for Structures*.

Nevertheless, the calibration for the response of the reference model when subjected to the blast effects of the experimental set-up was successfully performed. Afterwards, the same numerical parameters were considered in the fibre grout RC panel simulation. Through the analysis of the numerical results and subsequent comparison with experimental results, it is possible to conclude the following:

- As expected, the calibrated model correctly simulates the response of the reference model, with a difference of 0 and 4 % for the residual and maximum displacements, respectively;

- Additionally, through the comparison of the cracking on the bottom surface of the reference model, one can conclude that the numerical model underestimates the cracking present in the bottom surface of the model, with the greatest crack width measuring 0.9 mm, while on the experimental model the measured crack widths varied between 2 to 3 mm. The difference between the widths of the cracks might be due to their greater distribution in the numerical model, when compared with the experimental model;

- On the other hand, the numerical model B simulates the response of the fibre grout strengthened RC panel with an acceptable difference between the experimental and numerical results, of 4 and 10 % for the residual and maximum displacements, respectively;

- However, the cracking present on the bottom surface of the numerical model was similar to the obtained in the experimental model, which was characterized by a main crack at mid-span with a width of 1.3 to 2.5 mm along its length.

The greater differences observed in the results of model B might be due to the following factors or limitations:

- The observed differenced may result from the lack of measurement of the applied pressures in the performed test. Taking into account that the applied pressure depends on several environmental factors it may have not be same in all tests;

- It is known that the results of dynamic analyses greatly depend on the boundary conditions. For the case study, uncertain properties have to be modelled for the boundary condition related to the soil structure interaction due to uncertainties in the soil properties, hindering the generic application of the calibrated parameters;

- The fibremat's behaviour was calibrated from the experimental tests performed to the steel wires from which the fibremat is produced and modelled as a set of reinforcement bars, which might not be accurate since the mechanical properties of the steel wires are changed in the lamination process;

- Furthermore, the surface area of the fibres is substantially larger than its section, resulting in a great adhesion between the fibre and the grout when compared to the adhesion of a reinforcement bar inside concrete;

- Lastly, the steel fibres are not straight and regular, which results in a very complex behaviour of the fibremat inside the grout, which leads to a limitation in the simulation of the fibre grout's behaviour.

Despite the previous limitations and errors, it is possible to conclude that the Applied Element Method can accurately predict and simulate the response of fibre grout RC panels when subjected to blast effects.

5.2 Future work

In the present dissertation, the proposed objectives were fulfilled. The suggestions for future research presented below are limited by the experience of the author.

- More experimental field tests with measurement of the applied pressure to several structural components;

- Better definition of the boundary conditions when performing experimental blast tests;

- Development, resorting to the Applied Element Method, of protection solutions for military and civil structures to withstand blast effects;

- Resort to a flexural test in order to correctly calibrate the behaviour of the fibre grout in the commercial software *Extreme Loading for Structures*;

- Disseminate the results to the scientific community.

References

[1] Applied Science International, Durham, NC: *Extreme Loading for Structures V3.1 - Modeling Manual*, April 2010.

[2] Applied Science International, Durham, NC: *Extreme Loading for Structures - Theoretical Manual*, 2013.

[3] Applied Science International, LLC: *Vulnerability assessment: Murrah federal building.* `http://www.appliedscienceint.com/case-studies/`, visited on 2015-08-18.

[4] Asprone, D., A. Nanni, H. Salem, and H. Tagel-Din: *Applied element method analysis of porous GFRP barrier subjected to blast.* Advances in Structural Engineering, 13(1):153–170, 2010.

[5] Baker, W.E., P.A. Cox, J.J. Kulesz, R.A. Strehlow, and P.S. Westine: *Explosion Hazards and Evaluation.* Number 5 in *Fundamental Studies in Engineering.* Elsevier Science, 1983.

[6] Bischoff, P.H. and S.H. Perry: *Compressive behaviour of concrete at high strain rates.* Materials and structures, 24(6):425–450, 1991.

[7] Bulson, P.S.: *Explosive Loading of Engineering Structures.* CRC Press, 1st edition, 1997.

[8] *China explosions: What we know about what happened in Tianjin*, August 2015. `http://www.bbc.com/news/world-asia-china-33844084`, visited on 2015-08-20.

[9] Codimetal Industries, S.A.: *Rede electrossoldada*, 2014. `http://www.codimetal.com/pt/produtos/rede-electrossoldada.html`, visited on 2015-06-04, (In Portuguese).

[10] Coffield, A. and H. Adeli: *An investigation of the effectiveness of the framing systems in steel structures subjected to blast loading.* Journal of Civil Engineering and Management, 20(6):767–777, 2014.

[11] Committee for the Prevention of Disasters Due to Dangerous Substances, The Hague, Netherlands: *Method for the determination of possible damage to people and objects resulting from releases of hazardous materials (CPR 16E) TNO Green Book*, 1992.

[12] Dept of Army: *US Army Fundamentals of Protective Design (Non-Nuclear)*, 1965. Technical Manual TM5-855-1.

[13] Dept of Defense: *"Unified Facilities Criteria: Structures to Resist the Effects of Accidental Explosions" UFC 3-340-02*, December 2008.

[14] European Committee for Standardization (CEN): *EN1998-1: Eurocode 8: Design of structures for earthquake resistance - Part 1: General rules, seismic actions and rules for buildings*, 2004.

[15] Extreme Loading for Structures: *version 3.1*. Applied Science International, Durham, NC, 2013.

[16] FAVIR: *Fábrica de plásticos, Lda*, 2015. `http://www.favir.pt/index.php`, visited on 2015-08-10, (In Portuguese).

[17] Gião, R., V. Lúcio, C. Chastre, and A. Brás: *UFRG-unidirectional fibre reinforced grout as strengthening material for reinforced concrete structures*. Lisboa: BEFIB2012, 2012.

[18] Gonçalves, M.: *Reforço de placas de betão armado com argamassas armadas para acções de explosão*. Master's thesis, Faculdade de Ciências e Tecnologia - UNL, March 2015. (In Portuguese).

[19] Henrych, J.: *The Dynamics of Explosion and Its Use*. Developments in Atmospheric Science. Elsevier Scientific Publishing Company, 1979.

[20] Instituto Português da Qualidade (IPQ): *Norma Portuguesa NP EN206-1: Betão, Parte I: Especificação, desempenho, produção e conformidade*, 2007. (In Portuguese).

[21] Instituto Português da Qualidade (IPQ): *Norma Portuguesa NP EN1992 1-1: Eurocódigo 2: Projecto de estruturas de betão, Parte 1-1: Regras gerais e regras para edifícios*, 2010. (In Portuguese).

[22] Kennedy, W.D.: *Effects of impact and explosion*. Summary technical report of division 2, NDRC, volume I AD 221 586, Office of Scientific Research and Development, Washington, D.C., 1946.

[23] Kinney, G.F. and K.J. Graham: *Explosive Shocks in Air*. Springer Berlin Heidelberg, 2nd edition, 1985.

[24] Krauthammer, T.: *Modern Protective Structures*. Civil and environmental engineering. CRC Press, 2008.

[25] Kupfer, H., H.K. Hilsdorf, and H. Rusch: *Behavior of concrete under biaxial stresses*. In *ACI Journal proceedings*, volume 66-8. ACI, 1969.

[26] Magnusson, J.: *Structural concrete elements subjected to air blast loading*. Licentiate thesis, KTH, May 2007.

[27] Malvar, L.J. and J.E. Crawford: *Dynamic increase factors for concrete*. Technical report, DTIC Document, 1998.

[28] Malvar, L.J. and J.E. Crawford: *Dynamic increase factors for steel reinforcing bars*. In *Proceedings of the Twenty-Eighth DoD Explosives Safety Seminar*, 1998.

[29] Mayorca, P. and K. Meguro: *Modeling masonry structures using the applied element method*. SEISAN KENKYU, 55(6):581–584, 2003.

[30] MC90, CEBFIP: *Design of concrete structures. CEB-FIP model code 1990*, 1993.

[31] Meguro, K. and H. Tagel-Din: *Applied element method for structural analysis: Theory and application for linear materials*. Structural Engineering Earthquake Engineering, 17(1):21s–35s, 2000.

[32] Meguro, K. and H. Tagel-Din: *Applied element simulation of RC structures under cyclic loading*. Journal of Structural Engineering, 127(11):1295–1305, 2001.

[33] Meguro, K. and H. Tagel-Din: *Applied element method used for large displacement structural analysis*. Journal of Natural Disaster Science, 24(1):25–34, 2002.

[34] Mlakar, P.F. and D. Barker: *Handbook for Blast Resistant Design of Buildings*, chapter Blast Phenomena. Wiley, 2010.

[35] Needham, C.E.: *Blast Waves*. Shock Wave and High Pressure Phenomena. Springer Berlin Heidelberg, 2010.

[36] Okamura, H. and K. Maekawa: *Nonlinear analysis and constitutive models of reinforced concrete*. Gihodo Co. Ltd., Tokyo, 1991.

[37] Press, W.H., S. A Teukolsky, W.T. Vetterling, and B.P. Flannery: *Numerical recipes in Fortran 77 and Fortran 90*. Cambridge University Press Cambridge, 1996.

[38] Ramancharla, P.K., H. Tagel-Din, and K. Meguro: *Dynamic modeling of dip-slip faults for studying ground surface deformation using applied element method*. 13th World Conference on Earthquake Engineering, 2004.

[39] Ramos, A.P. and V. Lúcio: *Sebenta de estruturas de betão armado I e II*. Faculdade de Ciências e Tecnologia da Universidade Nova de Lisboa, September 2009. (In Portuguese).

[40] Ristic, D., Y. Yamada, and H. Iemura: *Stress-strain based modeling of hysteretic structures under earthquake induced bending and varying axial loads*. Research Rep. No. 86-ST, 1, 1986.

[41] Sim, D.: *China explosions aftermath: Photos from inside the blast zone show the devastation in Tianjin*, August 2015.

[42] Smilowitz, R., C. Arnold, M. Ettouney, M. Hankewycz, W. Blewwet, M. Kaminskas, and E. Letvin: *Reference Manual to Mitigate Potential Terrorist Attacks Against Buildings, FEMA 426/BIPS 06*. Buildings and Infrastructure Protection Series. U.S. Dept. of Homeland Security, Washington, DC, 2nd edition, October 2011.

[43] Smith, P.D. and J.G. Hetherington: *Blast and ballistic loading of structures*. Digital Press, 1994.

[44] Stroud, M.A.: *The standard penetration test: its application and interpretation*. In *Proc. of the Conference on Penetration Testing in the UK, Birmingham. Thomas Telford, London*, 1989.

[45] Tabatabaei, Z.S., J.S. Volz, J. Baird, B.P. Gliha, and D.I. Keener: *Experimental and numerical analyses of long carbon fiber reinforced concrete panels exposed to blast loading*. International Journal of Impact Engineering, 57:70–80, 2013.

[46] Tagel-Din, H. and K. Meguro: *Applied element simulation for collapse analysis of structures*. Bull. of Earthquake Resistant Struct. Res. Ctr, pages 113–123, 1999.

[47] Tagel-Din, H. and K. Meguro: *Analysis of a small scale RC building subjected to shaking table tests using applied element method*. 12th World Conference on Earthquake Engineering. New Zealand:[sn], pages 1–8, 2000.

[48] Tagel-Din, H. and K. Meguro: *Applied element method for dynamic large deformation analysis of structures*. Structural Engineering Earthquake Engineering, 17(2):215s–224s, 2000.

[49] Tagel-Din, H. and K. Meguro: *Nonlinear simulation of RC structures using applied element method*. Structural Engineering Earthquake Engineering, 17(2):137s–147s, 2000.

[50] U.S. Army Corps of Engineers: *"Methodology Manual for the Single-Degree-of-Freedom Blast Effects Design Spreadsheets" PDC TR-06-01*, September 2008.

[51] Štoller, Major Eng. J. and Lieutenant Colonel E. Zezulová: *The field testing of high performance fiber reinforced concrete slabs under the tnt load explosion together with the analytical solution and the numerical modelling of those tests results*. In *Military Technologies (ICMT), 2015 International Conference on*, pages 1–8. IEEE, 2015.

[52] Wijesundara, L.M.G. and S.K. Clubley: *Numerical modelling of reinforced concrete columns subject to coupled uplift and shear forces induced by internal explosions*. Structure and Infrastructure Engineering, (ahead-of-print):1–17, 2015.

[53] Yandzio, E. and M. Gough: *Protection of buildings against explosions*. Steel Construction Institute UK, 1999.